The Dissertation Committee for Min-Soo Noh
Certifies that this is the approved version of the following dissertation:

Material Growth and Characterization of GaAsSb on GaAs Grown by MOCVD for Long Wavelength Laser Applications

Committee:

Russell D. Dupuis, Supervisor

Joe C. Campbell

Sanjay K. Banerjee

Leonard F. Register

Llewellyn K. Rabenberg

Material Growth and Characterization of GaAsSb on GaAs Grown by MOCVD for Long Wavelength Laser Applications

by

Min-Soo Noh, B.S., M.S.

Dissertation

Presented to the Faculty of the Graduate School of
The University of Texas at Austin
in Partial Fulfillment
of the Requirements
for the Degree of

Doctor of Philosophy

The University of Texas at Austin
December 2003

Dedication

Dedicated to my parents
and to my loving and supportive wife, Sora Jeong,
and to my three sweet sons, JeeWon, JeeHoo, and JeeHoon

Acknowledgements

I would like to express my sincere gratitude to all those who have helped make this work and dissertation possible. First, I would like to thank my advisor, Professor Russell D. Dupuis, for his guidance and for giving me the opportunity to participate in optoelectronics research that is very stimulating and challenging. His devotion for work and deep and wide knowledge of semiconductors inspired me very much. I am proud of being one of his students. Special thanks are also due to Dana Dupuis for her assistance with preparing this dissertation.

I would like to thank Professor Sanjay Banerjee, Joe Campbell, Llewellyn Rabenberg, and Professor Leonard Register for agreeing to serve on my dissertation committee. It is an honor to have such esteemed professors on my committee.

Also, I would like to thank Professor Choong Hyun Chung who encouraged me to pursue Ph.D. degree by telling me that I was not too old to study again.

I was lucky to have been a part of the MOCVD group and to work with some bright and intelligent friends and graduate students. I would like to thank all of my co-workers, past and present - Dr. Uttiya Chowdhury, Dr. Bryan Shelton, Dr. Mike Wong, Dr. Ting-Gang Zhu, Jin-Ho Choi, Jonathan Denyszyn, Richard Heller, Dr. Damien Lambert, Dr. Jae-Hyun Ryou, Yuichi Sasajima, Tomoyuki Takada, Dong-Won Yoo, and post-doctoral fellows Dr. Joongseo Park, Dr. Ho-Ki Kwon, Dr. Ki-Soo Kim, and Dr. Xuebing Zhang.

I also thank the staff at The University of Texas Microelectronics Research Center - William Fordyce, Brenda Francis, James Hitzfelder, Jesse James, Joyce Kokes, Terry Mattord, Steve Moore, Robert Stephens, and Jean Toll for their help.

Many collaborators have contributed to make this work possible. I acknowledge the very beneficial collaboration with Prof. Kuang-Chien Hsieh at the University of Illinois at Urbana-Champaign for the TEM work. In addition, I would particularly like to thank Justin Elkow, Dr. Gabriel Walter, and Professor Nick Holonyak, Jr. at the University of Illinois at Urbana-Champaign for their laser fabrication and characterization.

I must express my gratitude to industrial collaborators for their precious technical discussions, material characterization, and for the supply of materials. These include Drs. Ying-Lan Chang, Dave Bour, Joachim Kruger, and Robert Weissman at Agilent Technologies and Dr. Ravi Kanjolia and Barry Leese of Epichem.

I would like to thank some of the graduate students at the MRC including Chulchae Choi and ByungKi Woo for their invaluable discussions and friendship.

This research has been funded in part by the National Science Foundation (NSF), Agilent Technologies, DARPA, and Epichem. Many thanks are extended to these companies and agencies.

Finally, I would like to thank my parents and parents-in-law for their endless love and unconditional support. I must also mention my brother Min-Jung’s family for all their love. This accomplishment would not be possible without the patience and support of my loving wife, Sora Jeong, who has had real hard time to bring up our three sons, JeeWon, JeeHoo, and JeeHoon almost by herself.

Material Growth and Characterization of GaAsSb on GaAs Grown by MOCVD for Long Wavelength Laser Applications

Publication No._____________

Min-Soo Noh, Ph.D.
The University of Texas at Austin, 2003

Supervisor: Russell D. Dupuis

Due to the demand for faster and higher bit rate optical communication, long wavelength vertical cavity surface emitting laser (VCSEL) has been attracting great interests because of its ability of 2D array application. Although InGaAsP/InP edge emitting lasers (EEL) have been well developed and commercially available, the lack of high contrast distributed Bragg reflector (DBR) for the material system forced to find new active materials that can be grown on GaAs substrate to exploit AlGaAs/GaAs DBR pairs. For the purpose, GaAsSb has been studied as the active material. This dissertation describes and discusses the GaAsSb semiconductor material growth, the optimization of the growth conditions, and the characterization of the laser devices fabricated from GaAsSb QW structures. Based on the optimal growth conditions, EELs operating at room temperature in CW mode at the wavelength of 1.27 μm have been demonstrated from the GaAsSb QW structure with GaAsP barriers grown monolithically by MOCVD.

Table of Contents

List of Tables

List of Figures

Chapter 1: Introduction

This chapter discusses the basic background of the long wavelength light emitter application, the feasibility of novel GaAsSb material as an active region for a long wavelength laser diode operating at ~1.31 μm, the GaAsSb material properties, and recent research progress in GaAsSb. The technical motivation and challenges related to this study are also discussed.

1.1 APPLICATION OF LONG-WAVELENGTH INFRARED OPTOELECTRONICS

In the recent couple of decades, communication systems that are based on data transmission in the form of light beams have made rapid progress. This was possible mainly due to the development over the past 50 years of optical fibers, light emitting devices, and the other necessary optical components such as photodiodes, modulators, etc. However, continuously increasing demands for transmitting and receiving enormous amounts of data require new light emitting and detecting devices of higher speed and better quality. To meet these needs, much research has been performed to develop improved light emitting devices that are one of the key components in optical fiber communication systems.

Optoelectronic devices that generate long-wavelength infrared light in the wavelength range from 1.3 μm to 1.6 μm in vacuum are of great importance in optical communications since currently, the highest performance optical fibers have a relatively low loss in this wavelength range. Wavelengths that extend from 1.49 μm to 1.61 μm, commonly referred to as the 1.55 μm wavelength range, are suitable for long-distance optical communication because this wavelength range (that actually consists of three bands labeled the S, C, and L bands) has the lowest loss for silica-based optical fibers. On the other hand, the 1.3 μm band has been used for optical communication at high-bit-rates and comparatively short distances because the optical fibers are almost free of wavelength dispersion in this wavelength range.

Until now, InGaAsP thin films grown lattice-matched on InP substrates [1,2] are the most important active material for long-wavelength infrared laser diodes. For the future demands of high-speed optical communication systems, however, parallel processing data transmission using 1D or 2D array laser structures is required. Vertical cavity surface emitting lasers (VCSELs) [3,4] are the most promising structure for this purpose. In the typical VCSEL structure, the vertical resonant-cavity geometry is formed by the upper and lower distributed Bragg reflectors (DBRs) that act as mirrors. In this regar, the DBRs are similar in function to the conventional cleaved mirror facets in conventional edge emitting lasers (EELs). However, for high efficiency, VCSELs need alternating semiconductor stacks with large differences in the indices of refraction between layers. Unfortunately, appropriate DBR pairs that are well lattice-matched to InP substrates do not exist for diodes with InGaAsP active regions. In addition, InP has a larger thermal resistance than that of GaAs, meaning device performance at high temperature becomes very poor. To solve this problem, researchers have explored alternate approaches, e.g., (1) novel material systems that can be grown on GaAs substrates in order to use high-performance Al(Ga)As/GaAs DBR pairs [5], (2) AlGaAs oxide confinement technique [6], and (3) to operate the VCSEL at a higher temperature.

Recently, InGaAsN and GaAsSb have been studied intensively as the candidates for long-wavelength infrared laser diodes because the energy bandgaps of these semiconductor materials are in the wavelength range of interest in optical fiber communication. Moreover, GaAs substrates are currently much cheaper and have a larger area than commercially available InP substrates, and the processing for GaAs is well established. Therefore, we can obtain several benefits by using GaAs substrates rather than InP substrates for VCSEL device production. In this research, we have investigated GaAsSb layers with various barrier materials grown on GaAs substrates by metalorganic chemical vapor deposition (MOCVD) to study the feasibility of fabricating 1.3 μm laser diodes capable of operating at low thresholds at room temperature.

1.2 FEASIBILITY OF III-AS-SB SEMICONDUCTORS FOR 1.3μM LASER DIODES

The Group III-arsenide-antimonide-based semiconductor material system has attracted a great deal of attention for the realization of optical devices like long-wavelength LEDs [7], infrared (IR) detectors [8,9], and mid-infrared lasers [10] as well as electronic devices [11,12,13]. This is because, except for AlAs and AlSb, these materials (GaAs, InAs, GaSb, InSb, and most of their related ternaries and quaternaries) are direct-bandgap compound semiconductors crystallizing in the stable zincblende structure. Furthermore, for heterojunction bipolar transistors, the type-II band lineup between GaAsSb and InP can be use as a base-collector junction that does not exhibit a current blocking effect [14]. For optical devices, direct-bandgap materials are preferable because they have much better light-emitting and receiving efficiency than indirect bandgap materials. These materials can cover a wide range of wavelengths from the near IR to far IR (1.0 μm~3.0 μm) that is used for light-emitting and detecting devices. Recently, GaAsSb strained quantum-wells (QWs) grown on GaAs substrates have been attracting a large amount of interest for laser diodes which operate in the wavelength region at ~1.3 μm for high-bit-rate optical fiber communication systems.

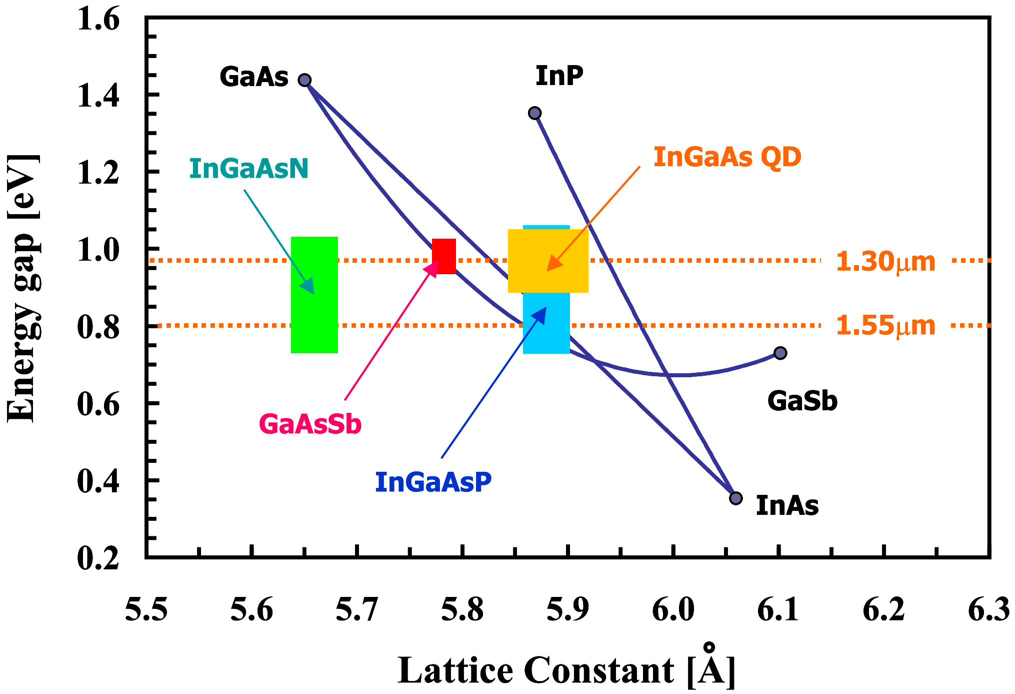

Figure 1.1 Lattice constants vs. energy gaps for various semiconductor materials and their suitability for optical fiber communication.

As shown in Figure 1.1, there are several possible material candidates for 1.3 μm laser diodes. Besides the widely used InGaAsP, InGaAs QDs, and other materials such as InGaAsN [15], and GaAsSb have recently been studied for this purpose. Ternary compound semiconductors are generally much easier to grow than quaternary compound semiconductors in terms of controllability of compositions and reproducibility, and furthermore, nitrogen (N) incorporation into epitaxially grown III-V semiconductors as a host (or matrix) element is quite difficult [16]. For these reasons, the ternary compound semiconductors such as InGaAs and GaAsSb are preferable from the point of view of epitaxial growth. First, InGaAs has actually been used for a long time in optoelectronics. One major application is for the active region in optical pumping sources at the wavelength of 980 nm for Er-doped fiber amplifier (EDFA) in 1.55 μm long-haul optical fiber communications systems [17], and the other application is for long-wavelength photodetectors [18]. There have been attempts to make long-wavelength lasers operating at wavelengths longer than 1.3 μm with InGaAs quantum well (QW) active layers [19], but due to the large lattice mismatch of InGaAs relative to GaAs substrates (7.4% misfit between GaAs and InAs), only lasers operating at much shorter wavelengths than 1.3 μm are possible using InGaAs QW active regions. Although InGaAs quantum-dot (QD) laser diodes [20],21,22] have been reported at wavelength around 1.3 μm, the output power is still very low because of the small optical gain in QDs. As another approach to achieving InGaAsP active VCSELs with AlGaAs/GaAs DBRs on GaAs substrate, wafer fusion bonding has been researched [23,24,25]. However the complex process of double fusion bonding is a big hindrance for the commercial application of this approach.

For the same reason that GaAsSb [26] has large lattice mismatch (7.8% misfit between GaAs and GaSb – it is greater than that of the InGaAs case) relative to GaAs substrates, it seems much less suitable for long-wavelength light emitters beyond 1.3 μm. Unlike InGaAs, however, GaAsSb has a large bowing parameter (1.2 eV) of the energy gap (E_g) vs. alloy composition curve [27], so in spite of a large mismatch to GaAs, GaAsSb can be a good candidate for 1.3 μm laser diodes with a smaller Sb composition than is expected from a simple linear relation of E_g between GaAs and GaSb.

1.3 PROPERTIES OF III-AS-SB

For the development of optoelectronic devices, it is very important to know the electrical, mechanical and thermal properties of the compound semiconductors that are to be used in the applications. The better the knowledge of these parameters, the better we can design and characterize accurately the layers and structures that we grow. Some interesting parameters of ternary end-point materials at 300 K are listed in Table 1.1 below. The intermediate parameters of ternary semiconductors can be derived from these binary semiconductors by using Vegard's law (except for the energy gap relationship) according to the variation of binary composition. In Vegard's law, any ternary parameters are linear function of binary compositions.

Table 1.1 Properties of interesting III-arsenide and III-antimonide binary semiconductors [28].

Property		**Unit**	**GaAs**	**InAs**	**GaSb**	**InSb**
Bandgap	E_g	**[eV]**	1.424	0.354	0.724	0.180
Lattice constant	a	**[Å]**	5.65325	6.05830	6.09593	6.47937
Effective mass	m_n	**[m_o]**	0.063	0.024	0.220	0.014
	m_{hh}	**[m_o]**	0.500	0.430	0.280	0.400
	m_{lh}	**[m_o]**	0.076	0.026	0.050	0.015
Mobility	μ_n	**[cm^2/Vs]**	9200	$2\sim3.3\text{x}10^4$	3750	$7.7\text{x}10^4$
	μ_h	**[cm^2/Vs]**	400	450	680	850
Elastic modulus	C_{11}	**[10^{11} dyn/cm^2]**	11.9	8.329	8.834	6.669
	C_{12}	**[10^{11} dyn/cm^2]**	5.38	4.526	4.023	3.645
Dielectric constant	$\varepsilon(0)$		13.18	15.15	15.69	16.8
	$\varepsilon(\infty)$		10.89	23.25	14.44	15.68

In this study, the primary practical concerns are the growth of GaAsSb epitaxial layer by MOCVD, and the optical properties of the grown layers as required for the active layer of a laser diode. From Table 1.1, the lattice constants of GaAs and GaSb have a huge difference (5.65325 Å and 6.05830 Å, respectively). This means that when GaAsSb is grown on a GaAs substrate, the GaAsSb is under compressive strain because the bigger lattice constant material is grown on a smaller lattice constant substrate. As the Sb composition increases, the compressive strain in the GaAsSb becomes greater. For high Sb compositions, it is impossible to grow GaAsSb films on GaAs without misfit dislocation generation for films over some thickness (this value is known as the critical thickness, h_c) [29,30]. For example, the critical thickness of $GaAsSb_{0.3}$ on a GaAs substrate is less than 100 Å [31]. Therefore, the strain effect places practical limits on the growth of thick single QW or multiple QWs which are desirable for improving the gain in QW laser structures. However, there is another advantageous effect in the elastic compressive strain of semiconductor thin films. When a semiconductor material is under compressive strain, the degenerate valence heavy-hole and light-hole bands split into two separate bands and the heavy-hole band changes to have light-hole-like behavior [32], resulting in a decrease of the effective density of states in the valence band. This change helps a laser diode to operate at a lower threshold current density. Another important feature of the large difference in lattice constants is that it can result in a miscibility gap for the materials in a wide range of alloy compositions. This will be discussed in detail in next section.

1.4 CHALLENGE POINTS IN THE GROWTH OF GAASSB

In growing GaAsSb epitaxial layers, there are four major challenges to obtain high-quality and high-performance epitaxially grown layers. First of all, the lattice constants of GaAs and GaSb are much different. As mentioned earlier, since we want semiconductor materials that emit near the wavelength of 1.3 μm and are compatible with AlAs/GaAs DBRs, the substrate should be GaAs. The huge difference of lattice constants results in highly compressively strained GaAsSb layers on GaAs. As discussed above, It is well known that moderate compressive strain reduces the threshold current by the splitting the valence bands and changing the shape of the heavy-hole band to light-hole-like band. On the other hand, in the high-strain region, the grown layer must be thinner than the critical thickness (h_c) so as not to generate misfit dislocations in the grown layer. However, restricting the highly compressive strained thin layer to a thickness less than h_c results in a severe drawback of decreasing the emission wavelength due to the increased transition energy from conduction band to valence band caused by compressive strain and the quantum-confinement effect of the thin layer. To overcome these problems, strain-compensated (SC) layers that have tensile strain, which is opposite to compressive strain, were proposed [33,34]. We also have used Ga-rich InGaP (over 51% of Ga) and low P composition (less than 30%) GaAsP as SC layers. Although the SC approach basically cannot solve the increased transition energy due to compressive strain effect, by employing SC layers as barrier materials, it enables the growth of thicker QW or multiple QWs of GaAsSb active layer over h_c without any misfit dislocation generation, hence the compensation for the compressive strain effect and quantum confinement effect.

The second problem is the wide alloy composition range of the GaAsSb miscibility cap ($0.2 < \text{Sb} < 0.8$) when mixing GaAs and GaSb [35,36,37]. If two binary semiconductor materials that have large difference in lattice parameters, for example GaAs and GaSb, are mixed together to form an alloy, it is hard to avoid the phase separation of two binary materials below the critical temperature (T_c). Thermodynamics can be used to predict the occurrence of spinodal decomposition or phase separation. By using a straightforward regular-solution model [38], the mixing enthalpy and entropy of binary solutions A(GaAs)+C(GaSb) can be expressed in a simple way. Mixing entropy is defined by Equation 1.1:

$$\Delta \boldsymbol{S}^{M} = -\boldsymbol{R} \cdot [\boldsymbol{x} \ln \boldsymbol{x} + (1-\boldsymbol{x}) \ln(1-\boldsymbol{x})] \qquad \text{Equation 1.1}$$

where R is the gas constant having 8.31J/(mol•K) and x is the Sb composition in GaAsSb. The mixing enthalpy is the sum of nearest-neighbor bond energies.

$$\Delta \boldsymbol{H}^{M} = \boldsymbol{x}(1-\boldsymbol{x})\Omega \qquad \text{Equation 1.2}$$

where Ω, the interaction parameter, is

$$\Omega = \boldsymbol{Z}\boldsymbol{N}^{0}[\boldsymbol{H}_{AC} - \frac{1}{2}(\boldsymbol{H}_{AA} + \boldsymbol{H}_{CC})] \qquad \text{Equation 1.3}$$

In Equation 1.3, Z is the number of nearest-neighbors, N^0 is Avogadro's number, and H_{AC}, H_{AA} and H_{CC} are nearest-neighbor bond energies. In addition, the Gibb's free energy of binary alloy mixing is the most important quantity for calculation of phase diagram and it is related to mixing enthalpy and mixing entropy as described by the following relationship:

$$\Delta \boldsymbol{G}^{M} = \Delta \boldsymbol{H}^{M} - \boldsymbol{T} \cdot \Delta \boldsymbol{S}^{M} \qquad \text{Equation 1.4}$$

With using these equations and the experimental value Ω of 4.00 kcal/mol [39], it is possible to calculate the excess-free energy curves as a function of Sb composition x at various temperatures for $\mathrm{GaAs_{1-x}Sb_x}$ as shown in Figure 1.2. The large positive mixing enthalpy with a large difference in lattice constant can overwhelm the negative mixing entropy, resulting in mixing Gibb's free energy with an upward curve in the center of the composition region, below the critical temperature (in Figure 1.2, T_{c} is around 760ºC).

This means that at equilibrium, the mixing composition within the upward curved region is not stable and the alloy decomposes into a mixture of two phases. Therefore, it is theoretically impossible to grow an alloy within the miscibility gap by any equilibrium growth technique e.g., liquid phase epitaxy (LPE), at temperatures below T_c.

However, under certain conditions, the alloys in the miscibility gap can be successfully grown even at lower temperatures than T_c by non-equilibrium growth techniques such as MBE or MOCVD. The successful growth of metastable epitaxial layers was attributed to the use of near unity V/III ratios, lower T_g, and a fast growth rate. All these conditions tend to minimize the diving force that forces the alloy to its equilibrium state. Phase separation is purely related to thermodynamics, but during the growth of an epitaxial layer, kinetics is also involved in the process. Therefore, controlling the kinetic parameters can affect the thermodynamics, such that even near the T_c, composition fluctuation due to the phase separation can be happen.

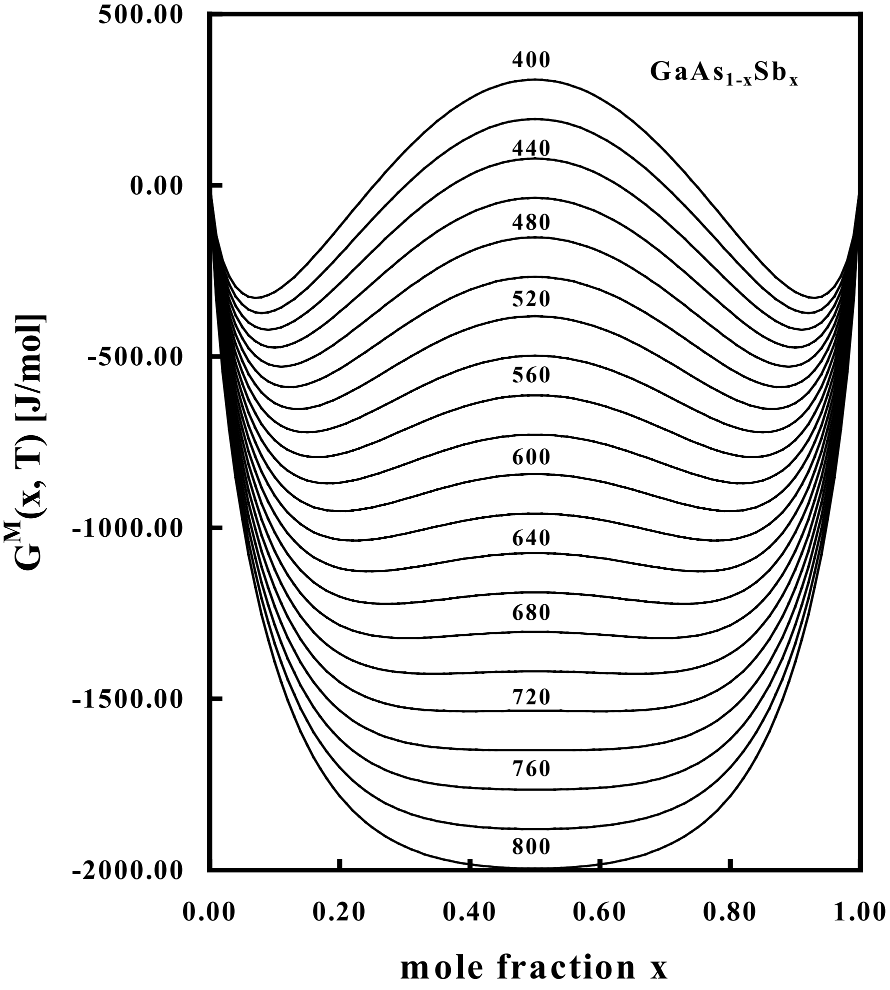

Figure 1.2 Calculated excess-free energy as a function of *x* at different temperatures for $GaAs_{1-x}Sb_x$.

The third problem takes place when GaAsSb is grown on a GaAs substrate or on a GaAs barrier. Since two semiconductors of different bandgaps are brought together to form a heterostructure interface, the energy band lineup between the two materials plays an important role in the performance of optoelectronic devices.

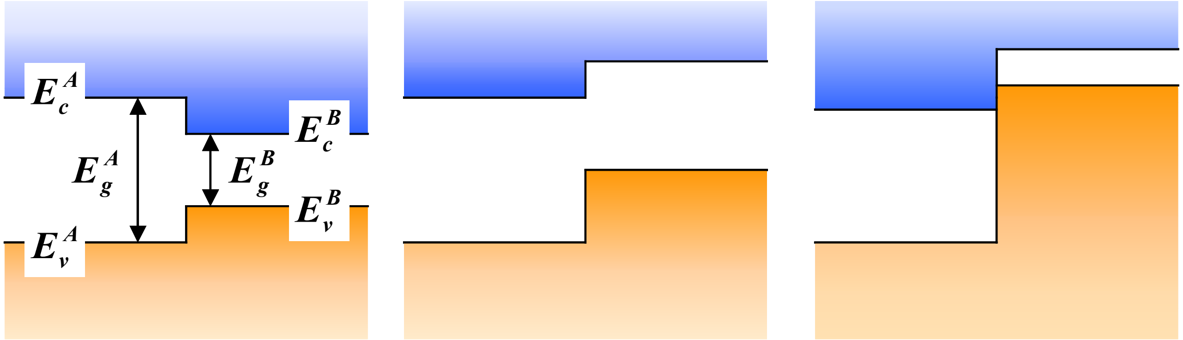

(a) Type-I **(b) Type-II** **(c) Type-III**

Figure 1.3 Various possible band lineups in heterostructure interface.

Figure 1.3 depicts various possible band lineups at heterostructure interfaces. When excess electrons and holes are likely to reside in the conduction band and valence band of the smaller bandgap semiconductor (in material B of Figure 1.3 (a)), respectively, it is called a Type-I or straddling band lineup. This type of band lineup is the most common and is the preferred heterostructure interface type for optoelectronic device applications. Figure 1.3 (b) shows a so-called Type-II or staggered band lineup, where the bands favor excess electrons in the larger E_g semiconductor and excess holes in the smaller E_g semiconductor. If a QW structure is made of two semiconductors with a Type-II band lineup, then the holes can be confined in the QW valence band, but since the smaller E_g semiconductor cannot form a QW for electrons in this case, confinement for electron is impossible and electrons spread out into the barrier materials. Therefore, laser diodes having a Type-II band lineup have poor optical characteristics.

The third possibility, when the two semiconductor bandgaps do not overlap at all, results in a Type-III [40] or broken-gap lineup heterostructure interface (Figure 1.3 (C)). A Type-I band lineup has been reported for $GaAs_{1-x}Sb_x$/GaAs heterostructure interfaces [41]. Most theoretical calculations and experimental data, however, show that the band lineup for this system is Type-II [42,43]. Strong evidence for Type-II band lineup was given in recent reports [44,45]. It is convenient to define a parameter that is related to valence band positions and bandgaps of both semiconductors, hence the band lineup. The valence band discontinuity ratio (Q_v) is defined in Equation 1.5.

$$Q_v = \frac{E_v^w(x) - E_v^b}{E_g^b - E_g^w} \qquad \text{Equation 1.5}$$

In the equation, the superscript "*w*" and "*b*" denote well and barrier, respectively. From this definition, if Q_v is less than unity, the heterostructure interface has a Type-I band lineup; if it is greater than unity, this system has a Type-II band lineup.

For example, the Q_v values for GaAsSb/GaAs in the references [42,43, 44,45] are in the range from 1.05 to 2.0. To obtain a better optical confinement and high-temperature operation, alternate semiconductor barriers that have a Type-I band lineup with GaAsSb are required. The barrier materials should have the conditions of larger bandgap than that of GaAs and lattice matching to GaAs substrates. If the barriers can be grown in a tensile strained condition on a GaAs substrate, we are able to take additional advantage of strain-compensation. InGaP and GaAsP barriers are investigated for both of these purposes in this research.

Finally, the fourth challenge is the narrow window of optimal growth conditions. Since the GaAsSb material should be grown at quite low temperature and with very reduced V/III ratio, the temperature compatibility with other layers (e.g. AlGaAs, or InGaP) and gas switching sequence from high V/III ratio to low V/III ratio, and vice versa are significantly important in the growth of good quality GaAsSb layers.

1.5 PROGRESS IN GAASSB SEMICONDUCTOR LASERS

In 1998, Anan, et al., (NEC, Japan) reported the first GaAsSb edge-emitting laser (EEL) structure grown on (100) GaAs substrates using GSMBE [46]. The structure was a single quantum well graded-index separate-confinement heterostructure (SQW-GRIN-SCH) and GaAs/GaAsSb was used as barrier and QW. It lased at a wavelength of 1.22 μm under pulsed operation (1.0 μs pulse width and 1 kHz pulse repetition rate). Although the lasing wavelength is far shorter than interesting 1.3 μm regime and threshold current density (J_{th}) is high even in pulsed operation mode, this report is considered very important as the starting point of laser diode with GaAsSb active regions.

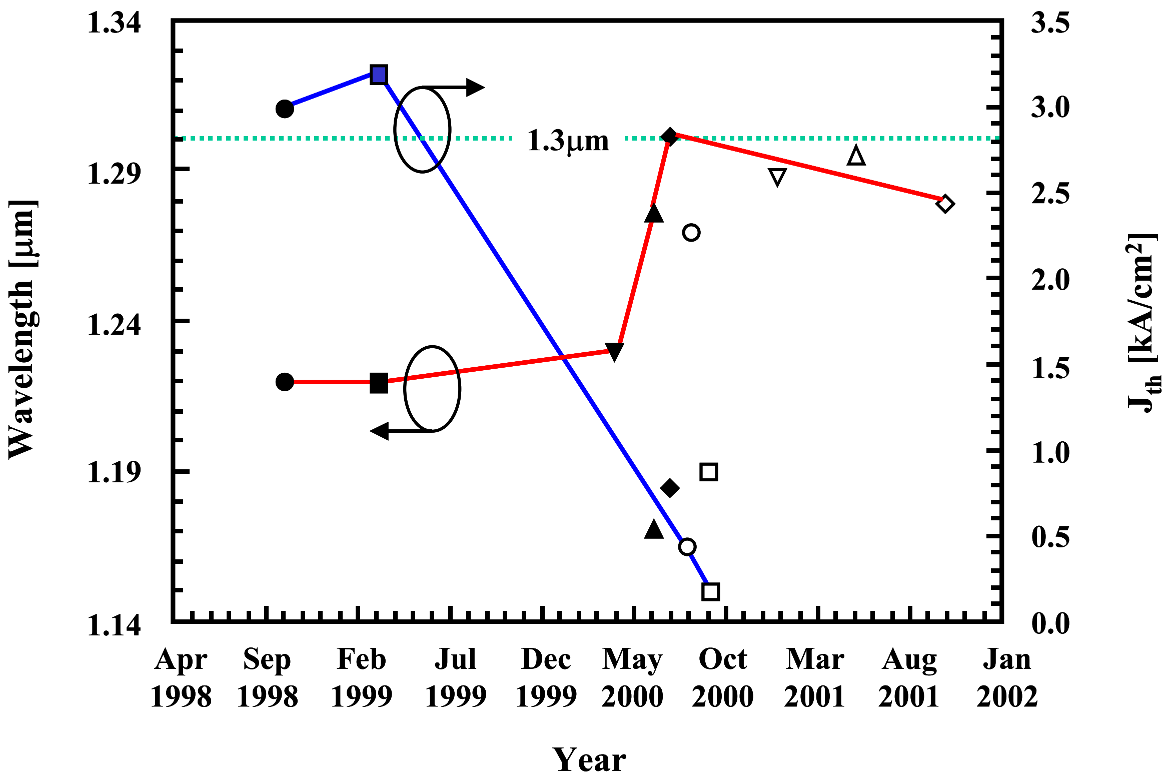

Figure 1.4 Progression in GaAsSb active laser diodes. Data points are from the work of Anan et al. [46,47,48] (●, ■, △), Yamada et al. [49,50] (▼, ◆, ○), Blum et al. [51] (▲), Ryu et al. [52] (□), and Quochi et al. [53, 62] (▽, ◇).

The same group made another big success in 1999 [47]. They fabricated a GaAsSb VCSEL for the first time with a double QW (DQW)-GRINSCH. The characteristics of the device are similar to their previous report. The lasing wavelength was still limited to 1.22 μm and only pulsed operation was possible. The output power was 0.23 mW. The DBR pairs were AlAs/GaAs 25.5 pairs for lower mirror and 18 pairs for upper mirror. In Figure 1.4, progress in the performance of GaAsSb active laser diodes is shown. In 2000, Yamada el al. (same group as Anan) demonstrated continuous-wave (CW) operation GaAsSb VCSEL for the first time [49]. The lasing wavelength was increased slightly to 1.23 μm and CW output power was only 0.1 mW. However, the threshold current (I_{th}) was 0.7 mA, a very low level. The unique fact in the report is they have used two different growth systems to improve the material quality. Usually, DBR pairs need several tens of alternate semiconductor pairs to get a large enough reflectance over 99.5% for both lower and upper mirrors. MBE offers controllability in the grown material thickness that is also needed in DBR mirror but due to the very slow growth rate, it takes very long time to grow a full VCSEL structure. However, sometimes this long growth sequence deteriorates the material quality. In order to grow good quality GaAs/GaAsSb laser structures, a three-step thermal cycling growth technique is required because the DBR and cladding layers that consist of AlGaAs need a higher growth temperature and GaAsSb QWs grown at low temperature have better quality. Yamada et al. employed MOCVD for the thicker part of the structure at high T_{g} and GSMBE for the GaAsSb QWs at low T_{g}. By means of using two growth systems, they could minimize the total growth time and avoided degradation of the QWs. This was followed by the report of Blum et al. of increased wavelength with using normal solid-source MBE on (100) GaAs substrates [51]. The wavelength reached 1.275 μm and J_{th} was reduced to 535A/cm^2 in pulsed operation. They also measured the wavelength shift with device operation temperature and it was 3.1 Å/ºC. Finally, in 2000, Yamada el al. demonstrated a record high 1.3 μm EEL with a triple quantum well (TQW)-GRINSCH and 1.27 μm VCSEL with a DQW-GRINSCH with using the same dual growth system technique [50]. The output powers of the devices were 8 mW and 10 mW in pulsed mode, respectively. Ryu et al. [52] made a report of a fully MOCVD grown GaAsSb DQW-SCH EEL with a very low J_{th} of 190 A/cm^2. Although the wavelength property of the device was not promising, i.e. lasing wavelength is only 1.19 μm, it is very important that they confirmed the feasibility of fully MOCVD grown GaAsSb laser structures on GaAs substrates. They have used an unusual GaAs (100) substrate oriented 15º tilted toward <111>A direction GaAs substrates instead of the more usual (100) on-axis substrates that all other research groups have been using. Since a large off-angle substrate creates a short terrace spacing on the surface and steps or kinks are thought to be more stable than terraces in terms of bonding energy, a small kinetic driving force could result easily in thermodynamic equilibrium of the grown materials. Therefore, it is disadvantageous to use large off-angle substrates for the growth of metastable semiconductor materials like GaAsSb because the strong driving force toward thermal equilibrium causes phase separation in the material. Anan et al. reported the temperature-dependent properties of DQW-SCH VCSELs for a lasing wavelength at 1.295 μm (the longest ever in a VCSEL) [48]. The maximum operation temperature went up to 70 ºC in CW mode. The characteristic temperature (T_0) was 119 K in the range from 20 ºC to 60 ºC. Quochi et al. also successfully fabricated VCSELs with DQW-GRINSCH [53,62]. However, their structure was not grown fully by MBE. They used a dielectric mirror (SiO_2/TiO_2) as the upper DBR pairs. Moreover, these devices lased only in an optically pumped operation mode. The lasing wavelength achieved in the device was 1.288 μm.

As described above, there has been a great performance improvement during a short period, but the performance is still not sufficient for commercial usage. In spite of several benefits of MOCVD growth, laser structures grown entirely by MOVCD are still very uncommon. The major goal of this study is to grow good quality GaAsSb active layer on GaAs substrate with only using MOCVD and to develop long-wavelength emitter with this GaAsSb for optical communication.

Chapter 2: Metalorganic Chemical Vapor Deposition

This chapter discusses the general features of MOCVD growth process and experimental apparatus. All epitaxial semiconductor structures in this study are grown by low-pressure metalorganic chemical vapor deposition (MOCVD). The MOCVD sources, the growth process, and experimental system will be covered in this chapter.

2.1 INTRODUCTION TO MOCVD

It is somewhat controversial who is the first inventor of metalorganic chemical vapor deposition (MOCVD) because of the appearance of some earlier patents that were not published in the scientific literature. Nevertheless, the significance of the early work of Manesevit, et al. [54] cannot be underestimated. Their efforts in growth of a wide range of III-V, II-VI, and IV/VI semiconductors lead to the development of MOCVD growth of devices in the late 1970s. Early doubts concerning the purity of these grown materials were eliminated by the reports of high-purity GaAs with extremely high mobility exceeding about 1×10^5 $cm^2/V\cdot s$ at low-temperature [55] and the demonstration of the first continuous-wave (CW) quantum-well (QW) injection laser operating at 300 K [56]. MOCVD is a non-equilibrium vapor-phase process for deposition of a single crystalline epitaxial layer of semiconductor on a single-crystal substrate. Before the development of MOCVD, epitaxial growths were performed mainly with using liquid-phase epitaxy (LPE) and vapor-phase epitaxy (VPE) such as halide VPE or hydride VPE. Since both of these previously developed epitaxial growth processes had problems in the growth of superlattices and Al-containing materials, these processes were replaced quickly by the superior epitaxial growth methods of molecular beam epitaxy (MBE) [57] and MOCVD. Although MOCVD has several problems including expensive source materials, hazardous properties of source materials (metalorganic sources are pyrophoric and hydride sources are extremely toxic), a large number of parameters such as flow rates, V/III ratios, growth temperature (T_g), growth pressure (P_g), source temperatures, etc. that must be precisely controlled to obtain good uniformity and reproducibility of grown layers, it is thought to be superior to MBE from an economical point of view. The reason is that usually MBE has a very low growth rate, and frequent downtime for maintenance, leading to limited throughput.

In the earliest work on the GaAsSb system, epitaxial film growth was performed mostly by LPE [58,59]. Since LPE is the equilibrium deposition technique and GaAsSb has a wide range of solid compositions over which any solid solution is not stable at normal growth temperatures due to spinodal decomposition as discussed above, Sb incorporation into GaAsSs was limited to very low Sb compositions. The growth of metastable GaAs-GaSb alloys within the miscibility gap, even at the middle point of the alloy, $GaAs_{0.5}Sb_{0.5}$, was reported to be possible with non-equilibrium techniques such as MBE [60,61] and MOCVD [36] under growth conditions employing relatively low V/III ratios. Employing a near unity V/III ratio freezes Group V elements in the manner of a random distribution on the surface of substrate, resulting in metastable GaAsSb alloys of almost perfect average homogeneity. Recently, with the metastable growth techniques, several research groups reported the growth and fabrication of GaAsSb active laser diodes emitting close to 1.3 μm [50,62]. However, almost all of the structures were grown by MBE or modified-MBE such as gas source MBE (GSMBE).

In this study, in order to take advantage of the MOCVD process, GaAsSb layers have been grown by MOCVD on (100) GaAs substrates at low pressure and quite low temperatures (450ºC~590ºC). Triethylgallium (TEGa) is used as Group III source and trimethylantimony (TMSb) and arsine (AsH_3) are used as Group V sources to grow GaAsSb.

2.2 MOCVD SOURCES AND GROWTH PROCESS

For better understanding of the epitaxial growth of III-V semiconductor layers by MOCVD, it is essential to explore the properties of the MOCVD sources and the growth process. MOCVD system uses metalorganic (MO) sources as the Group III elements (exceptionally the Sb source in the form of MO is common due to the instability of its hydride form) and hydride sources as the Group V elements. The growth process is simply expressed by following equation [63]:

$$\boldsymbol{R}_3\boldsymbol{M} + \boldsymbol{EH}_3 \rightarrow \boldsymbol{ME} + 3\boldsymbol{RH} \qquad \text{Equation 2.1}$$

where *M* is the group III metal (such as Ga, Al, In), *E* is the group V element (such as As, P), *R* is Alkyl radical (such as CH_3 or C_2H_5), and *H* is hydrogen. Here R_3M and EH_3 denote MO source and hydride source, respectively. For a simple example, consider the GaAs formation by the chemical reaction from triethylgallium (TEGa) and arsine (AH_3). The process can be described as follow:

$$(\boldsymbol{C}_2\boldsymbol{H}_5)_3\boldsymbol{Ga}(\boldsymbol{l}) + \boldsymbol{AsH}_3(\boldsymbol{g}) \rightarrow \boldsymbol{GaAs}(\boldsymbol{s}) + 3\boldsymbol{C}_2\boldsymbol{H}_6(\boldsymbol{g}) \qquad \text{Equation 2.2}$$

where l, g, and s are liquid, gas, and solid phases. After reaction, gaseous ethane is produced as the byproduct.

2.2.1 MOCVD Sources

For the epitiaxial growth of III-V semiconductors using MOCVD, usually, metalorganic sources are used for Group III elements and hydride sources are used for Group V elements. The dopant sources are available in both metal-organic and hydride forms. The metalorganic sources are pyrophoric liquids or high vapor pressure solids, which are contained in stainless steel vessels. To deliver the source to reactor, a controlled flow of carrier gas (high purity hydrogen (H_2) or nitrogen (N_2)) is introduced into the metalorganic container. Inside the container, the metalorganic source occupies the lower part of the vessel (most of the metalorganics are liquids at the temperature of use) and above the source top level, due to the vapor pressure of the MO source, there exists a volume that is filled with source gas combined with the carrier gas. The carrier gas is passed or bubbled through the source and collects source molecules from the volume to deliver them into the reactor. To maintain a constant vapor pressure inside the container, the carrier gas is continuously bubbled through the source. Hence the container is also called a "bubbler". Since the molar flow rate of the metalorganic source is related to bubbler operating conditions and should be controlled precisely to produce uniform composition and abrupt interface epitaxial layers, it is necessary to place the bubbler in constant-temperature bath and the incoming carrier gas flow and outgoing source gas flow should be controlled accurately by electronic mass flow controllers (MFCs). In simple form Equation 2.3 gives the relation between the bubbler temperature and the equilibrium vapor pressure over the liquid or solid source phase:

$$Log_{10} P_v = B - \frac{A}{T} \qquad \text{Equation 2.3}$$

where P_v is the vapor pressure of metalorganic source at equilibrium in the unit of mmHg, T is the absolute temperature of the bubble in the unit of K, and A, and B are material constants. In Equation 2.3, the vapor pressure is exponentially proportional to the ambient temperature, therefore, it is very important to control the bubbler temperature precisely. The chemical parameters of typical metalorganic sources that are used in MOCVD growth are shown in Table 2.1.

In most cases, an electronic pressure controller (PC) maintains the total pressure of the outgoing source flow from the bubbler. The molar flow rate of a metalorganic precursor, Q_{MO} can be calculated from the total bubbler pressure, the vapor pressure of the precursor, and the carrier gas flow rate by following equation [64]:

$$Q_{MO} = \frac{P_v}{P_b - P_v} \times \frac{F_c}{V_{STP}} \qquad \text{Equation 2.4}$$

where the unit of Q_{MO} is mole/min, P_v is the vapor pressure [Torr], P_b is total bubbler pressure [Torr], V_{STP} is the molar volume (22.406 liter/mol) of an ideal gas at standard temperature (298.15 K) and pressure (760 torr), and F_c is the carrier gas flow rate [in standard cubic centimeter/min (sccm)].

Table 2.1 Chemical properties of metalorganic sources used in MOCVD growth [65].

Chemical name	Formula	Melting Point [ºC]	Formula Weight	Vapor Pressure [mmHg] $\mathrm{Log}_{10}P_v=B-A/T$	
				A	B
Trimethylgallium (TMGa)	$(CH_3)_3Ga$	-15.8	114.82	1703	8.07
Triethylgallium (TEGa)	$(C_2H_5)_3Ga$	-82.3	156.91	2162	8.08
Trimethylaluminum (TMAl)	$(CH_3)_3Al$	15.4	72.09	2134	8.22
Trimethylindium (TMIn)	$(CH_3)_3In$	88.4	159.93	3014	10.52
Trimethylantimony (TMSb)	$(CH_3)_3Sb$	-87.65	166.85	1709	7.73
Diethylzinc (DEZn)	$(C_2H_5)_2Zn$	-28	123.49	2109	8.28
Carbontetrabromide (CBr_4)	CBr_4	88-90	331.6	2346	7.78

Hydrides sources used for Group V elements and dopant sources are very toxic. It is a major disadvantage of MOCVD growth technique but it is a problem that has been solved successfully by companies and laboratories throughput the world. Although less toxic Group V metalorganic precursors [66,67] have been developed, in this study, only conventional As and P hydride sources are used as Group V elements except for TMSb [68] of Sb source. TMSb is the most common Sb source because of the instability of the other Sb sources in metalorganic or hydride forms. The hydride sources used in the system are 100% pure Megabit™ II grade (manufactured by Solkatronic) arsine (AsH_3, purity ≥ 99.99994%) and phosphine (PH_3, purity ≥ 99.9999%). Since the container pressure of the pure hydride is lower than that of the mixed one balanced with H_2, and the total amount of hydride in pure case is much more than that of mixed one, it is possible to reduce the rapid spread of toxic gas when it leaks, and the number of container changes (the chance of gas leak and line contamination is very high when changing the container). Theses are the benefits of using pure hydride.

The hydride molar flow rate of a hydride, Q_H can be calculate by following equation:

$$Q_H = \frac{Mixture\ \%}{100} \times \frac{F_H}{V_{STP}} \qquad \text{Equation 2.5}$$

where F_H is the hydride flow (sccm) which is controlled by MFC, V_{SPT} is the molar volume (22.406 liter/mol), and mixture % is the hydride percentage in balance gas, H_2. In our pure hydride case, it is 100, therefore the hydride molar flow is given simply by F_H/V_{STP}.

Two molar flow rates provide very important MOCVD parameters. The V/III ratio is defined by Q_H/Q_{MO}. In most cases of III-V semiconductor film growth by MOCVD, the growth ambient is over-pressurized with the Group V element to prevent the vaporization of Group V element from the epitaxial surface, which happens because of more volatile property of Group V element than the Group III element. In order to maintain a higher partial pressure of the Group V element in reactor, a relatively high V/III ratio is required. This requirement is reversed in III-Sb semiconductor growth. Due to the extremely low volatility of Sb, an almost unity V/III ratio is key a factor to grow high-quality III-Sb materials [35].

Sources for n-type dopants are usually hydrides and p-type dopant sources are usually metalorganics. The maximum doping concentration in most semiconductor epitaxial layers is high × 10^{18} to middle × 10^{19} per cm^3. It is very high concentration range but still is a fairly small amount compared to the matrix elements ($\sim 10^{22}/cm^3$). To introduce a low molar flow rate into reactor, the disilane (Si_2H_6) hydride source employed here is only 10ppm in balance H_2 and the p-type dopant source molar flow rates, specifically, the metalorganic precursors such as diethylzinc (DEZn) and carbontetrabromide (CBr_4) are controlled by adding a H_2 flow through a dilution line.

In this study, sources used for MOCVD epitaxial growth are conventional metalorganics for Group III elements and hydrides for Group V elements, including triethylgallium (TEGa), trimethylgallium (TMGa), trimethyl-aluminum (TMAl), and trimethylindium (TMIn) for Group III elements, trimethy-antimiony (TMSb), arsin (AsH_3), and phosphine (PH_3) for Group V elements. Disilane (Si_2H_6), and diethylzinc (DEZn), bis(cyclopentadi-enyl)magnesium (Cp_2Mg), and carbontetrabromide (CBr_4) are used as n-type dopant, and p-type dopants, respectively.

2.2.2 MOCVD Growth Mechanism and Process

In semiconductor crystal growth by MOCVD, the fundamental processes are subdivided into two components of thermodynamics and kinetics. The thermodynamics determines the state of a closed system at equilibrium. However the MOCVD system is not a closed system, so the MOCVD growth process is not an equilibrium process. Thus thermodynamics only defines the growth processes such as the driving force, maximum growth rate, and compositions of the equilibrium phase in the epitaxial layers within certain limits. Since thermo-dynamics deals only with the energy of the system in the initial and final equilibrium state, it is not able to provide any information related to the time required to attain the equilibrium. The MOCVD process is frequently treated as a quasi-equilibrium process, because the growth rate is very small in most cases (this means that the system state changes very slowly from the initial to final state, such that the system seems to be at equilibrium state during a very short time interval.). Even with a state of quasi-thermodynamic equilibrium at the growth interface, the rates of the various processes from the initial input gases to final formation of a solid semiconductor film can be obtained only by kinetics. The kinetics of the MOCVD growth process is divided into two parts: mass transport and chemical reactions. The mass transport controls the rate of transport of source materials to the surface where growth occurs. The chemical reaction can occur in the gas phase (homogeneous reactions) and in vapor/solid phase on the growing surface (heterogeneous reactions). Because the homogeneous reaction does not include the growing surface, the resultant epitaxial layer has poorer quality than that grown in heterogeneous reaction.

The “final state” of the MOCVD growth process is controlled mainly by thermodynamics and kinetics and is intimately related to hydrodynamics and mass transport [69,70]. The growth process can be generally categorized into three process regions by limiting of total growth rate: surface-kinetics limited, mass-transport limited, and a thermodynamically limited case. For relatively low growth temperatures, the growth rate is limited by the surface reaction rate. If the growth temperature increases in this growth region, the reaction rate becomes faster and the growth rate increases. In the kinetically limited region, the growth rate also depends on the crystal orientation. As the growth temperature increases, the surface kinetic energy becomes sufficient and the mass-transport limited process becomes dominant. Since the gas-phase diffusion through the boundary layer to the growth surface is nearly temperature independent, the growth rate is constant in the mass-transport limited process. In this region, the growth rate is directly proportional to the amount of source materials that reach the growth surface and is inversely proportional to the thickness of the boundary layer above the substrate. Because of these effects, increasing the source flow rate and decreasing the reactor pressure well increase the growth rate. As the growth temperature passes the mass-transport limited region, the growth rate starts decreasing as the temperature increases due to various thermodynamic effects and the decomposition of deposited material from the substrate. Since the cracking of source precursors into deposited material (for example of GaAs growth, TMGa and AsH_3 crack to Ga and As on the substrate.) is an exothermic process, the growth rate is limited by thermodynamics at higher temperatures. Of all the growth process regions, the mass-transport limited region is preferable because of its temperature insensitive growth rate.

For MOCVD growth, the heater (resistance, lamp, or RF type heating) provides thermal energy to substrate and this thermal energy is used to pyrolyze the source precursors to their chemically active elementary forms and to drive the reactions. The vapor and solid interface at the substrate surface improves the cracking of sources when the heterogeneous reactions occur. The total growth process is governed by thermodynamics, and kinetics. The hydrodynamics that is closely related to the reactor design affects the boundary layer formation, gas flow characteristic (laminar flow or turbulence), and the gas-phase diffusion of sources. However the whole growth process and reaction mechanisms are not understood fully due to the complex interrelations between them.

2.3 MOCVD SYSTEM

A typical MOCVD reactor system consists of four main parts: the gas handling system, the reactor chamber, the heating system for pyrolysis of source precursors, and the exhaust system. Each part has its unique role and, for a properly designed and constructed system, these components give the reactor the ability to perform state-of-the-art epitaxial growth. All the epitaxial structures that are discussed in this study were grown in an Emcore GS3200-UTM (University of Texas modified) system. The reactor chamber is vertical gas-flow geometry and is a high-speed rotating-disk system. A schematic diagram of MOCVD system is shown in Figure 2.1.

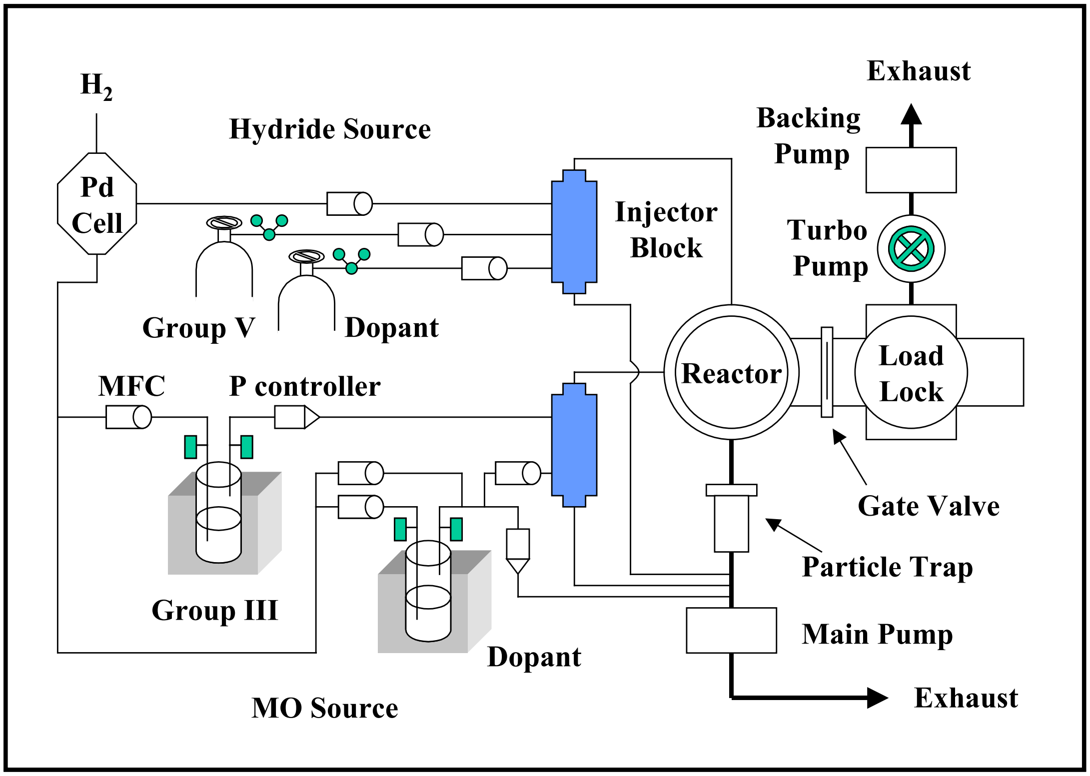

Figure 2.1 Schematic diagram of MOCVD system

2.3.1 Gas Handling System

The main function of the gas handling system is to deliver precisely controlled amounts of the source gases from the gas cylinders and metalorganic containers to the reactor chamber without any contamination. It is subdivided into three sections: (1) source storage, (2) gas delivery tubing, and (3) source and carrier gas control. The Group V hydride sources are high-purity liquids and are contained in high-purity cylinders with specially treated inner cylinder walls. The high toxic property of these materials is a major disadvantage of these sources. For safety purposes, the hydride source cylinders are stored in remote gas bunker and the source pressures and flow rates are controlled by regulator and MFCs and delivered to the reactor through long sections of stainless steel tubing. The metalorganic (MO) Group III sources are liquid or solid forms that are contained in stainless steel vessels, also called bubblers. Usually, hydrogen carrier gas goes into the bubbler and collects source molecules from the vapor that exists in the volume above the MO source. Therefore the vapor pressure of the MO source is an important parameter. Since the vapor pressure of the source dependents strongly on the ambient temperature, it is necessary to maintain a constant bubbler temperature for stable and uniform source supply. In this study, the stainless steel MO source bubblers are placed in constant temperature baths (Neslab RTE-111 or Lauda RC-6) filled with an anti-freezing solution (a mixture of water and ethylene glycol).

The tubing employed in the reactor is electro-polished stainless steel seamless tubing (normally Type 316) in which hydrogen and the hydride and MO sources pass. The shorter the tubing length is, the less the chance of leaks or contamination from the joint points is. However because of the safety issue, fairly long length of hydride source tubing is inevitable. The tubing for the MO sources is wrapped with resistance line heaters to keep the MO source from re-condensing in the tubing.

The gas control part of the MOCVD system assures that precise amounts of the desired sources are supplied into reactor without any fluctuation of source parameters. Every metalorganic source has a computer-contrelled mass flow controller (MFC) that regulates the source flow rate, a pressure controller (PC) that controls the pressure of the line at a certain set point, and valves that are activated pneumatically. By switching the source flows with a computer, even very complicated multilayer structures can be grown easily with a pre-programmed recipe that is a computerized instruction set. There are three manifolds or injector blocks just before the reactor chamber, one each for the hydride line and the two separate MO source lines. The manifolds are an assembly of several run/vent valves. The function of the manifold is to switch each source gas flow into the reactor chamber when the sources are needed for growth or to the exhaust line when the growth is in a pause state or the sources are not required for that layer (for example, TMAl is going to exhaust line, when GaAs is being grown). To maintain steady flows of the source gases, hydrogen push flows are added into the flows going through each manifold.

The purity of the hydrogen used for the metalorganic source transport is critical. The ultra-high-purity (UHP) hydrogen is supplied from a liquid hydrogen tank. It is purified at point-of-use by passing it through a heated pallardium (Pd) cell at ~400 ºC. When the Pd cell is heated, it becomes permeable only to atomic hydrogen. Hydrogen can penetrate the Pd cell wall in the form of protons and the other larger size impurities cannot. Finally, the protons recombine with electrons on the “high-purity” side of the Pd cell membrane and the H_2 purification process is finished.

2.3.2 Reactor Chamber and Heating System

The reactor chamber of the GS3200-UTM is an air-cooled cold-wall stainless steel cylinder type. All the gases are introduced into the reactor chamber from the top gas showerhead. This gas flow scheme is called a vertical reactor type. Inside the reactor chamber, there is a flow showerhead (or flow flange) through which the MO sources and hydride sources are introduced in to the reactor, a high-speed rotating-disk system for achieving a uniform boundary layer above the substrate, a heater system which gives thermal energy to the substrate and to the source precursors to accomplish the pyrolysis reactions, and a thermocouple (K-type, Chromel/Alumel) which detects the temperature of the susceptor holding the substrate and makes it possible to maintain the desired set temperature point with a feed-back loop provided by a temperature controller and a power supply.

The reactor chamber is connected to three subsystems: (1) the top flow flange, (2) the bottom exhaust system, and (3) the side load-lock system. The load-lock system is very convenient subsystem that provides a way to load a new wafer or multiple wafers without opening the whole chamber to the atmosphere. The wafer is loaded on the susceptor and is preheated in the load-lock chamber under vacuum to remove the surface oxygen or moisture with pumping down to low × 10^{-7} Torr by turbo molecular pump. After adequate pre-thermal treatment, the wafer on the platter is carried into reactor chamber using the transport arm and fork system.

The flow flange, which is placed on the top of the reactor chamber, receives the source gases that are injected from the three manifolds. It also is used to introduce a large amount of “shroud” hydrogen flow [~22.5 slm (standard liter per minute)] into the reactor. The shroud flow creates a laminar flow geometry in the growth chamber that permits the MOCVD reactor to produce uniform and controllable epitaxial layers.

The precursor flows containing the metalorganic and hydride sources are directed to wafer carrier (or platter) on which the substrate sits. The platter spins at a very high-speed (~1200 rpm) to create thin and uniform boundary layer over the entire susceptor (and substrate) surface. The high-speed rotating-disk system also improves the temperature uniformity. The susceptor (or platter) is made of a ~5 in. diameter-molybdenium (Mo) circular plate and has a single machined pocket in the middle of it to hold the substrate.

The source precursors that reach at the top of the boundary layer diffuse through it to substrate surface. The thermal energy from the resistance heater provides enough energy for the precursors to crack into their elementary forms. The resistance heater is made of graphite and is located under the wafer carrier. To provide current into the heater, a DC power supply (maximum open-circuit voltage of 60 V and short-circuit current of 80 A) is used. The existence of the free chemical bonds on the substrate surface weakens the molecular bond strength of the adsorbed precursor species, thus increasing the reaction rate for the thin film growth [71]. Since a uniform temperature distribution and precise temperature control are the key factors to achieve high-quality epitaxial layers, an accurate temperature-control system is required. Adequate control is possible by using a feedback loop between the thermocouple, the PID temperature controller, and the power supply. In order to check the temperature calibration and therefore determine the real temperature of the substrate, an Al thin film (~2000Å) deposited on Si wafer is used. When the actual temperature exceeds the eutectic temperature of Al/Si (~573 ºC), the mirror-like surface of the Al film on the polished Si substrate turns hazy because of the formation of an Al-Si alloy at that temperature. By observing the surface change at several temperature-set points, it is possible to calibrate the thermocouple temperature reading. By using this approache, we determined that the real temperature of the substrate is ~50 ºC higher than that of the set point and the thermocouple reading temperature. When the heater system, the thermocouple position, or the thermocouple itself are changed, a temperature calibration is an essential procedure to ensure the real temperature is not incorrectly measured. The Al/Si eutectic method is time consuming but fairly easy and accurate method to calibrate the reactor susceptor temperature.

2.3.3 Exhaust System

In a low-pressure MOCVD system, the main function of the exhaust system is to maintain the reactor pressure at a certain specified value(s) during the growth process (the pressure is usually atmosphere at ~760 Torr or low-pressure at ~60 Torr). In this study all growth runs were taken at a growth pressure of 60 Torr. As the growth pressure is reduced, it causes a reduction of boundary layer thickness, resulting in an increase of the growth rate [72], and a decease of impurity incorporation [73] into the grown layer. Because the growth pressure plays an important role in the properties of the resultant epitaxial layers, a constant, non-fluctuating stable growth pressure is a key factor to obtain reproducible high-quality and uniform epitaxial layers. One of the benefits of low-pressure (LP) MOCVD relative to atmospheric-pressure (AP) MOCVD is a more economical source usage due to the higher growth rate and the ease of achieving high quality layers, if the growth pressure is controlled precisely. The second function of exhaust system is performed by two sub-systems. One is the exhaust filter sub-system which functions to remove and trap the particles or byproducts in the exhaust stream, which are produced during the growth process. The other sub-system is the toxic gas burn box, which burns and oxidizes the residual toxic and reactive gases, therefore converting the chemicals in the reactor exhaust stream into solid waste removed by the filters and harmless gaseous byproducts, primarily water vapor. Because not all the sources react to adhere to the substrate surface where real epitaxial film growth occurs, the remainder of the sources that are not deposited on the substrate should be removed from the reactor chamber and exhaust line so as to not build-up and increase the growth pressure and also to not disturb the normal growth mechanisms. The main process vacuum pump removes the unreacted precursor sources and byproducts in two forms: a solid form of waste byproduct and a gaseous form of the unreacted or partially reacted sources. The gaseous form includes extremely toxic hydride gases of AsH_3 and PH_3. (The threshold limit values (TLV) of those hydrides are 0.05 ppm and 0.3 ppm, respectively. The TLV is an eight-hour time-weighted average concentration believed to be that which most workers may be exposed to day after day, without any harmful effects.) The safe removal of these unreacted and partially reacted materials is one of the essential functions of the exhaust system.

In our MOCVD system, the exhaust system consists of stainless steel tubing, two particle traps, a throttle valve, the main process pump, and the burn box. Fairly coarse byproducts are removed by the first particle trap filled with stainless steel mesh, and fine particles are removed by the second particle trap that is water-cooled and contains a 40 μm sintered stainless steel mesh filter. The throttle valve controls the reactor pressure with an electronic feedback loop between the throttle valve opening and a pressure transducer attached to reactor. The main process pump that is used in the system is a Leybold Trivac D65BCS rotary pump using chemically inert fluorocarbon (*Krytox*) oil. The gases pumped by main process pump go to a burn box (Guardian^{TM} made by ATMI Ecosys) to be burnt and oxidized to become less toxic oxide materials as discussed above.

For safety, a multiport toxic gas detector monitors several important points in the MOCVD system such as the reactor chamber, gas delivery system, and the process pumping unit to check for any toxic gas leak.

Chapter 3: Material Characterization

This chapter discusses the characterization techniques used for optimization of epitaxially grown semiconductor materials. These techniques can be categorized by optical and electrical methods, or destructive and nondestructive methods. It is very important to choose the proper characterization technique according to the properties that we want to measure. Therefore the knowledge of these techniques is essential to the growth of high-quality materials and to the development of high performance devices.

The general characterization techniques including X-ray diffraction (XRD), photoluminescence (PL), electrochemical capacitance-voltage doping profiler (ECV), atomic force microscopy (AFM), cathodoluminescence (CL), secondary-ion mass spectroscopy (SIMS), transmission electron microscopy (TEM), and scanning electron microscopy (SEM) are employed in the work and are described below.

3.1 X-RAY DIFFRACTION

X-ray diffraction (XRD) is a very useful, fundamental and nondestructive (powder method is destructive but not used frequently for III-V semiconductor materials) characterization technique for semiconductor materials, from which the lattice constant, residual strain, alloy composition, etc. can be determined. XRD techniques can be applied to semiconductors to measure the properties of epitaxial thin film in several forms: (1) X-ray rocking curves, (2) double crystal X-ray diffraction (DCXRD) for the determination of the compositions of grown layers, (3) reciprocal space mapping (RSM) to measure the amount of the built-in compressive or tensile strain in films and its relaxation, and (4) glancing incident angle X-ray analysis (GIXA) for epitaxial layer thickness and interface roughness [74,75].

Diffraction is a phenomenon that happens when certain phase relationships exist between two or more waves. It can occur when an electromagnetic wave interacts with a periodic structure whose repeat distance is about the same as the wavelength of the wave. In-phase waves cause constructive interference and out-of-phase waves cancel each other out in their superimposed wave.

In 1912, German physicist von Laue discovered from his X-ray diffraction experiments that X-rays are very short wavelength electromagnetic waves, and that a crystal has a periodic atomic arrangement. His experiments are very important because they showed that the diffraction concept could be applied into crystals. Since any periodic structure has a reciprocal space that is related to the Fourier transform of the real space periodicity, and a diffraction pattern is basically a map of reciprocal space, and we can determine the crystal structure from the diffraction pattern that is obtained by detection of scattered X-rays from the sample. To measure the diffraction pattern, X-ray photons at a wavelength of $\lambda = 1.5405Å$ obtained from a Cu $K\alpha_1$ source are used. This wavelength is chosen since it is comparable to the periodicity spacing of the crystal planes. (In a semiconductor, the typical lattice constant is around 5Å, such that this periodicity or distance between any adjacent parallel lattice planes is on the order of the X-ray wavelength). W. L. Bragg, who was inspired by von Laue’s experiments analyzed his own X-ray diffraction data and was able to express the diffraction condition in a comparably simpler mathematical way than that used by von Laue. The Bragg's law is given by Equation 3.1:

$$2\boldsymbol{d}_{\boldsymbol{hkl}} \sin \boldsymbol{\theta}_{\boldsymbol{B}} = \boldsymbol{n}\boldsymbol{\lambda} \qquad \text{Equation 3.1}$$

where d_{hkl} is the spacing between adjacent lattice planes, θ_B is Bragg's angle between the lattice plane and incident X-ray, n is the order of the diffraction, and λ is the wavelength of X-ray. For the cubic crystal, the spacing d_{hkl} is given by

$$\boldsymbol{d}_{\boldsymbol{hkl}} = \frac{\boldsymbol{a}}{\sqrt{\boldsymbol{h}^2 + \boldsymbol{k}^2 + \boldsymbol{l}^2}} \qquad \text{Equation 3.2}$$

where a is lattice constant of interest in the semiconductor, and (h k l) are the Miller indices of the scanned lattice plane. Bragg's approach in the analysis of DCXRD is very simple and fairly accurate method to determine the ternary semiconductor compositions and the quality of epitaxial layer and its interfacial property. Since lattice constant, (a) of any semiconductor is related to Bragg's angle through Equation 3.1 and Equation 3.2, a can be obtained from the spacing of planes (h k l), d_{hkl} that is calculated from the measured θ_B with fixed wavelength of X-rays. Furthermore, the lattice constant (a) of a ternary compound semiconductor varies with respect to the alloy ratio of the constituent binary semiconductors, such that the composition of the material can be determined from the calculated (a). However, to determine the composition of quaternary semiconductor, both XRD and PL measurements are required because various compositional combinations of constituent elements can correspond to the same lattice constant in a quaternary compound semiconductor. The interfacial properties can be assessed from the

XRD data too. When the adjacent epitaxial layers with slightly different lattice constants have abrupt interfaces, the X-ray diffraction data shows interference patterns in a rocking curve or an ω-2θ curve. It is known as Pendellosung fringe [76]. These fringes are a good indication of the high quality of the interfaces. The full width at half maximum (FWHM) of the measured peak is another important parameter from which to determine the quality of epitaxial layer.

As mentioned above, periodic lattice planes with the same Miller indices in real space have a reciprocal point in reciprocal space by the application of a Fourier transform. In the ideal case of an infinite and perfectly periodic structure, the reciprocal point has delta-function-like shape with infinite intensity and zero spread. However when considering the real crystal structure, theses reciprocal space points will be broadened due to several reasons such as the finite periodicity of the crystal and existence of defects. This can be explained in two ways – by insufficient constructive interference or by the spreading of the reciprocal space points by the Fourier transform of a finite periodic structure. Therefore the narrow FWHM of measured peak is the good indication of high quality material. The peak broadening of a very thin layer like a quantum well is inevitable because of the broadening effect, even though the atomic planes in the layer are perfectly periodic and defect-free.

To evaluate the built-in strain or relaxation of the strain in the epitaxial layer, reciprocal space mapping (RSM) is very useful technique. The von Laue approach that is used in the construction of the Ewald sphere is convenient in this case. The incoming X-ray and outgoing X-ray that make some angle with measured sample are basically probing the reciprocal space point. The condition of the measurement is known as the Laue equation and given by

$$\vec{k}_i - \vec{k}_f = \vec{G} \qquad \text{Equation 3.3}$$

where $\vec{k}_i$ is the wavevector of the incident X-ray beam, $\vec{k}_f$ is the wavevector of scattered X-ray beam, and $\vec{G}$ is the reciprocal space vector that indicates the reciprocal space point being probed. In principle, the Laue equation is equivalent to Bragg's law. The detail of Laue approach can be found in many textbooks of solid-state physics and X-ray diffraction [77].

When the ω-2θ scans are consecutively measured by changing a small amount of ω, it allows getting a map of reciprocal space that the reciprocal space vector $\vec{G}$ is probing over. This measurement technique is called RSM. If RSM is taken at the asymmetric reciprocal space point, it gives much information on the semiconductor structure. To understand this, first, assume a cubic semiconductor structure that has a fully strained epitaxial layer grown on a substrate having a smaller lattice constant. In this case, the epitaxial layer is called compressively strained and if the layer is grown within its critical thickness, it can have a high film quality without any dislocation formation. The in-plane lattice constants that are parallel to the growth interface shrink and fit to the lattice constant of substrate. On the other hand, the vertical lattice constant is elongated in the growth direction (*z*-axis) as allowed by Poisson's ratio. When an asymmetric RSM is taken under the fully compressive strain conditions, the reciprocal space peaks of the substrate and the epitaxial layer are aligned vertically to the reciprocal *x*-*y* plane, but for the reciprocal *z*-axis, the epitaxial layer peak appears close to the origin because the longer lattice in real space matches to the shorter reciprocal lattice. The (115) direction asymmetric RSM of a fully compressively strained $GaAsSb_{0.24}$ epitaxial film grown on GaAs is shown in Figure 3.1.

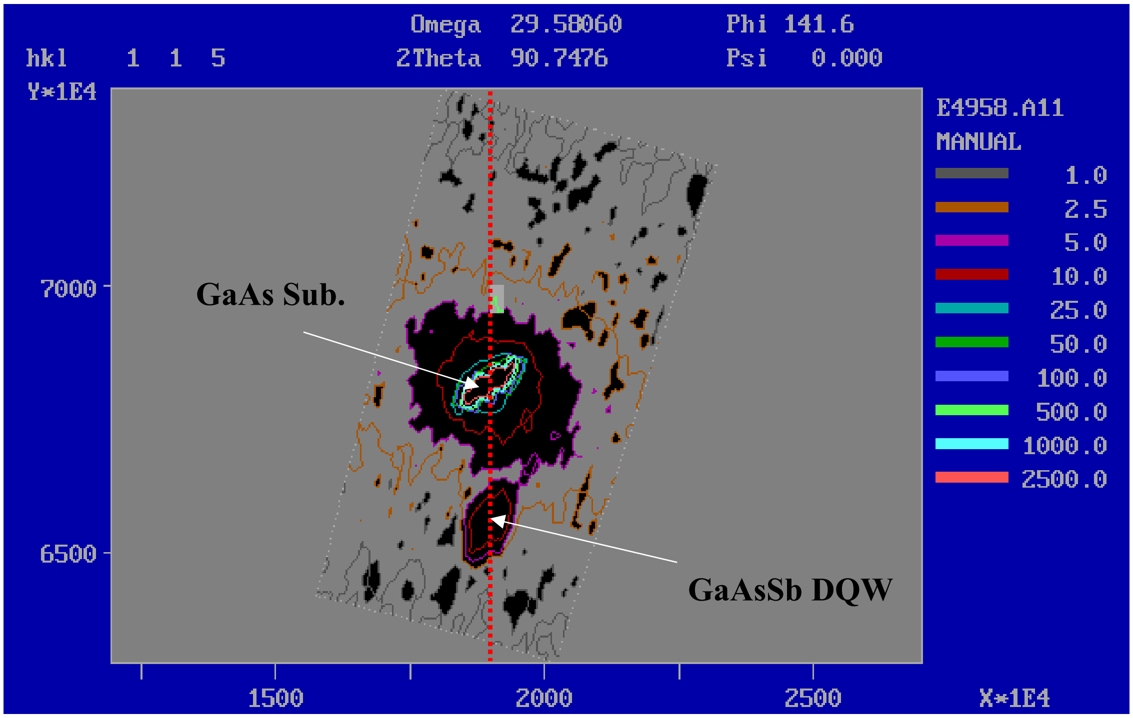

Figure 3.1 (115) XRD RSM of a fully compressively strained $GaAsSb_{0.24}$/GaAs DQW-SCH structure

In the figure, the GaAs substrate and GaAsSb QW peaks are vertically aligned and this means that the GaAsSb layer is fully strained and grown within the critical thickness.

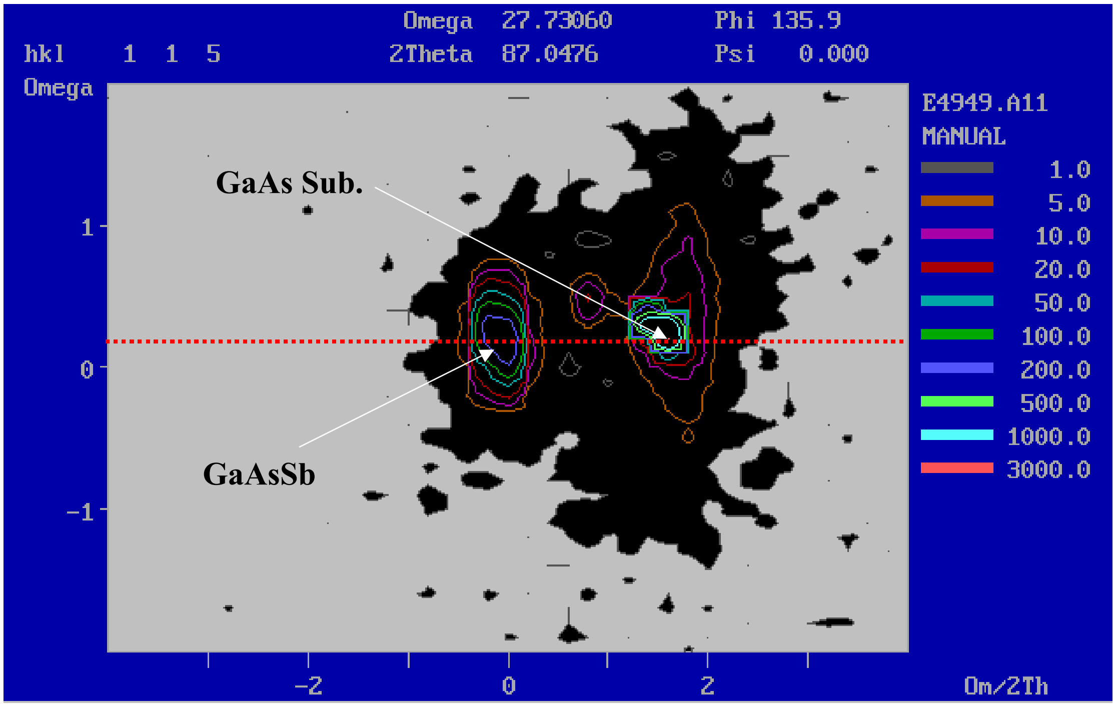

Figure 3.2 (115) XRD RSM of an as-grown fully relaxed GaAsSb$_{0.38}$ layer on GaAs substrate.

As the second case, the asymmetric RSM of a fully relaxed epitaxial layer will be discussed. When a thick semiconductor layer is grown on a substrate with a smaller lattice constant, the compressive strain starts to relax depending on its thickness. If the thickness of the grown layer is much greater than the critical thickness, the strain is fully relaxed and the heteroepitaxial semiconductor structure returns to its original cubic structure by relaxation of all three lattice constants (two from in-plane lattice constants and one from growth direction lattice constant). The compressive strain relaxation can be detected by measuring an asymmetric RSM. For the fully relaxed epitaxial layer, the in-plane lattice constants are not aligned vertically to the substrate any longer. Instead the reciprocal peaks of the film and the substrate are aligned to the origin of the reciprocal space coordinate. In Figure 3.1, the (115) asymmetric RSM of a fully relaxed 6000 Å-thick $GaAsSb_{0.38}$ is shown. The two peaks are aligned horizontally to the origin of the ω axis. From the result, we can conclude that the thick GaAsSb layer is fully relaxed and by measuring the DCXRD of the sample, the Sb composition is determined accurately without any compressive strain effect.

In this study, all XRD data were taken with a *Philips* X'pert MRD high resolution (0.0001°) X-ray diffractormeter, shown schematically in Figure 3.3. Cu Kα characteristic X-ray radiation is used as source for the XRD and it is collimated with a four-crystal Ge (220) monochromator. The monochromator also splits two characteristic lines into Cu Kα_1 (λ = 1.54056Å) and Cu Kα_2 (λ = 1.54439Å). Finally, only the Kα_1 X-ray is illuminated on the sample. The sample stage can be rotated about the θ-axis (or ω-axis, rocking), ϕ-axis (rotation), and ψ-axis (tilt), and can be translated in the *x*, *y*, and *z* direction. The detector can be fixed for the rocking scan or the ω scan. It can be rocked independently for the 2θ scan, or coupled with the sample stage for ω-2θ scan. The system has a secondary optics assembly (detector 2) for rocking curves, and a triple-axis analyzer crystal part (detector 1) for high resolution RSM. The triple-axis section consists of a Ge (110) crystal that is aligned to the Ge (200) reflection.

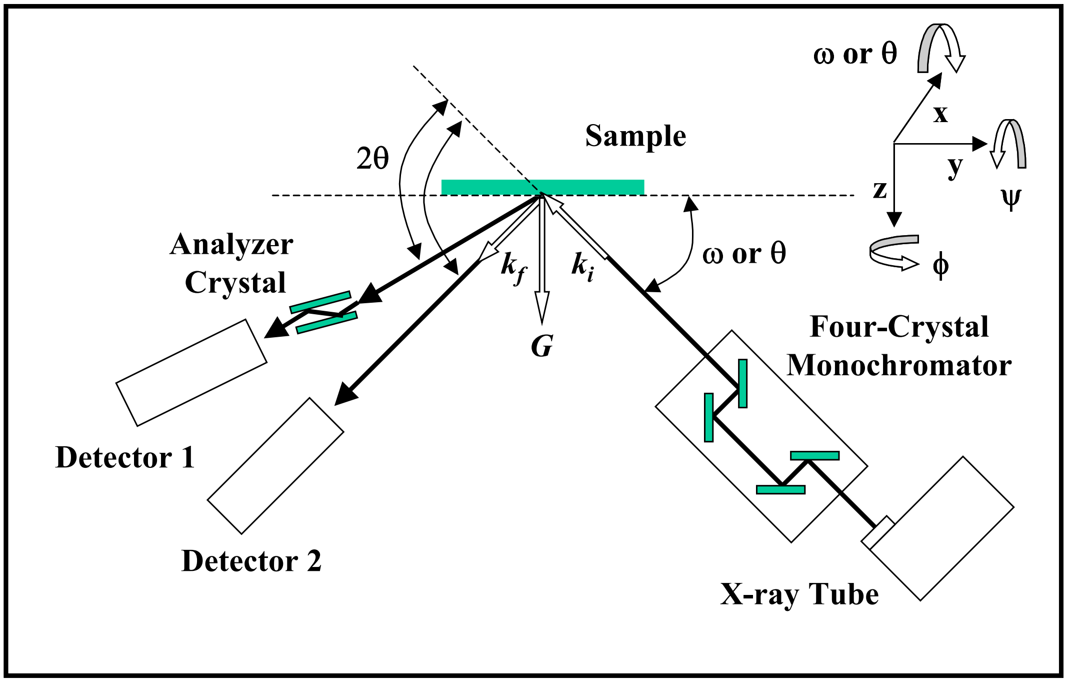

Figure 3.3 Schematic diagram od the Philips X'pert X-ray diffractometer system.

In the Figure, $\vec{k}_i$ and $\vec{k}_f$ are the wavevectors of incident and scattered X-rays, respectively. The end point of $\vec{G}$ is the reciprocal space point that is being probed. The rocking of the sample varies the incident angle, and the reciprocal space point that vector $\vec{G}$ indicates is changed too. Repetition of incident angle changes will make X-ray rocking curves as a function of rocking angle θ (or ω).

The simulation of X-ray rocking curves is very useful to verify the compositions calculated from the X-ray rocking curves, and to ensure the targeted thickness, and the quality of interfaces. Commercially available RADS (Rocking curve Analysis by Dynamic Simulation) software is used for dynamic simulation of sample structures. The (004) DCXRD curve of $GaAsSb_{0.24}$/GaAs DQW-SCH structure that was grown at 530 ºC is shown in Figure 3.4. The simulated curve is well matched to the experimental curve with the structure described in the inset.

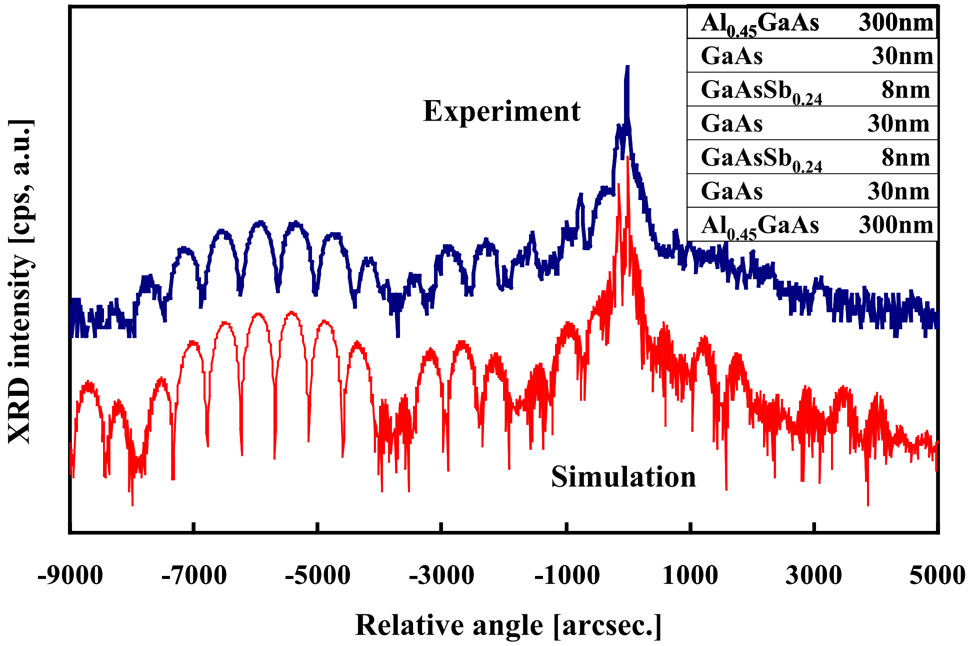

$Al_{0.45}GaAs$	300nm
GaAs	30nm
$GaAsSb_{0.24}$	8nm
GaAs	30nm
$GaAsSb_{0.24}$	8nm
GaAs	30nm
$Al_{0.45}GaAs$	300nm

Figure 3.4 (004) XRD scan and dynamical X-ray diffraction simulation of DQW-SCH.

3.2 PHOTOLUMINESCENCE

Photoluminescence (PL) is one of the most powerful and widely used optical characterization techniques for III-V semiconductors and their alloys because of its simplicity and non-destructive measurement feature. PL provides plenty of information on both bulk and layered semiconductor materials, such as impurities states and defect states, which affect the materials quality and device performance, as well as the bandgap (E_g) of the materials [78].

When a direct bandgap semiconductor is illuminated with high enough energy photons, some of the electrons in the valence band are excited to the conduction band and leave holes in the valence band energy states. Thus, this photon absorption process generates electron-hole pairs (EHPs) in the semiconductor. For the absorption to happen, the incident photon energy should be greater than the bandgap energy of the semiconductor, $h\nu \geq E_g$, where h and ν are the Planck constant and the frequency of incident light, respectively. As currently practiced, PL in most case, employs an excitation light source that is a laser that has the proper excitation energy for the measurement. The excited electrons in the conduction band lose their excess energy into the semiconductor as phonons by a lattice scattering process, and move to the electron states near the conduction band energy minimum. The free holes move to energy states near the valence band maximum through the similar process to electrons. After a certain amount of time, electrons in the conduction band minimum recombine either radiatively or non-radiatively with holes in the valence band. Luminescence is the spontaneous light emission from the material when the radiative electron and hole recombination process occurs. PL system measures the luminescence as a function of wavelength. The PL wavelength data can be converted to energy scale using Equation 3.4.

$$\lambda = \frac{hc}{E} = \frac{12398.45}{E} \qquad \text{Equation 3.4}$$

Here, the unit of λ is Å, while the unit of *E* is eV. The converted energies from PL peaks can be used to determine the bandgap energy of the material and to analyze the impurities and defect state within the bandgap. Therefore, room temperature PL (RTPL) is simple and useful method to calculate the compositions of direct-bandgap ternary semiconductors because energy of the bandedge PL peak varies with the alloy compositions. For quaternary semiconductors, however, PL and X-ray diffraction should be used simultaneously to determine the compositions of their constituent elements. The accurate determination of compositions is important to design optical device and to improve its performance. Also, material quality can be estimated from the intensity and full width at half maximum (FWHM) of PL peak. The higher quality semiconductor gives narrower FWHM and brighter intensity in the PL peak shape.

Low-temperature PL (LTPL) and temperature-dependent PL are other important PL-related measurements for the identification of impurity state, localized state, and band lineup [79]. Since the thermal excitation and the thermal energy broadening are suppressed sufficiently by decreasing the sample temperature, transition PL peaks tend to be more separable and sharper for LTPL.

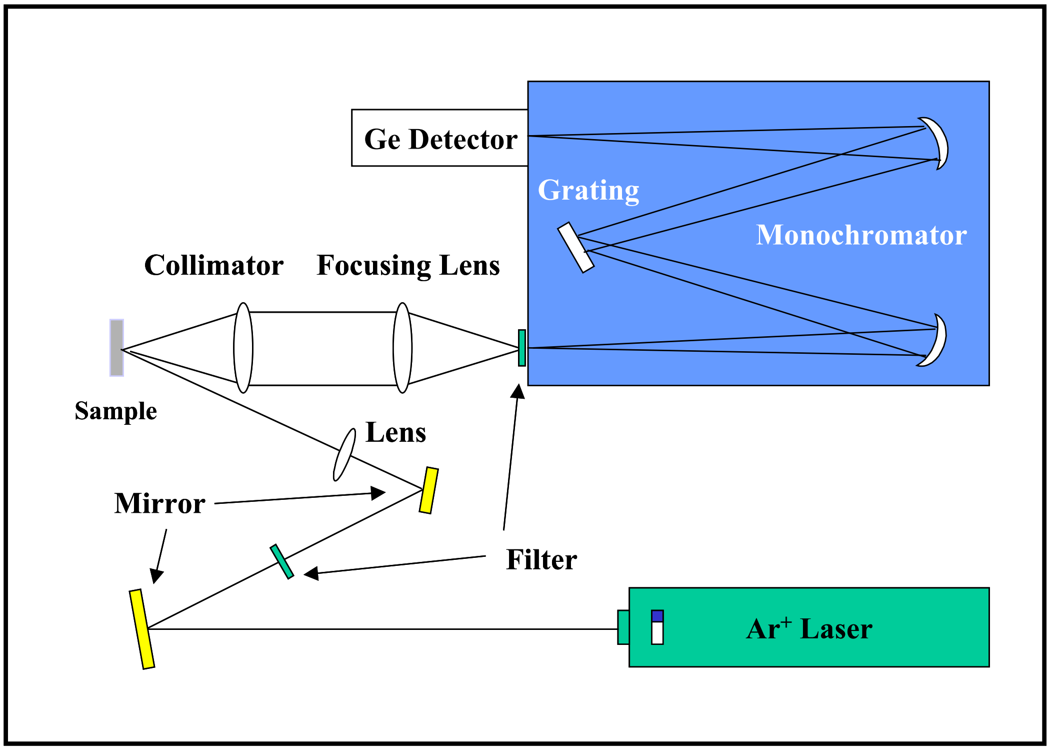

Figure 3.5 Schematic diagram of PL measurement system used in this study

In this study, PL spectroscopy is used to determine the transition wavelength and to characterize the optical quality of GaAsSb quantum-well heterostructures with various barrier materials. The schematic diagram of the experimental PL system is shown in Figure 3.5. The PL system consists of an excitation source, the beam routing optics, the luminescence collection optics, a spectrometer, and a detector. The sample is mounted on the sample mount or in the cryostat that can be filled with liquid nitrogen or liquid helium so that PL measurement can be performed at the temperatures of 4 K, 77 K, and 300 K.

The excitation light source for EHP generation is an Ar^+ laser (Coherent I-90, 20W maximum output power) operating at $\lambda = 488.1$ nm. The typical laser power that is used in this study is 100 mW ~ 300 mW. A beam of high-energy photons is reflected by mirrors and focused onto sample to create EHPs. Then spontaneous emission from sample is collimated and focused into spectrometer (SPEX 1 m focal length). The ruled grating inside the spectrometer distributes the multi-wavelength spontaneous light into monochromatic light to be detected and the intensity is recorded vs. wavelength. The gratings employed in the system have rulings of 1200 groove/mm with a blaze wavelength at 0.5 μm for GaAs and AlGaAs scan and 600 groove/mm with a blaze wavelength at 1.0 μm for long-wavelength InGaAs and GaAsSb PL spectra. Two types of detectors have used to gather distributed lights by monochromator. For visible spectral range detection (350 nm ~ 900 nm), a water-cooled photomultiplier tube (PMT) with a GaAs photocathode and for infrared region detection (900 nm ~ 1600 nm), a liquid-nitrogen-cooled Ge detector are used. The detected monochromatic light is converted into an electric signal and this signal is measured by digital multimeter and recorded by a computer-controlled system.

To achieve reliable comparison for sample to sample optical quality, the GaAs capping layer of sample was removed with H_2SO_4:H_2O_2:H_2O = 1:8:80 etchant and standard sample scanning was performed prior to the main sample scanning.

3.3 ATOMIC FORCE MICROSCOPY

Atomic Force Microscopy (AFM) is a scanning probe technique that makes it possible to image three-dimensional surface topography with nanometer-scale area and sub-nanometer depth resolution. Since Binnig, Quate, and Geber invented the AFM technique in 1986 [80], it has been improved greatly. Although the scanning tunneling microscope (STM) that is the ancestor of the AFM, and was invented by the same group [81], is considered a more fundamental technique for surface profiling, its applications are limited, because it can be performed only on electrically conductive samples. However, AFM can be used to scan the surfaces of various samples such as insulators, organic materials, ceramics, polymers, and semiconductors in different environments (atmosphere, liquid, and vacuum) because it uses mechanical forces to scan the surface.

Another special feature of AFM is that its resolution is directly related to the dimension of its probe tip, while imaging resolutions of other optical or electrical microscopes are limited by diffraction effects. When a very fine probe tip comes close to surface of a sample, it can detect variety of induced forces between the surface and the probe tip. By detecting these forces, AFM is possible to reconstruct the topography of the sample. The scanning methods of AFM can be categorized three types based on the tip spacing from sample surface. The inter-atomic force vs. tip-to-sample spacing is shown in Figure 3.6. When the probe tip, which is attached to the end of flexible cantilever, makes physical contact with the sample surface during a scan, it is called contact mode or repulsive mode AFM. As the tip moves on the sample surface, the contact force results in bending of cantilever in response to the sample topography. By tracing this deformation, AFM gives a surface image. One major demerit of contact-mode AFM is the possibility of contamination or damage of the sample surface by dirty tip or stiff cantilever.

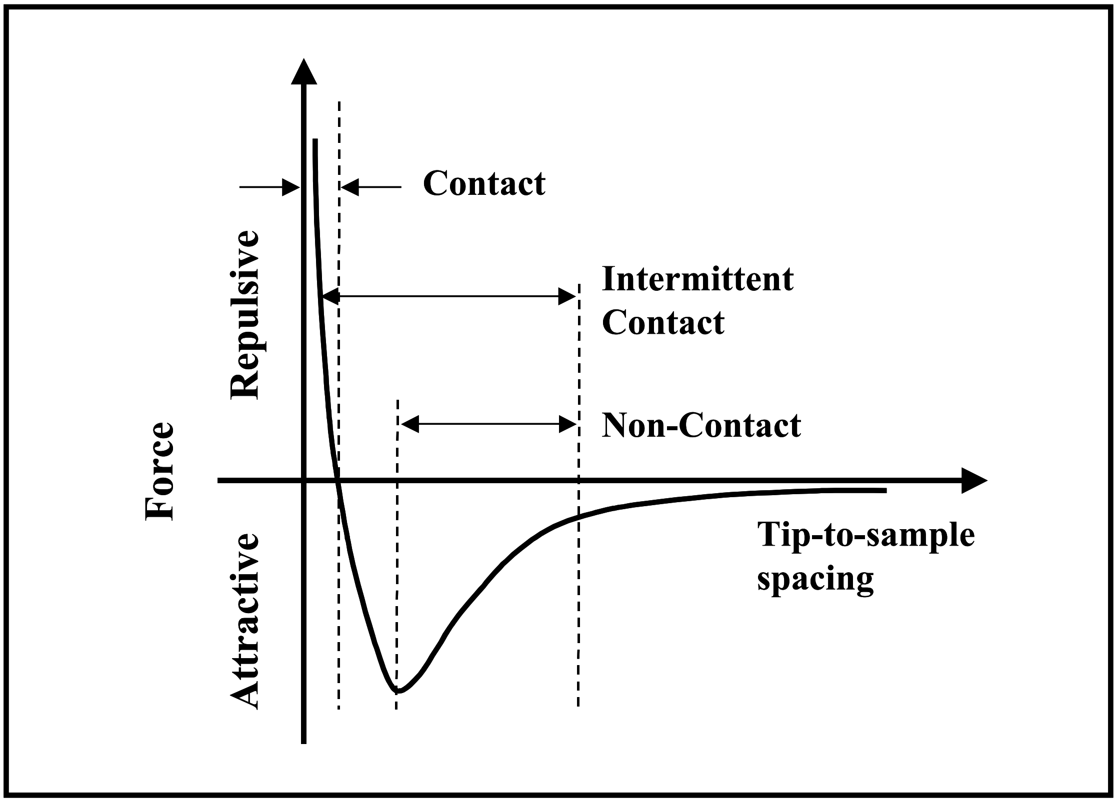

Figure 3.6 Interatomic force vs. tip-to-sample spacing curve in AFM

Non-contact AFM (NC-AFM) is one of the oscillating cantilever techniques and exploits the attractive force region in Figure 3.6. The typical spacing between the tip and sample surface is on the order of tens to hundreds of angstroms. NC-AFM is very desirable because it is a method for measuring the sample topography without contact, which can cause contamination or damage on sample surface. However it is more difficult to detect the force between the tip and sample than in contact mode, because the force is very small. Another drawback of NC-AFM is if there is water drop on the sample surface, the tip follows the contour and therefore, gives a false image.

The third type of AFM mode is intermittent-contact AFM (IC-AFM) and it is also known as tapping mode. IC-AFM is very similar to NC-AFM in terms of the oscillating cantilever technique, except that for IC-AFM, at the bottom of its oscillation, the oscillating tip touches or “taps” the sample when it is brought closer to the sample surface. According to the tip-to-sample spacing, the oscillation amplitude changes. By monitoring the changes, IC-AFM images the topography of the sample surface. Since IC-AFM eliminates sample damage from lateral forces (drag or friction) in contact AFM, and overcomes artificial image due to surface contaminations in NC-AFM, it has become an important non-destructive AFM technique.

The equipment used in this study is a Digital Instrument Dimension 3000$^{®}$. All scans were performed in tapping mode. The brief operational concept is illustrated in Figure 3.7.

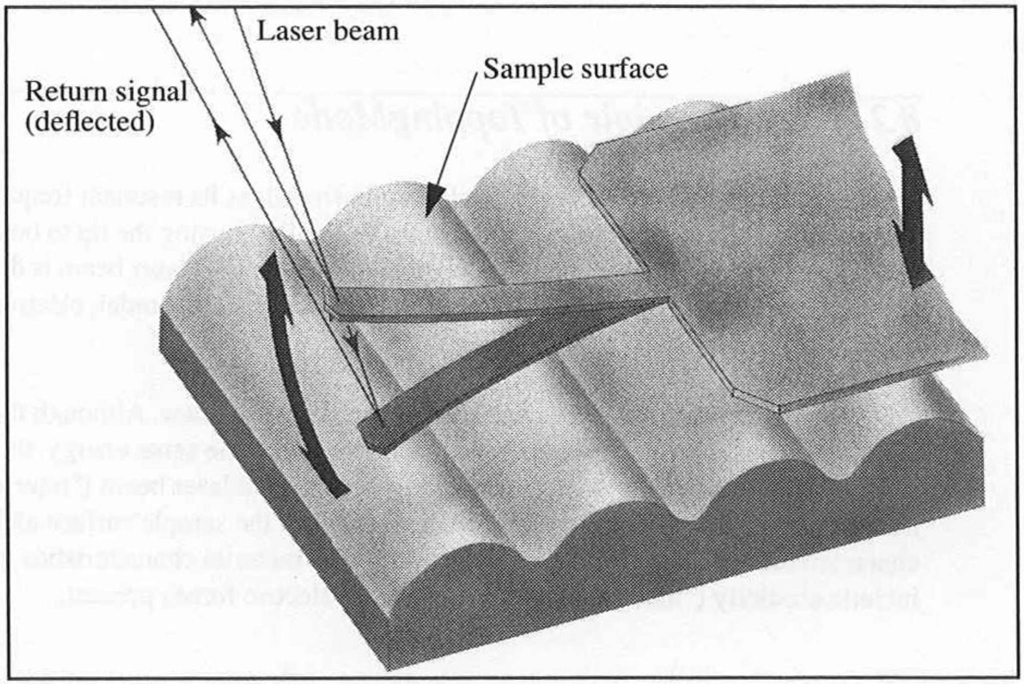

Figure 3.7 Illustration of tapping mode operation [82].

The surface topography changes the oscillation amplitude of the cantilever and it deflects laser beam that is reflected on the backside of the cantilever. A position-sensitive photo-detector (PSPD) measures the deflected beam signal as position and height information. Then the signal is converted to a surface image.

With AFM measurement, the surface smoothness, dislocation defect density, and epitaxial growth modes can be observed. An AFM image of a GaAs substrate surface is shown in Figure 3.8. The root-mean-square (RMS) surface roughness is only 0.221 nm for a 20 μm x 20 μm area scan.

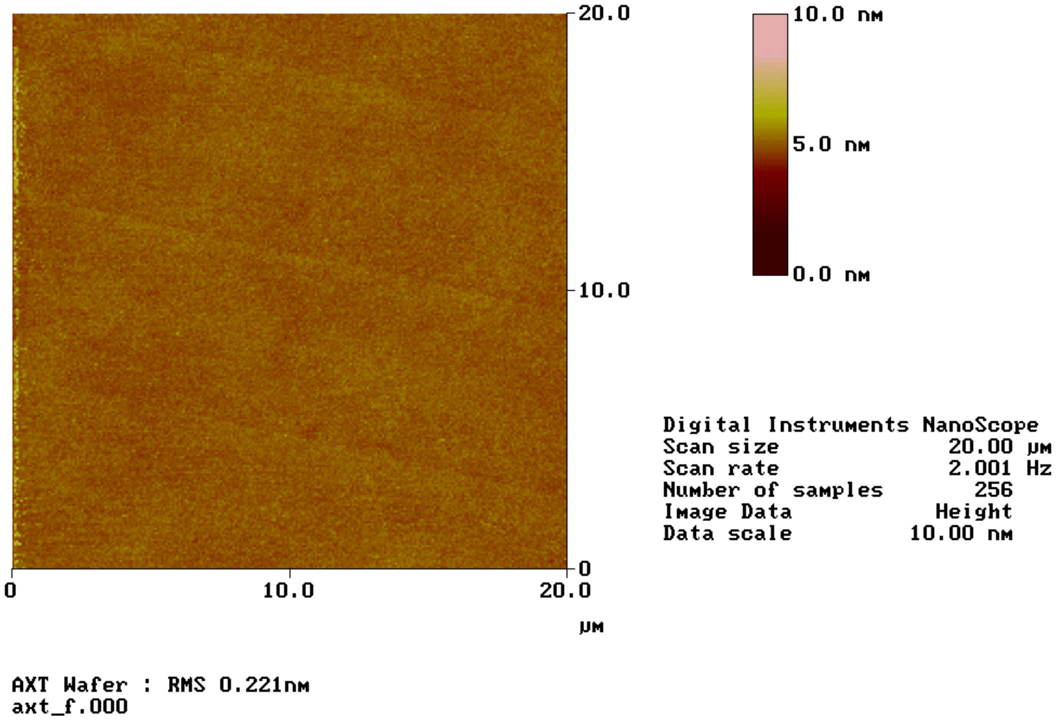

Figure 3.8 AFM image (20 µm x 20 µm) showing the smooth surface (RMS = 0.221 nm) of a GaAs substrate.

3.4 ELECTROCHEMICAL CAPACITANCE-VOLTAGE DOPING PROFILER

Since modern electrical and optical semiconductor devices require complicated and precisely controlled doping concentrations for each layer to meet the high performance device characteristics, information on doping or carrier concentration as a function of depth is important. There are several techniques to measure the doping concentration, but in most case, depth profiling of the doping concentration is limited. In this section, the measurement of the doping profile using the electrochemical capacitance-voltage techingue is discussed.

The capacitance-voltage (C-V) technique [83] is very useful to characterize semiconductor structures that exist in the form of a capacitance. This technique exploits the fact that the width of the reverse-biased space-charge region or depletion region of the semiconductor junction devices such as p-n diodes, Schottky barrier devices, and MOS devices depends on the applied voltage.

To derive the relation between capacitance and doing concentration [84], we first consider the Schottky barrier diode of Figure 3.9. A dc bias V is applied to p-type semiconductor with doping concentration N_a. The applied reverse bias produces a deletion region of width W. The capacitance is given by

$$C = -\frac{dQ_s}{dV} \qquad \text{Equation 3.5}$$

where Q_s is the charge in semiconductor. The negative sign implies that more negative ionized acceptor is generated as increasing the applied reverse bias. It is possible to extend the depletion region further into semiconductor by adding small amount of positive ac bias to the applied dc voltage. The depletion region increment is dW in the Figure. The increment of semiconductor charge dQ_s in the increased small volume can be written as following:

$$dQ_s = -qAN_a dW \qquad \text{Equation 3.6}$$

where A is the area of the semiconductor.

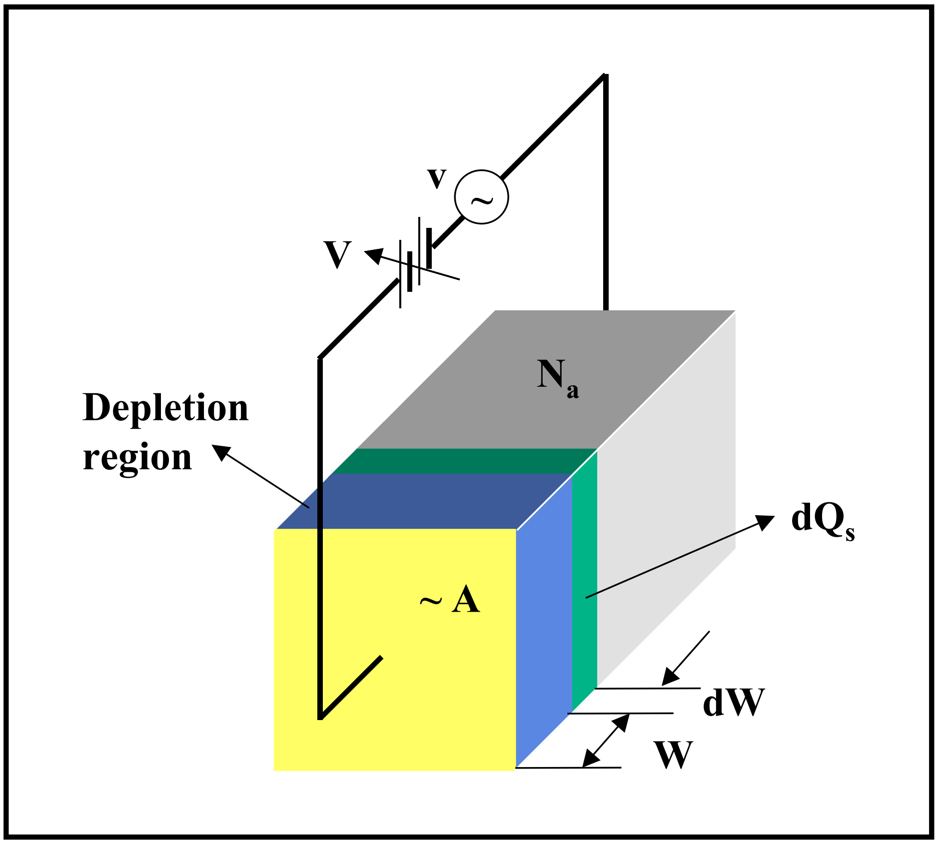

Figure 3.9 Illustration of a reverse-biased Schottky diode

The combination of Equation 3.5 and 3.6 gives

$$C = -\frac{dQ_s}{dV} = qAN_a \frac{dW}{dV} \qquad \text{Equation 3.7}$$

For the dielectric parallel plate capacitor, the capacitance is defined by

$$C = \frac{K_s \varepsilon_0 A}{W} \qquad \text{Equation 3.8}$$

where K_s and ε_0 are the relative permittivity of the semiconductor and free-space permittivity, respectively. By differentiating Equation 3.8 with respect to the voltage and substituting *dW/dV* into Equation 3.7, we have the expressions for N_a of Equation 3.9 and 3.10 with respect to *C*.

$$\boldsymbol{N_a = -\frac{C^3}{qK_s\varepsilon_0 A^2(dC/dV)}} \qquad \text{Equation 3.9}$$

or

$$\boldsymbol{N_a = \frac{2}{qK_s\varepsilon_0 A^2[d(1/C^2)/dV]}} \qquad \text{Equation 3.10}$$

The doping concentration N_a is obtained by measuring the capacitance and calculating the change of *C* or $1/C^2$ with respect to V from C-V plot. In those equations, since N_a is inversely proportional to A^2, the precise determination of semiconductor area is also important to determine an accurate doping concentration.

To more completely cetermine the doping profile in a semiconductor, the electrochemical-profiling technique is employed. The measurement concept of the electrochemical capacitance-voltage (ECV) is basically the same as the typical C-V technique except that ECV uses an electrolyte to make Schottky contact with the semiconductor rather than metal contact. However the prominent difference between C-V and ECV is that ECV has an etching ability through the use of a proper electrolyte, such that, in principle, an essentially unlimited depth profiling is realized. Repetition of C-V measurements combined with the etching of the electrolyte contact area and permit the measurement of the doping concentrations up to any depth. A drawback of ECV is its destructive nature. After the ECV measurement, there is a crater where the etching process occurred. For some special cases, ECV can also be used to determine the conduction-band offset [85].

In this study, a Bio-Rad PN4300 Semiconductor Profiler is used to measure the depth profile of doping concentration. A mixture of 0.2M disodium EDTA ($C_{10}H_{14}O_8N_2Na_2 \cdot 2H_2O$), 10% ethylenediamine ($C_2H_8N_2$), and H_2O is employed as the electrolyte to make a Schottky contact with the semiconductor and to etch the contact area. An ECV profile of an $Al_{0.45}GaAs$ film doped with Si is shown in Figure 3.10. The inset depicts the structure of measured sample.

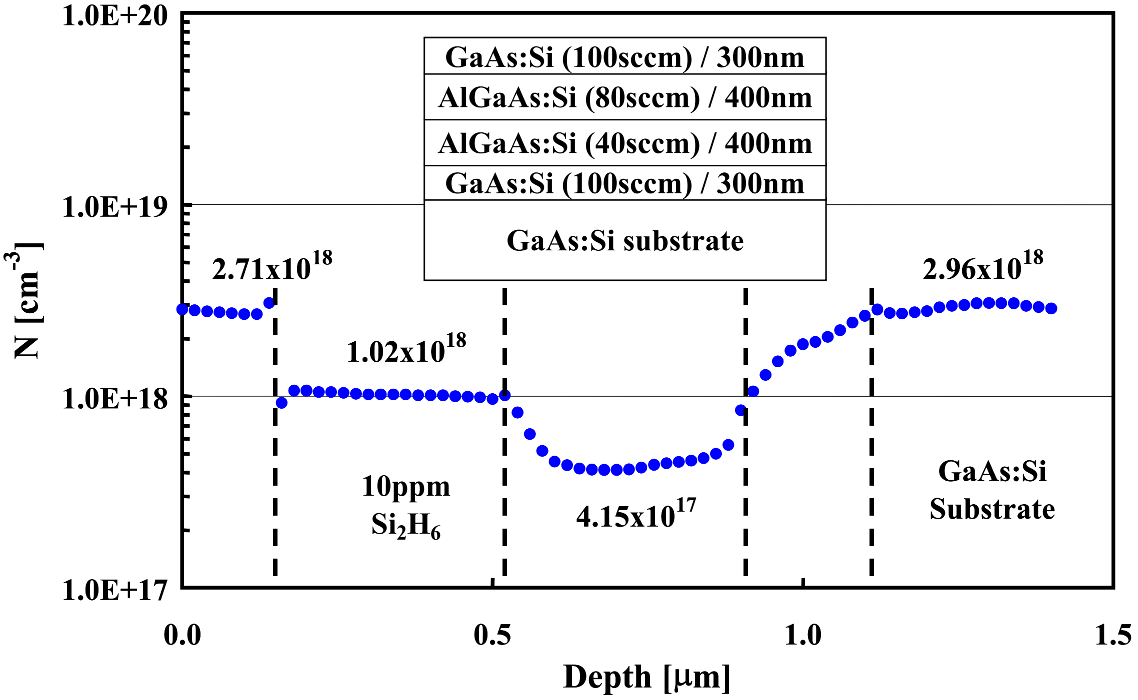

Figure 3.10 Doping profile of n-type Si doped $Al_{0.45}GaAs$ layer having different doping concentrations vs. depth.

3.5 CATHODOLUMINESCENCE

Cathodoluminescence (CL) is one of many characterization techniques that use luminescence phenomenon. CL is basically similar to photoluminescence (PL) however, while PL typically uses photons from a laser as the excitation source, CL results from the excitation of high-energy electron beam. When a high-energy electron beam hits a semiconductor sample, it interacts strongly with the material. The incident electrons are scattered either elastically or inelastically by interaction with the nucleus or the bound electrons of the material until they lose their energy, producing various energy radiations such as characteristic X-ray, secondary electrons, Auger electrons, back-scattered electrons, and cathodoluminescence of ultraviolet (UV), visible, and infrared (IR) from the material. The radiations typically produced by the bombardment of electrons on the sample are shown in Figure 3.11. Each radiation event can be used for various characterization techniques such as energy dispersive X-ray spectroscopy (EDS), scanning electron microscopy (SEM), Auger electron spectroscopy (AES), low- or high-energy electron diffraction (LEED or HEED), and CL.

The CL system is normally attached to an SEM system. Since the same electron gun, focusing and scanning system of SEM can be used in the CL system, CL can be done in the range of low (x20) to very high magnification (x100,000). There are two possible measuring methods in CL depending on the electron beam conditions. In scanning mode or known as raster mode, the electron beam is scanned over the interesting area and the generated light is collected by parabolic mirror and detected by a photodetector either directly (panchromatic) or as a function of wavelength (monochromatic) that is dispersed by a spectrometer. This scanning mode can give an area mapping of the CL image. Another CL mode is spot measurement that is spectral analysis of the luminescence with a focused electron beam at a certain point on the sample. By varying the temperature and the injection current of electron beam, CL can achieve microscopic resolution of the energy states in the sample.

In this study, low-temperature current-dependent CL is used to determine the band lineup of GaAsSb with various barrier materials.

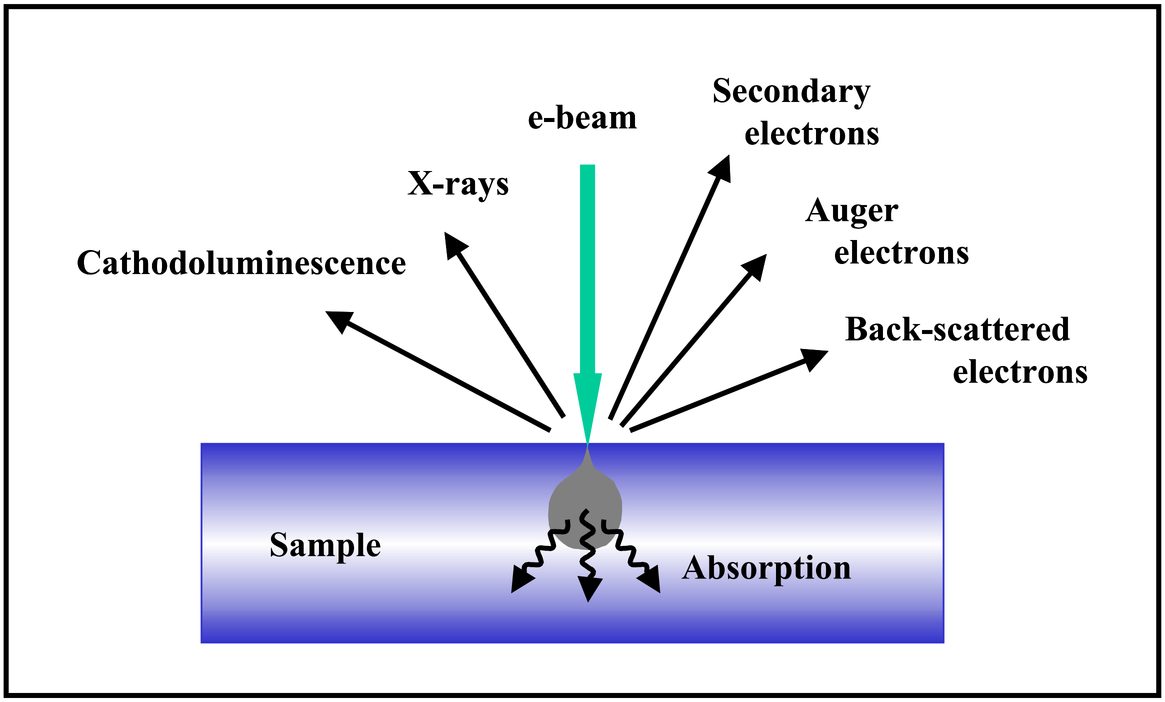

Figure 3.11 Schematic illustration of the radiations produced from electron beam interaction with a semiconductor

3.6 SECONDARY ION MASS SPECTROSCOPY

Secondary ion mass spectroscopy (SIMS) is one of the ion-beam characterization techniques and is very useful to determine the trace of the constituent elements, dopants, and impurities in solid materials, especially semiconductors and thin films. Among the ion beam techniques, SIMS is the most sensitive technique with detection limits for certain elements in the range of 10^{14} to 10^{15} cm^{-3}. Although this technique is destructive, it is widely used because of the detection ability of low concentration elements and achievement of information as a function of depth, called a depth profiling. The typical lateral resolution is less than 100 μm, but the depth resolution is 50 to 100 Å.

Bombardment of sample surface with a focused primary ion beam produces secondary particles that carry negative, neutral, and positive charges. When the secondary particles are escaping from the sample surface, they have kinetic energies that range from zero to several hundred eV. This bombardment also results in the sputtering or removing of surface material leaving a crater after the measurement. When the sputtering rate is extremely slow, the entire measurement of the secondary particle yield can be finished while consuming only a few tenths of an atomic monolayer. This very slow sputtering mode (typically ~1 Å per hour) is called *static* SIMS. On the contrary, continuous analysis as a function of depth with relatively high sputtering rate (~10 μm per hour) is known as *dynamic* SIMS, yielding an impurity concentration depth profile. The yield of secondary particles by primary ion bombardment is dependent on the sample material, the crystallographic orientation, and the nature, energy, and the incident angle of the primary ion beam. If the sputtering rates are fairly different for the constituent elements in a multicomponent material, selective or preferential sputtering can occur. Since SIMS detects only ionized particles, what is important is the yield of ionized ejected particles rather than the yield of total secondary particles. Basically the secondary ion yield is significantly small compared to the total secondary particle yield but can be influenced by the type of primary ion source. The primary ions used in SIMS include O_2^+, O^-, Cs^+, Ar^+, and Ga^+ with energy range of 1 to 30 keV. Electronegative primary ions like O_2^+ can enhance the yield of electropositive elements such as Zn, Mg, Ga and Al in AlGaAs. In a similar manner, electronegative elements that are generated by an electropositive primary ions like Cs^+. In this case, the secondary ion yields of Si, C, As, P, and Sb in AlGaAs, GaAsP, and GaAsSb can be increased. If a sample with both electropositive and electronegative elements is analyzed with SIMS, two separate SIMS runs are needed with O_2^+ and again with Cs^+. The ejected secondary ions are separated by their mass-to-charge ratio as they are going through the ion energy analyzer (electrostatic sector) and mass analyzer (magnetic sector). The electrostatic energy analyzer bends lower-energy ions more strongly than higher-energy ions. By changing the position and width of the energy slit, only interesting elements can be transferred to mass analyzer. As the ion beam passes through the magnetic field in the mass analyzer, the ionized particles are deflected by the formula in Equation 3.11.

$$\frac{\boldsymbol{m}}{\boldsymbol{q}} = \frac{\boldsymbol{B}^2}{2\boldsymbol{V}}\boldsymbol{r}^2 \qquad \text{Equation 3.11}$$

This equation shows the relationship between the mass-to-charge ratio (*m/q*), the magnetic field (*B*), the accelerating voltage (*V*), and the radius of ion curvature (*R*) in the magnetic field. The ions having different masses are deflected by different amounts. If the position of the slit for the ion-counting electron multiplier varies, different ion species will be detected selectively.

In SIMS analysis, the concentrations of elements present in the sample can be calculated from the signal intensities using the primary ion beam current, the sputter yield, the ionization efficiency, and the instrumental factors. However the accurate concentration is not easy to be determined, since some of these factors are not well defined. For example, one simple way to determine the alloy composition of a ternary or quaternary semiconductor from the SIMS intensity spectra is first making a set of standard samples whose compositions are determined accurately by another characterization technique like XRD and comparing the SIMS intensity ratios of each element with the standard samples. In usual case, it will be sufficient to check the compositional changes of alloy semiconductor layers at different depths with *dynamic* SIMS analysis.

3.7 TRANSMISSION ELECTRON MICROSCOPY

Transmission electron microscopy (TEM) is very useful characterization technique used to study metal, crystalline, polycrystalline, and organic materials with sub-atomic resolution. It is impossible for optical microscopy to achieve this extremely fine resolution, because classical Rayleigh criterion limits the best resolution of optical microscopy at roughly half of the wavelength of the light used. The typical resolution of the optical microscopy for green light (550 nm) in the middle of the visible spectrum is around 300 nm. On the other hand, the wavelength that is used in a TEM is significantly smaller, resulting in a great improvement in the resolution aspect. Based on the de Brogie's wave-particle duality idea, the wavelength of the accelerated electron beam can be calculated by considering relativistic effects:

$$\lambda = \frac{h}{\sqrt{2m_0eV\,(1+\frac{eV}{2m_0c^2})}} \qquad \text{Equation 3.12}$$

where h is Plank's constant (6.626x10^{-34} N·m·s), m_o is the electron rest mass (9.109x10^{-31} kg), e is electron charge (1.602x10^{-19} C), V is the acceleration voltage of the electron microscope, and c is the speed of light in vacuum (2.998x10^{8} m/s). When the acceleration voltage of 100 kV is used in TEM measurements, the wavelength of the electron beam is only 0.00386 nm. Although the theoretical resolution limit of this short wavelength is much smaller, typical resolution of TEM in practice is in the range of 0.25 ~ 0.3 nm because the real magnetic lenses that used in TEM are not perfect. But it is still small enough to observe the atomic scale structures of the measured sample and TEM can achieve the magnification of greater than x3,000,000 easily.

To perform TEM measurements, the sample must be extremely thin for the electron beam to pass through it and make an image. When the electron beam is passing through sample, it interacts with the material. Electron interacts strongly with the dense part of the material and weakly with the soft part of the material. This interaction difference from the different areas creates an electron intensity distribution on the imaging plane after transmission through the sample. The difference in intensity, also known as contrast can be recorded on film or on a screen and gives an image of the sample. If the direct beam from the sample is selected, the resultant image is called a bright-field (BF) image, and if any scattered electrons are selected for imaging, it is called a dark-field (DF) image. In addition to the imaging mode, by changing the slits in the TEM system, the diffraction pattern of crystal structure can be obtained too. Exploiting both image and diffraction pattern modes, TEM can determine the atomic-scale morphology features and the thickness of very thin layers as well as the presence of lattice defects such as dislocations, and stacking faults.

Further details of TEM can be found in many textbooks on TEM or electron microscopy [86]

3.8 SCANNING ELECTRON MICROSCOPY

Scanning Electron Microscopy (SEM) is a very convenient electron-beam characterization technique. When a fine electron beam is focused on a sample surface, low-energy secondary electrons are ejected from the sample by scattering between the incident electrons and the material. The secondary electrons are captured by a detector and processed to make an image of the sample. The typical electron gun is made of tungsten (W) and the acceleration voltage is round 10 ~ 30 keV. The measurement is performed under vacuum.

SEM has several benefits over both conventional optical microscopy and TEM. It is much better in resolution and magnification than those of the optical microscopy and much easier in sample preparation than TEM. However, used in this way, SEM characterization is a destructive technique, the same as TEM.

In this study, the SEM is mainly used to observe the cross-sectional view of the epitaxially grown layers. The cross-section of interest is delineated with proper etchant after cleaving the sample. The cross-sectional SEM image gives fairly accurate thickness information for each layer and it can be used for growth rate calibration, which is important and fundamental in MOCVD growth to make precisely controlled device structures.

In Figure 3.12, a cross-sectional SEM image of AlGaAs/GaAs is shown. The layers are selectively etched with HF:H_2O_2:H_2O = 1:1:10 echant for delineation.

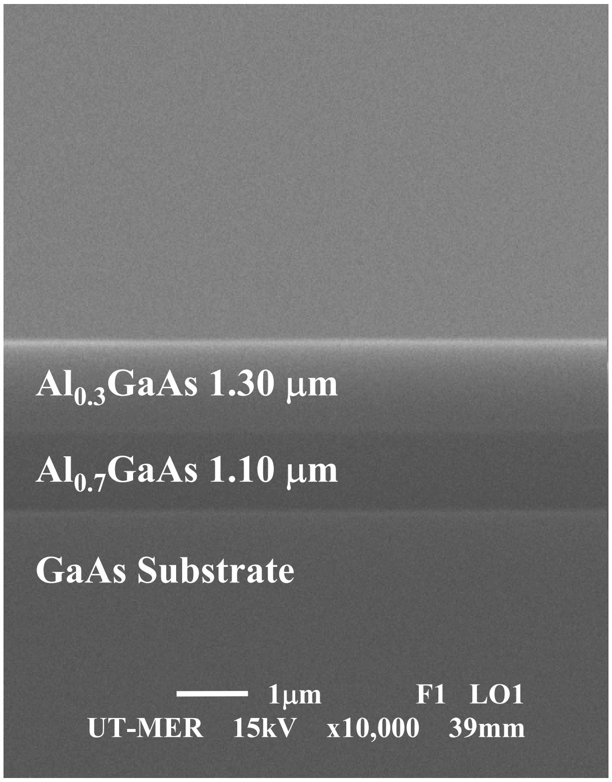

Figure 3.12 Cross-sectional SEM image of AlGaAs/GaAs structure.

Chapter 4: Material growth and optimization of growth conditions

This chapter discusses the MOCVD growth and analysis of GaAs, AlGaAs, and GaAsSb QW structures to optimize the growth conditions. When making a laser structure, n- and p-type doping of the semiconductor materials are essential. The doping issue is covered in this chapter too. GaAsSb is a very subtle material from the growth point of view. As described in Chapter 1, the epitaxial growth of GaAsSb has several challenges. To optimize the growth conditions, a great number of GaAsSb QW structures have been grown with varying growth temperature, V/III ratio, and QW thickness. Also novel barrier materials are employed to achieve strain-compensation and Type-I band lineup for improving optical and electrical properties.

4.1 ALGAAS GROWTH AND CHARATERIZTION

In GaAs based optical devices, AlGaAs is very important material for wave-guiding and cladding layers. Since AlGaAs is virtually lattice matched to a GaAs substrate in the whole Al alloy composition range, it is possible to grow even AlAs on GaAs without dislocation formation. Therefore, significantly thick AlAs/GaAs pairs can be used as VCSEL DBR mirrors. The AlGaAs material quality is critical to obtain good device performance. The oxygen (O) is likely to be incorporated into AlGaAs and is considered to be a major contaminant in AlGaAs grown by MOCVD. When O is incorporated into AlGaAs, it causes dopant compensation, low luminescence efficiency, and degradation of the surface morphology [87]. To overcome the problems due to the O incorporation into AlGaAs, high-purity sources and high growth temperatures are required [88]. The AsH_3 source was considered the O source in early development of MOCVD. However hydride purification techniques and the inner surface treatment of its container have been improved, such that AsH_3 having a purity of 99.99994% is commercially available and this ultra-high-purity hydride source is employed in this study. Therefore we can eliminate the hydride from being the source of O. Other possible O sources are MO precursors, especially TMAl. To evaluate our TMAl sources, AlAs/AlGaAs multiple layers are grown with two different TMAl sources.

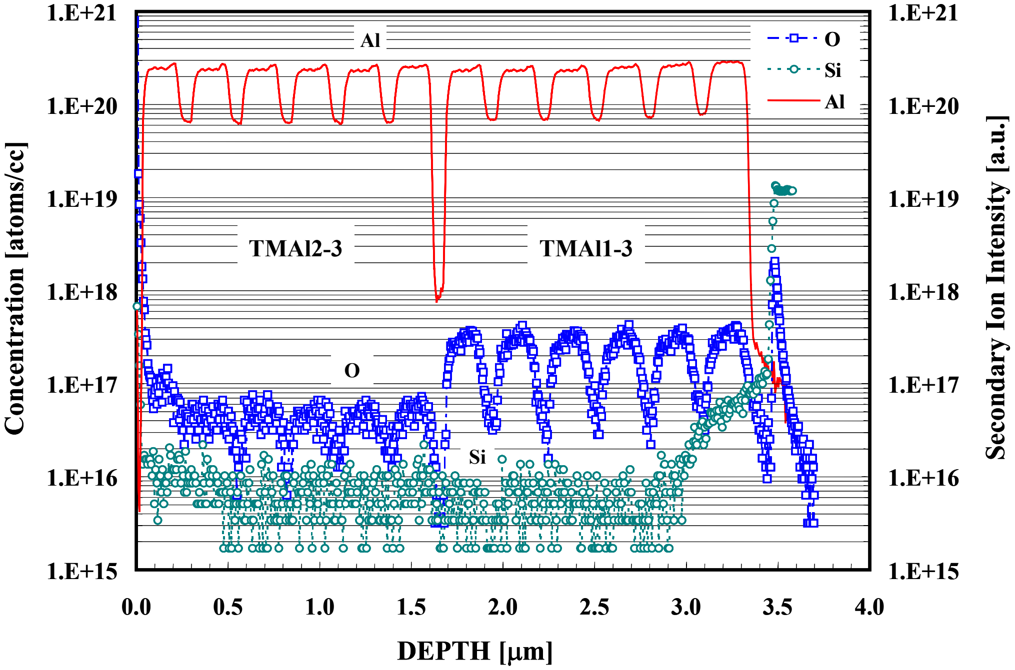

Figure 4.1 SIMS analysis of AlAs/AlGaAs multiple layers grown with two different TMAl sources (— Al, ○ Si, and □ O).

In the SIMS analysis shown in Figure 4.1, it has been found that the layers grown with TMAl1-3 have much higher O impurity level (□) than the layers grown with TMAl2-3. Based on this result, only the lower O level TMAl source has been used as the Al source for the growth of device structures.

Before discussing the next issue, it is to describe the substrates used here. All samples that are discussed in this study are grown on 2" GaAs substrates. They are manufactured by AXT using the VGF (vertical gradient freeze) bulk crystal growth method. After wafers are sliced from the GaAs ingot, the substrate surface is polished and cleaned to ensure an "epi-ready" grade (hence a separate substrate surface treatment is not necessary prior to main growth). The GaAs substrates employed in the growth are Si doped n-type ($\sim 10^{18}$ cm^{-3}) having an orientation of (100) ± 0.5º. The etch pit density (EPD) is less than 500 cm^{-2}. The VGF substrate quality is considered superior to that of HB (horizontal Bridgeman) grown GaAs wafers.

To design a laser structure, the properties of the lower and upper cladding layers, which are necessary to confine carriers and light, must be determined. In Figure 4.2, the relation between the Al vapor compositions that are calculated from the TMAl and TEGa molar flow rates and the solid alloy compositions from XRD measurement is shown. Since modern laser diodes usually utilize a graded-index separate-confinement heterostructure (GRINSCH) active region and a p-type AlGaAs/GaAs DBR also uses graded composition layers to reduce the resistance, we need to know the growth rates and compositional information over a wide composition range of AlGaAs in order to realize the GRINSCH and the graded-composition DBR. Using Figure 4.2, we can easily calculate the solid Al alloy composition according to the input Al molar flow rates. The lower circles are calculated by using the Philips X'pert software and the upper squares are calculated from the angle separation between AlAs and GaAs. There is some discrepancy between both calculations, especially in the high Al composition region. This can be attributed to the inaccurate simulation parameters in the software or the strain effect of AlGaAs.

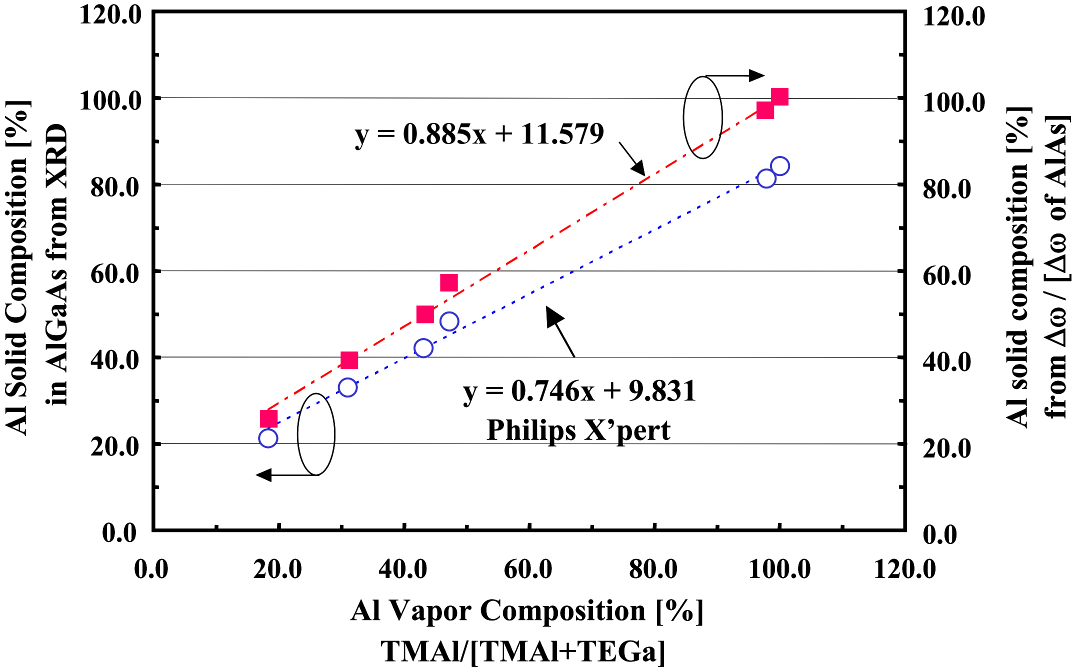

Figure 4.2 The relation between Al vapor composition and solid composition of AlGaAs grown at 700 ºC.

The growth rate dependence of the total source molar flows (TMAl + TEGa) is also examined in this work. To confirm the AlGaAs layer thickness, a fairly thick (0.4 ~ 0.5 μm) layer is grown and the thickness of each AlGaAs layer is measured by using cross-sectional SEM analysis with 10,000 magnification. The best linear fit is obtained if the TMAl incorporation is assumed to be 2.5 x TMAl molar flow rate (Figure 4.3). With these two results (Figure 4.2 and Figure 4.3), it is possible to predict any Al composition in the AlGaAs and growth rate of the layer.

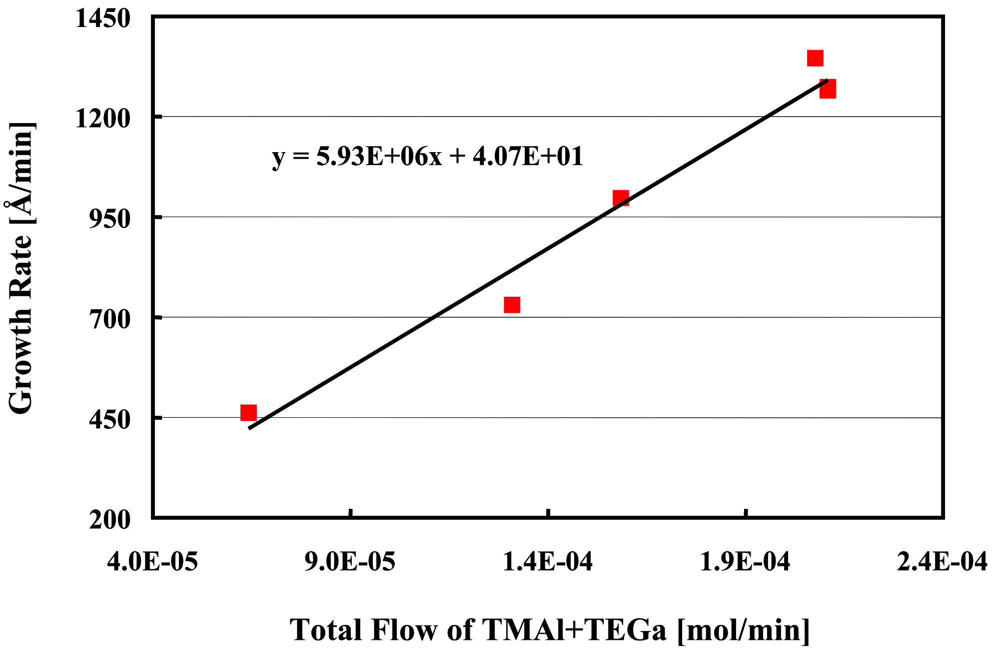

Figure 4.3 The relation between growth rate and total molar flow rate of (TMAl + TEGa). The AlGaAs layers are grown at 700 ºC.

These linear relations of growth rate and Al composition in AlGaAs are applied to all the cladding layers in further growth of GaAsSb QW test structures and laser device structures.

4.2 P-TYPE AND N-TYPE DOPING

4.1.1 p-type doping

In order to fabricate p-n junction devices, p-type doing in semiconductor is necessary. p-type doping occurs when acceptor impurities are doped into a host semiconductor, and some of the valence band electrons are trapped by the acceptors and leave free holes in the valence band of the material. It is commonly found that p-type doping is more difficult to achieve than is n-type doping. Since p-type dopants such as Zn and Mg usually have high diffusion coefficients, this can cause an undesirable graded junction or a junction shift into the n-type material during re-growth or thermal processing [89]. For example, a laser structure that has a junction shift due to dopant diffusion typically has a large turn on voltage, a large threshold current, or in worst case, it does not lase. In addition, because most device processes are performed on p-type layers, e.g. the creating of a current restriction channel and corresponding area contact formation, etc., a high doping concentration is required. The prerequisites for the good p-type dopant are a low diffusion coefficient, and a high solubility to achieve high p concentration and thermally robust material.

For AlGaAs/GaAs optical and electrical devices grown by MOCVD, Mg and Zn are commonly used for acceptor impurities, while Be is use for heavy p-type doing in MBE-grown materials. All these are Group II elements and they substitute for Group III elements in the III-V semiconductor crystal lattice to generate acceptor states and free holes at 300 K. However the diffusion coefficients of Mg (0.68~ 1.4 x 10^{-13} cm^2/s at 900 ºC) [90,91], and Zn (2.2 x 10^{-14} cm2/s ~ 1.0 x 10^{-12} cm^2/s at 900 ºC) [91,92] are very high. For the purpose of finding a better p-type dopant, C has been studied and employed as a p-type dopant in optical and electrical devices such as AlGaAs lasers [93], HBTs [94] and GaAsSb/InP HBTs [95]. C as a p-type dopant has several benefits over Mg and Zn. It has a lower diffusion coefficient (6.0 x 10^{-15} cm^2/s at 900 ºC) [96], a higher solubility [97] and a smaller memory effect. Also it is relatively easy to get a concentration of over 10^{20} cm^{-3} free holes for use in the Ohmic contact layer or the base in HBT.

There are two possible methods for C doping. One is the use of the methyl radicals in the MO sources of TMGa and trimethylarsine (TMAs) [98,99]. In this method, C incorporation rate is dependent on the pyrolysis of the sources in the gas phase or on the substrate surface. The other method is using various C precursors as C sources. The halomethanes of carbontetrachloride (CCl_4) [100], carbontetrabromide (CBr_4) [101], and carbontrichloro-bromide (CCl_3Br) [102] have been investigated. A well-known problem encountered in the use of CCl_4 is the etching effect [103] during growth, giving an unstable growth rate on doped materials. The problems with the use of CBr_4 are the reduced growth rate of C doped materials due to the preferential gas phase bonding effect between Ga and Br, and the low vapor pressure because the source is a solid at room temperature. However, CCl_3Br is a liquid source with stable vapor pressure and it has been reported that it does not have any etching effect. Although this source is very promising C dopant, it is not common yet. Since C is an amphoteric dopant, in order to acts like an acceptor, it should substitute on a Group V element site. Therefore a low V/III ratio gives a high C incorporation into the semiconductor materials. The growth temperature effects on C incorporation are somewhat controversial.

In this study, a CBr_4 solid-source precursor has been used as the p-type C doping source. First of all, we have not observed any growth rate reduction even for the growth of highly C doped GaAs and AlGaAs layers. This may be attributed to the different flow dynamics of our MOCVD system. Figure 4.4 shows a cross-sectional SEM image of C doped and undoped $Al_{0.8}GaAs$ and GaAs layers grown at 650 ºC. The growth rate of the undoped AlGaAs layer is same as those of the $3.0x10^{18}$ cm^{-3}, and the $6.0x10^{18}$ cm^{-3} C doped AlGaAs layers. The growth rate is 1290 Å/min for all AlGaAs layers. This very high growth rate (the typical growth rate of AlGaAs is around 300 ~ 500 Å/min) is employed here for preventing the degradation of the GaAsSb active QW layer during the long growth time for the thick AlGaAs upper cladding layer at a relatively high temperature. This will be discussed in a later section. Constant growth rates are also observed in C doped and undoped GaAs layers. From these results, we have found that CBr4 can be a reliable C source without any etching effect during the layer growth.

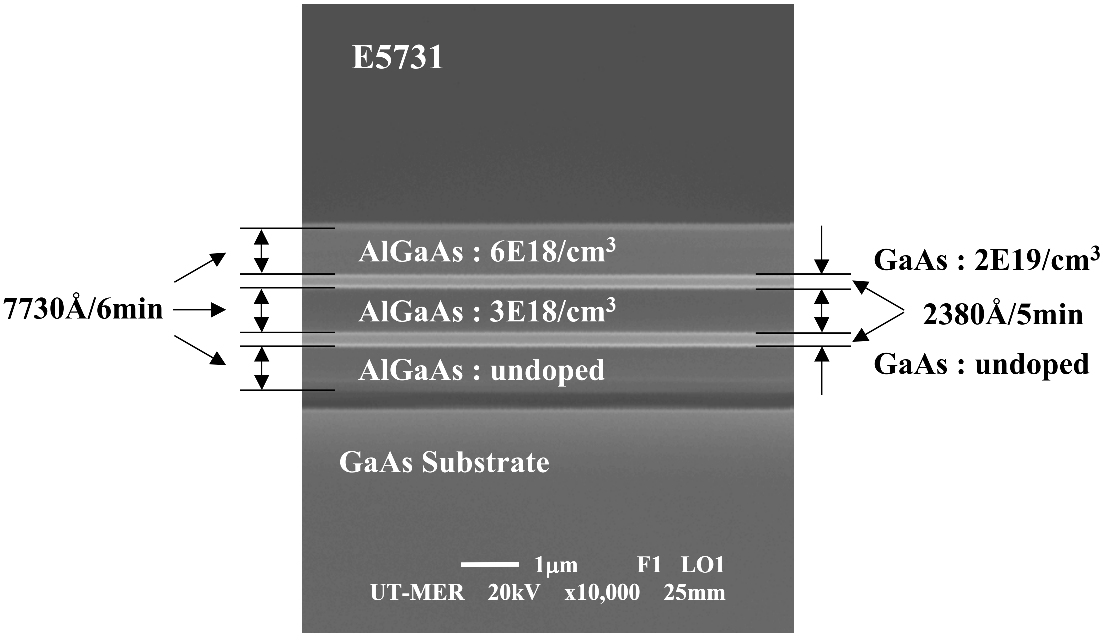

Figure 4.4 Cross-sectional SEM image of C doped and undoped AlGaAs and GaAs layers (The growth rate of the heavily doped layers are same as used for the undoped layers.)

The doping concentrations vs. depth of p-type C doped $Al_{0.45}GaAs$ layers grown at 650 ºC are measured by ECV method. The typical doping profile is shown in Figure 4.5. The structure and CBr_4 molar flow rate are given in the inset.

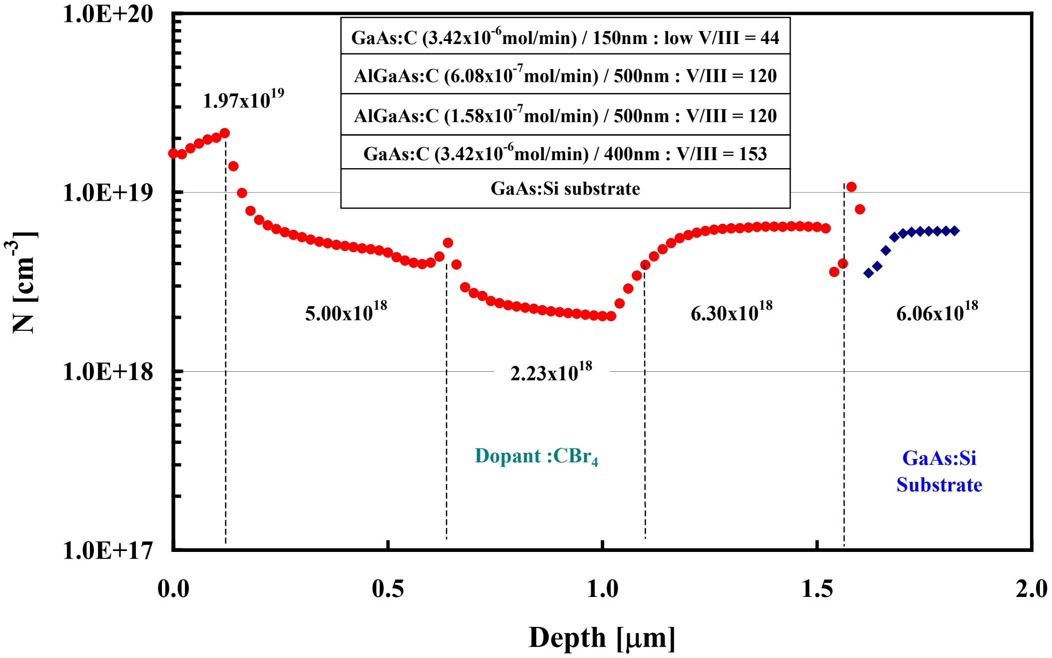

Figure 4.5 ECV doping profile of C doped $Al_{0.45}GaAs$ and GaAs layers grown on an n-type GaAs substrate.

The GaAs cap layer employed in the laser structure is heavily doped with C. The p-doping concentration reaches ~2.0x10^{19} cm^{-3}, and it is realized by growing this layer with a fairly low V/III ratio of 44. The AlGaAs layers also have high p-doping concentrations. As a comparison, the doping profile of Zn doped $Al_{0.45}GaAs$ and GaAs layers grown at 650 ºC are shown in Figure 4.6.

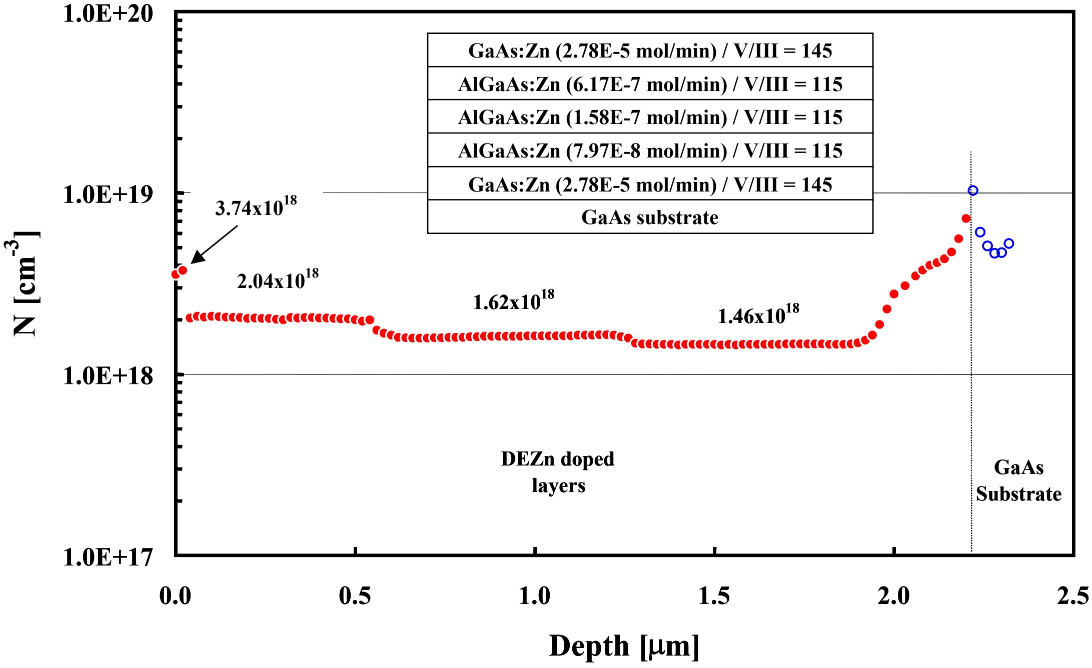

Figure 4.6 ECV doping profile of Zn doped $Al_{0.45}GaAs$ and GaAs layers grown on an n-type GaAs substrate.

The maximum p-doping concentrations for Zn doped GaAs and AlGaAs are 3.74 x 10^{18} cm^{-3} and 2.04 x 10^{18} cm^{-3}, respectively. The inset gives the structure and the DEZn molar flow rates for each layer. To obtain a lower contact resistance for laser applications, the CBr_4 source has been used for the p-type dopant rather than DEZn in this study.

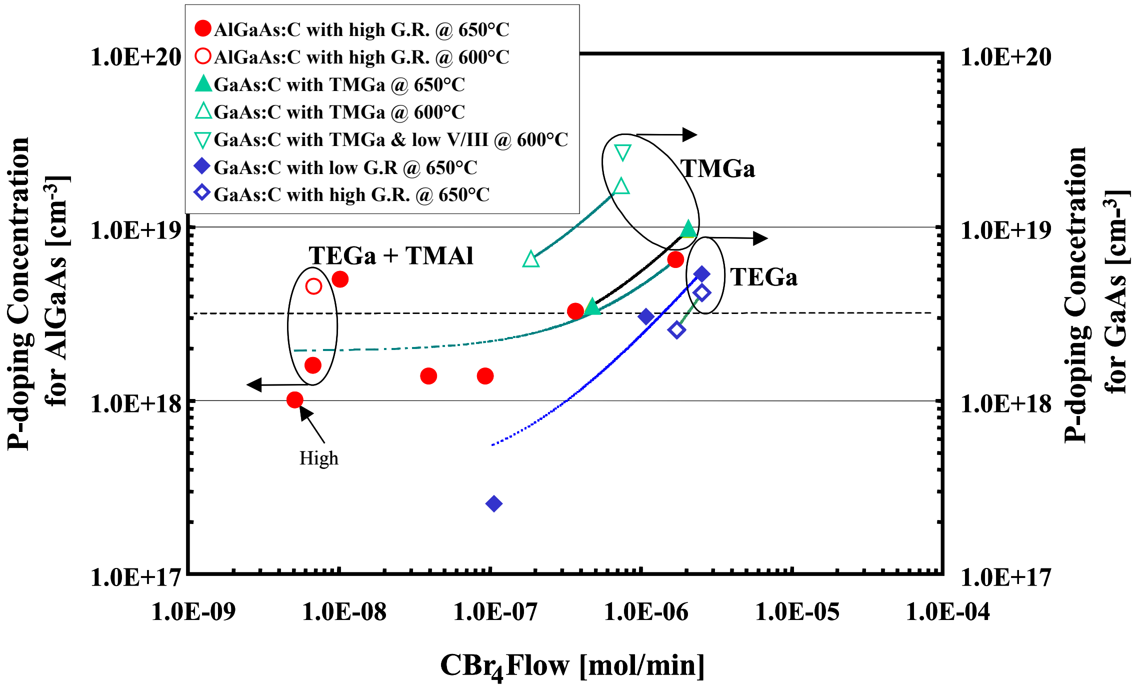

Figure 4.7 p-doping concentration in C doped GaAs and AlGaAs according to CBr_4 flow and growth rate.

In Figure 4.7, the p-doping concentrations in GaAs and $Al_{0.45}GaAs$ as a function of CBr_4 flows and the growth rate of each material are summarized. Especially in the VCSEL application, a high doping concentration in the p-GaAs capping or contact layer becomes very important. A heavily doped capping layer reduces the contact resistance even in the small contact area, resulting in a more reliable device. The carbon doping concentration in the GaAs layer is increased for a high growth rate, a low T_g, and a low V/III ratio. For GaAs growth using TMGa, a low V/III ratio (~50), a low T_g, and a high growth rate (515 Å/min), a p-doping concentration of $2.0x10^{19}$ cm^{-3} was obtained. For the growth of the p-type AlGaAs cladding layers, high enough doping concentrations are achieved from a wide range of CBr_4 flow rates.

4.1.2 n-type doping

For n-type dopants of III-V semiconductor materials, Group VI elements (S, and Se) and amphoteric Group IV elements (Si, and Sn) are commonly used. In this study, 10 ppm disilane (Si_2H_6) balanced in high-purity hydrogen is used as an Si dopant source. The Group IV Si atom usually substitutes on a Group III element site in MOVCD growth and gives an extra electron into host semiconductors. For laser structure growth with MOCVD, a Si doped GaAs buffer layer and a n-type Si-doped AlGaAs cladding layer are required. Since when using a disilane source, the Si incorporation rate into a semiconductor increases as the growth temperature increases [104], and AlGaAs has better material quality when it is grown at higher temperature, all Si doped AlGaAs layers are grown at high temperature of 700 ~ 740 ºC.

The relation between the Si_2H_6 molar flow and the doping concentration in AlGaAs layers, grown at 700 ºC, is shown in Figure 4.8. It has linear relationship for a wide range of Si_2H_6 molar flow rates, such that we can predict the n-type doping concentration from 3.0×10^{17} to 2.0×10^{18} cm^{-3} doping ranges in our experiment. The diffusion coefficient of Si (~10^{-18} cm^2/s at 575 ºC and 4.0×10^{-15} cm^2/s at 850 ºC in GaAs and AlGaAs) in a semiconductor is very small compared to typical p-type dopants, resulting in a relative ease to achieve an abrupt junction. Furthermore, since n-type GaAs substrates have better quality than p-type substrates, almost all structures are grown on n-type GaAs substrates. This means that the current blocking and current channel formations are performed in the p-type material side in most laser diodes. Therefore, the n-type cladding layer characteristics are more forgiveing than that of the p-type layer in the real device fabrication point of view.

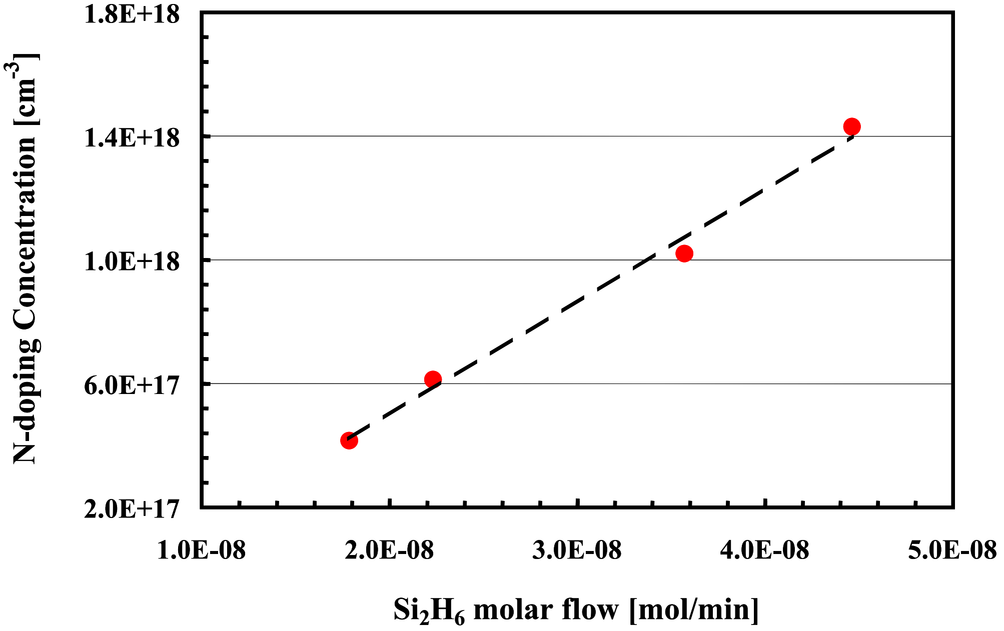

Figure 4.8 n-doping concentration in Si doped $Al_{0.45}GaAs$ as a function of Si_2H_6 molar flow rate.

4.3 GAASSB GROWTH AND CHARACTERIZATION

The antimony (Sb) based compounds and their alloys have been attracting great interests because these material systems represent the smallest bandgap among the III-V semiconductors. The bandgap can be as small as 0.15 eV at 300 K for InAsSb alloys [105]. These compound semiconductor systems are suitable for the 1.3 ~ 1.55 μm silica-based optical fiber communications, the 3 ~ 5 μm range of interest for chemical sensors, and even into the 8 ~ 12 μm night vision and infrared imaging applications.

GaAsSb has been researched for optical communication application as a novel light emitting active material and we also studied this material for the same purpose. However a major difference in the growth of GaAsSb is related to the reduced volatility of Sb compared to As and P. This means that the use of the typical high V/III ratio to grow the material results in solid Sb formation on the grown layer. Therefore the growth conditions for GaAsSb are somewhat different from the conventional larger bandgap P- and As-based materials. Since the active material quality is essential to the development of high performance laser devices, first we have focused on the growth of high-quality GaAsSb layers and second on the optimization of the growth conditions. In addition, to improve the optical quality, novel barrier materials are employed.

4.3.1 Growth of GaAsSb layers

The epitaxial layers to be discussed here have been grown by low-pressure MOCVD on (100) on-axis Si-doped n-type semi-conducting GaAs substrates. The growth was performed in ambient of H_2 that is purified through a Pd-cell operated at 400ºC, employing the primary precursors TEGa, TMAl, and TMIn as Group III alkyl sources, and AsH_3, PH_3 and TMSb as Group V hydride and alkyl sources. The growth pressure was fixed at 76 Torr. T_g ranged from 520 to 590 ºC for GaAsSb and barriers to optimize material quality and the other layers were grown at 650 ºC and 700 ~ 740 ºC.

In order to find the basic growth conditions, 0.2 and 1.0 µm thick GaAsSb layers were grown at 540 ºC with V/III ratio of 10.66 and 13.9 and an Sb vapor composition of 6.1% and 40%, respectively.

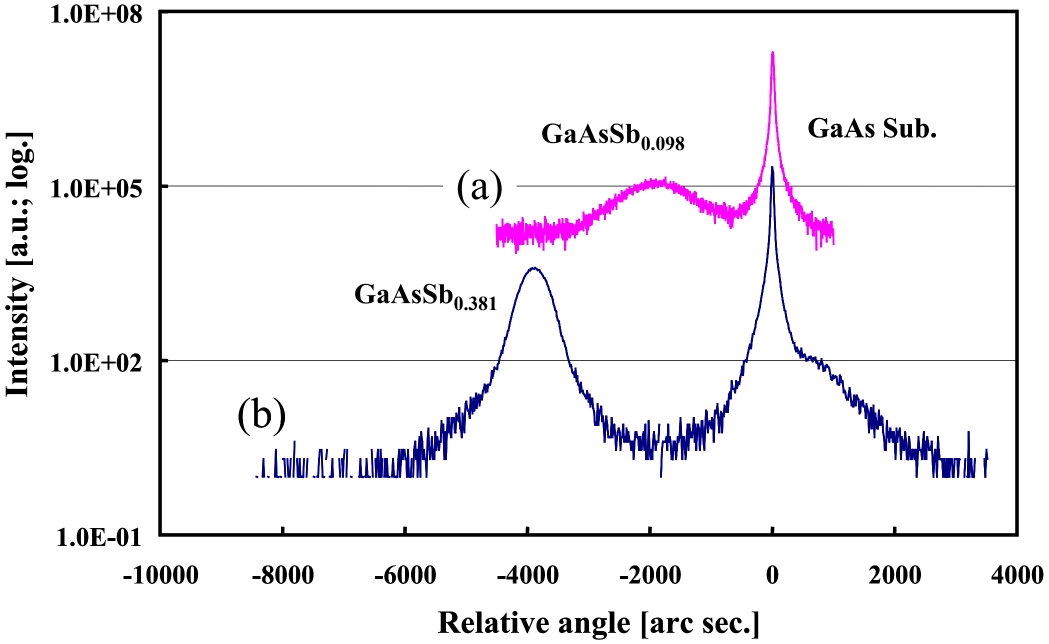

Figure 4.9 XRD of 0.2 µm and 1.0 µm thick GaAsSb layers grown on GaAs substrate.

The XRD scans of two of these layers are shown in Figure 4.9. The Sb solid compositions are 9.8% (Figure 4.a (a)) and 38.1% (Figure 4.a (b)). The Sb incorporation rate decreases even when the Sb vapor composition is high. The Sb incorporation effect into GaAsSb will be discussed in the next section. The complete strain relaxation of the GaAsSb layer is confirmed by RSM measurements (Figure 3.2). The growth rate determined by SEM for thick layers was 166.7Å/min. Although the possibility of GaAsSb growth by MOCVD is verified from these results, for real applications, the optical properties of the GaAsSb layer is important. Since the GaAsSb layers grown on GaAs have as large as mismatch, it is necessary to grow very thin layers within the critical thickness. Based on the information of the alloy composition and the growth rate, AlGaAs/GaAs/GaAsSb SQW- or MQW-SCH structures were grown to check the material quality. To grow all layers in one growth run, a three-step growth technique was used starting with a high-temperature GaAs buffer (200 nm thick) and AlGaAs lower cladding layer (300 nm thick) grown at 700ºC, followed by the growth of the GaAsSb QWs (75 ~ 116 Å thick) and barriers (30 nm thick) at low-temperature (520 ~ 590ºC), and finally, the upper AlGaAs cladding layer (300 nm thick) and the GaAs capping layer (500 Å) are grown at 650ºC which is lower than the growth temperature of the lower cladding layer to minimize the thermal degradation of the GaAsSb layer. During the T_g change step, growth was interrupted for maximum of five minutes in an AsH_3 ambient. No degradation has been observed at the interface when using this procedure.

First, the GaAs barrier and GaAsSb QW-SCH structure was investigated as a reference point for the other barrier structures. The effect of the growth parameters will be discussed in the next section. A typical XRD scan is shown in Figure 3.4. The cross-sectional image and the surface quality of the structure are characterized with TEM and AFM (shown in Figure 4.b and Figure 4.c, respectively). The TEM cross-section image of Figure 4.10 shows that the interfaces are very smooth and the fully strained GaAsSb QWs were grown without any dislocations. Figure 4.11 depicts the step-flow grow of the GaAsSb DQW-SCH surface. 2D or 3D growths were not observed.

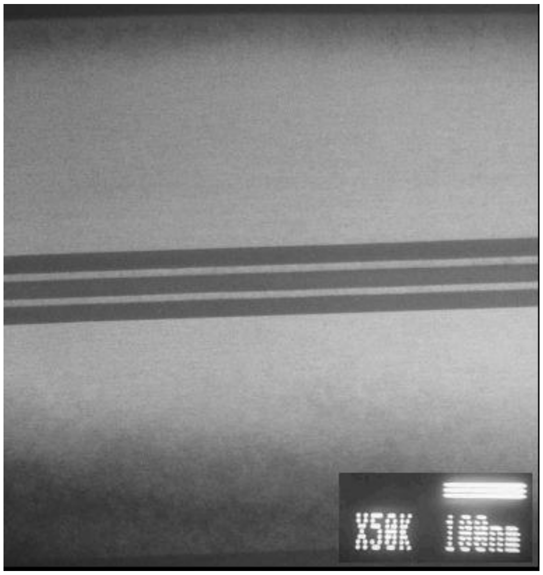

Figure 4.10 TEM cross-section view of a DQW-SCH structure.

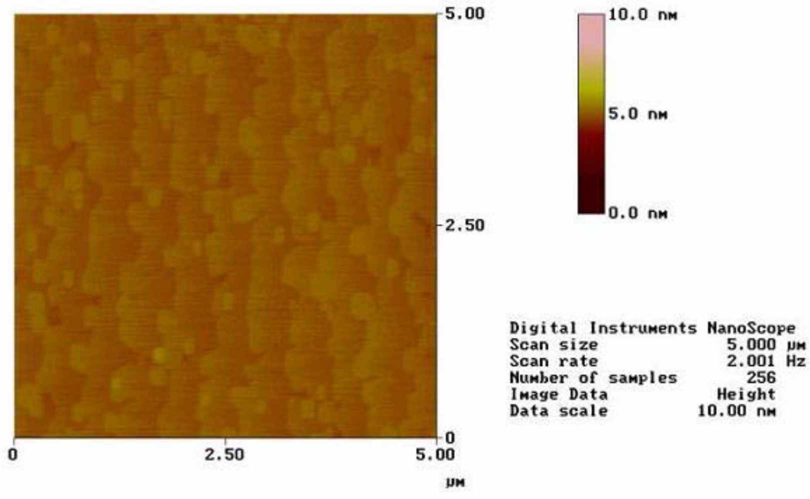

```
Digital Instruments NanoScope
Scan size              5.000 µm
Scan rate              2.001 Hz
Number of samples        256
Image Data             Height
Data scale           10.00 nm
```

Figure 4.11 AFM surface image of a GaAsSb DQW-SCH structure.

With these fundamental growth results, large sets of GaAsSb QW structures were grown with various V/III ratios (10 ~ 15), and T_g (520 ~ 590ºC). As discussed in Section 1.4 of Chapter 1, materials that have a wide miscibility gap are hard to grow without phase separation using equilibrium growth techniques. As shown in Figure 4.12, only with a non-equilibrium growth technique (e.g., MOCVD), could GaAsSb alloys be grown metastably inside the miscibility gap. Data points outside the curve were grown by LPE. We have been able to grow GaAsSb layers successfully inside the miscibility gap with MOCVD at various T_g values.

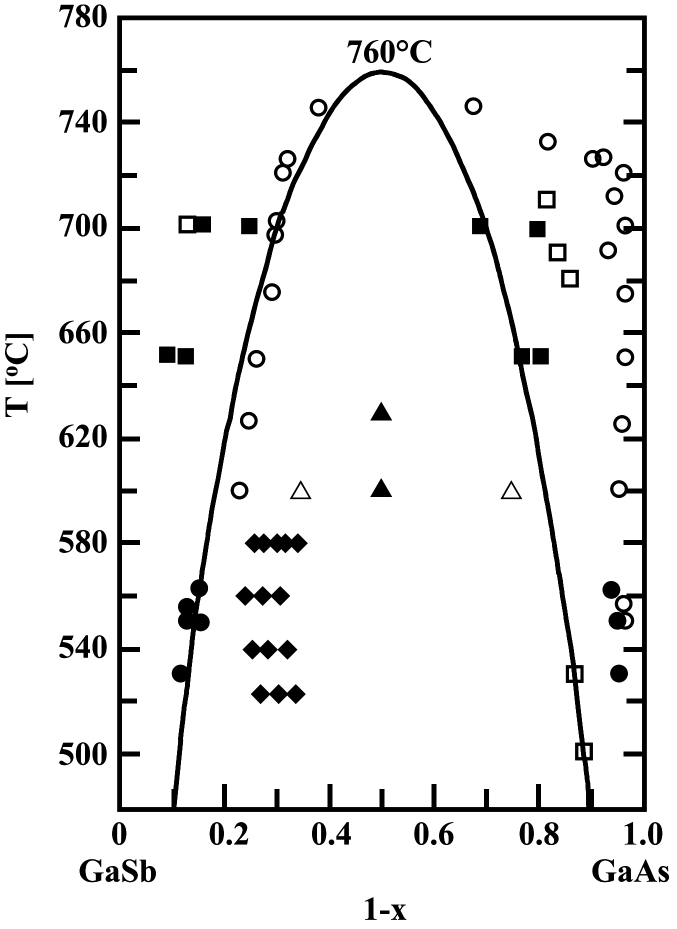

Figure 4.12 T_g vs Sb composition with calculated miscibility gap boundary. Data points are from the work of Pesseto et al. [106] (■), Gratton et al. [107] (○), Takenaka et al. [108] (□), Mani et al. [109] (●) - stated above by LPE; Cherng et al. [110] (▲), Cooper et al. [111] (△), and the present work (◆) - the rest were grown by MOCVD. The calculated curve is from the regular solution model.

4.3.2 Optimization of Growth Conditions and Structure

In order to achieve high-quality device structures, growth conditions must be investigated carefully. To optimize the material and optical properties of GaAsSb, large sets of GaAsSb QW structures have been grown with varying growth temperature, V/III ratio, QW thickness, the number of QWs, and barrier materials (GaAs, GaAsP, and InGaP).

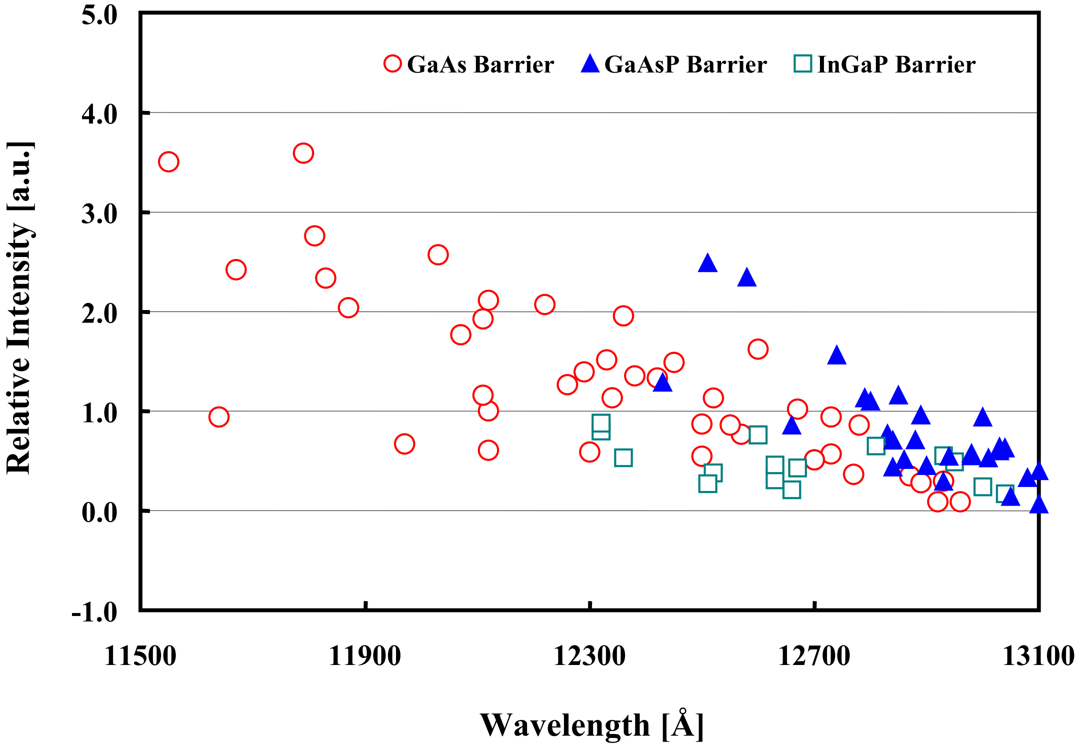

Figure 4.13 The RT-PL wavelength vs. PL intensity of GaAsSb QW structure with various barrier materials.

For the optical communication application, a laser that emits at a wavelength of at least 1.31 μm is required. To achieve that long wavelength, the Sb composition in the GaAsSb must be around 34 ~ 36%. However when the PL wavelength that comes from GaAsSb QW structure reaches that wavelength, the intensity drops to almost zero due to several reasons such as the Sb solidification on the interface, dislocation formation from lattice mismatch, etc. The PL intensity drop for various barrier materials is shown in Figure 4.13. Among those three barrier materials, GaAsP seems to be the most promising barrier material because even near the wavelength range of 1.3 μm, the PL intensity of the GaAsSb quantum-well with the GaAsP barriers is higher than those of the other barrier materials. In addition to barrier material selection, precise optimization of other growth conditions is very important.

The effect of T_g on material quality was first studied for GaAs/GaAsSb DQW-SCHs. For the "constant" growth conditions employed in each run, the Sb vapor composition was 21.85% and the nominal V/III ratio was 10.53. Only difference in each run is the growth temperature. As shown in Figure 4.14, the PL wavelength increases with increasing T_g. However, the PL intensity drops very quickly for T_g over 540 ºC. The relationship is clear in the inset showing the integrated PL intensity vs. T_g. The Sb solid composition increase with T_g accounts for the PL wavelength increase and the PL intensity drop. The Sb solid compositions measured by XRD were 26.9%, 28.7%, 29.8%, and 31.2% from samples grown from 520 ºC to 580 ºC. This result, however, is opposed to the MBE-grown GaAsSb case. It is reported that the As incorporation increases when the substrate temperature is increased [112,113]. We believe that this opposite result of

MOCVD grown GaAsSb is due to the increased pyrolysis of TMSb, which has 50% pyrolysis temperature of around 550 ºC.

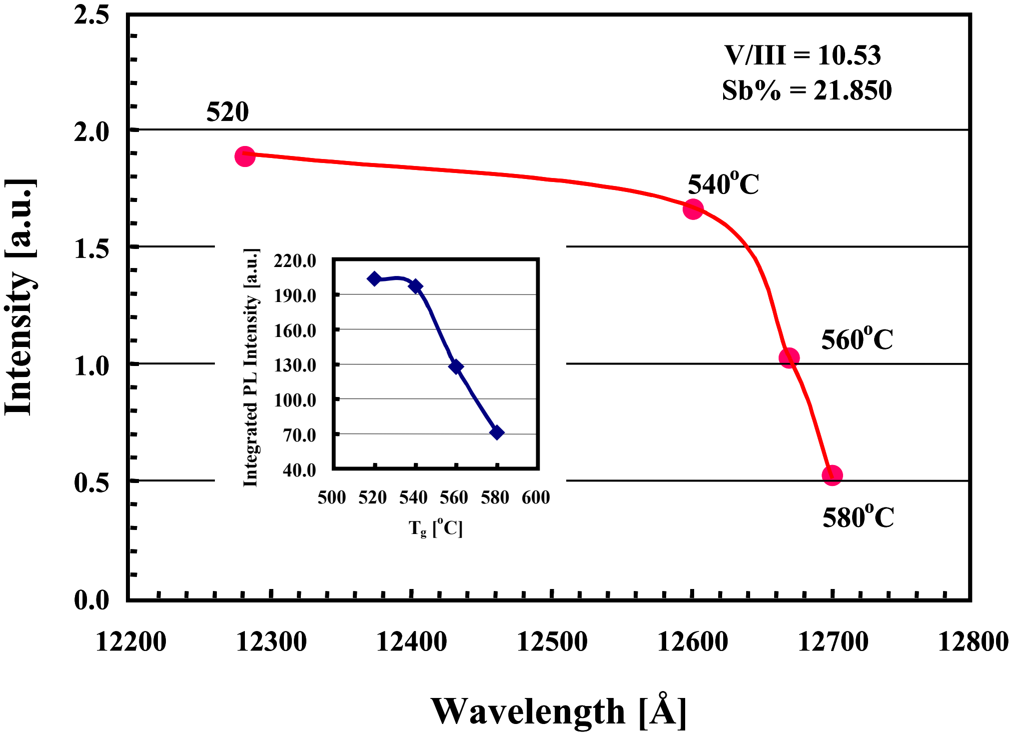

Figure 4.14 T_g effect on RT-PL intensity. Inset is integrated PL intensity vs. T_g

The T_g effect on the samples with same PL wavelength is investigated as well. In Figure 4.15, the PL intensity dependence on T_g is shown. If the samples have same PL wavelengths but the growth temperatures are different, the sample that is grown at lower temperature has a brighter PL intensity. This can be explained by the thermal degradation of the GaAsSb active or the interface region and by Sb segregation.

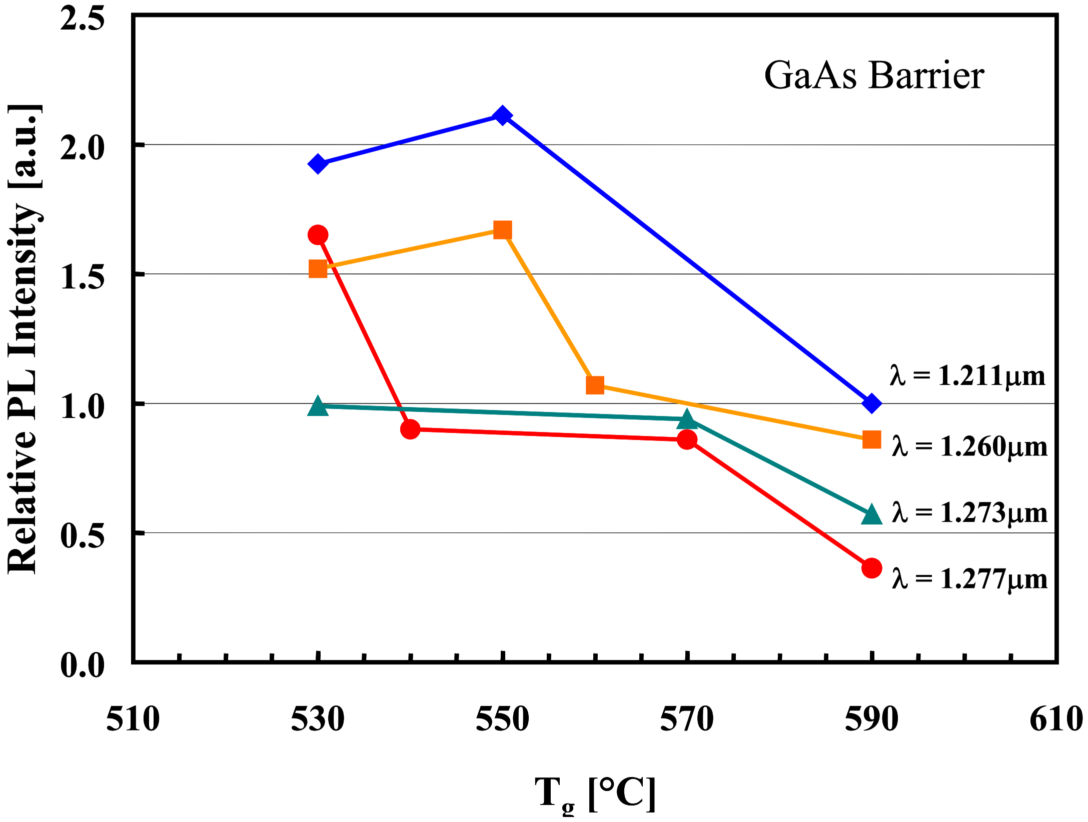

Figure 4.15 T_g effect on PL intensity of the samples with same wavelengths.

From these two results concerning the effect on material quality, we find that the optimum T_g for GaAsSb QW with GaAs barriers is around 520~560 ºC.

At a T_g of 530ºC, the V/III ratio effect on the Sb incorporation into the GaAsSb epitaxial layser was studied (shown in Figure 4.16) for the same structures. The V/III ratio was changed from 10 to 15 without changing the TMGa flow rate. As the V/III ratio increases, the Sb incorporation into solid GaAsSb decreases and the PL emission wavelength from the sample decreases to the shorter wavelength side. The Sb solid compositions are measured by XRD ω-2θ scan. Since the Sb vapor composition is fixed at 18.62%, the Sb solid composition should be same. However the decisive factor for the Sb solid composition is not the relative vapor composition, but the Sb incorporation into the solid. The strong competition between the incorporation of anions leads to the different sticking coefficients of As and Sb. Because the GaAs bonding is preferential to GaSb bonding, the abundant As species in the growth condition of high V/III ratio depletes Ga first, resulting in an As rich GaAsSb layer. This causes the wavelength to blue-shift as the V/III ratio increases. The residual Sb atoms could be segregated on the growth surface and make the quality of the epitaxial layer poor. The increasing of the PL intensity as the PL wavelength decreases (the intensity data are not shown in the figure, but the intensity of the 1.10 μm sample is almost 20 times higher than that of the 1.29 μm sample.) means that significant Sb segregation does not occur on the sample surface. Another possible explanation of the PL wavelength decrease as the V/III ratio increases is that the real increase of the As mole fraction is larger than that of Sb in the process because the V/III ratio is not real but is a nominal value.

The effect of the Sb molar flow rate change is relatively simple. Figure 4.17 shows the effect of the Sb vapor composition on the PL wavelength and intensity. The samples were grown at 530 ºC with a V/III ratio of 12.5. As the Sb vapor composition increases, the PL wavelength increase as expected.

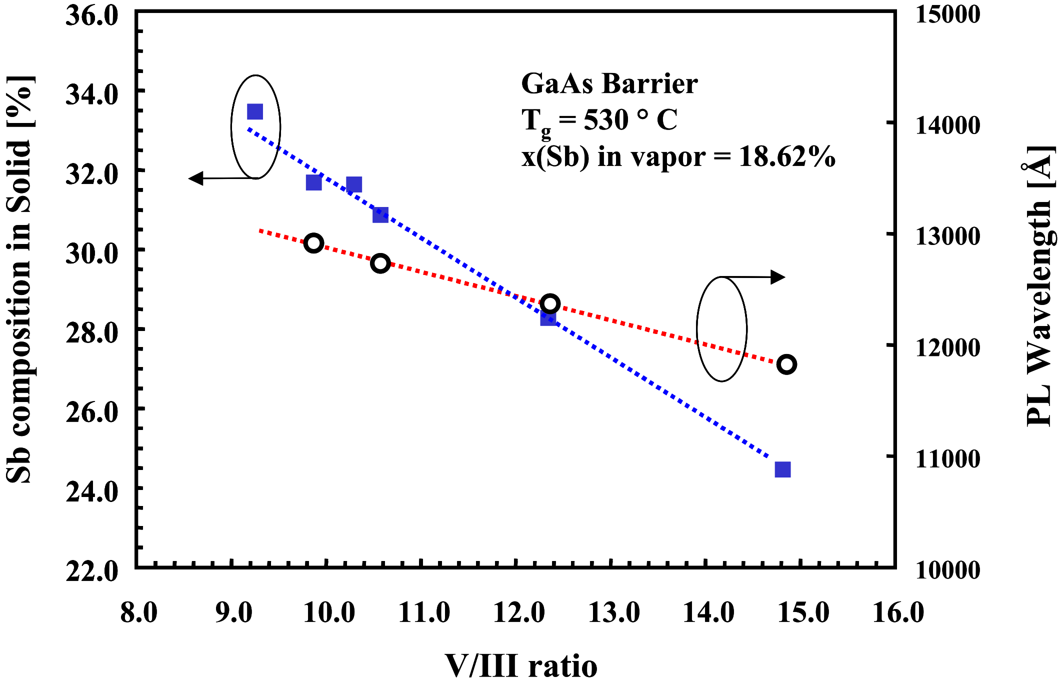

Figure 4.16 V/III effect on Sb incorporation into GaAsSb and on PL wavelength

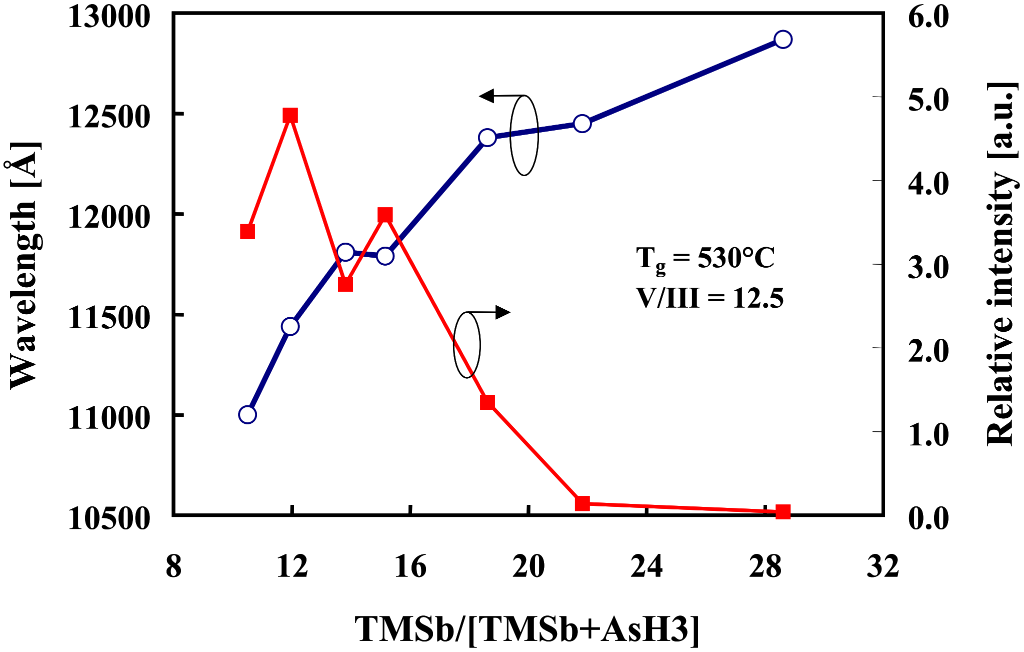

Figure 4.17 The effect of the Sb vapor compostion change on the PL wavelength and intensity for the GaAs barrier GaAsSb DQW-SCH structures.

The quantum-well thickness effect in the PL results is shown in Figure 4.18. The samples were grown at 530 ºC with a V/III ratio of 11.73. All samples have around a 31% Sb solid composition. When the QW thickness is 75 Å, the PL intensity has a maximum value. If the QW thickness decreases to 50 Å, the PL wavelength moves to the shorter side due to the quantum-confinement effect. The reduced intensity is attributed to the small carrier confinement in the active region. The sample with the 116 Å thick QW has the longest wavelength but the intensity is very dim because of strain relaxation and dislocation formation.

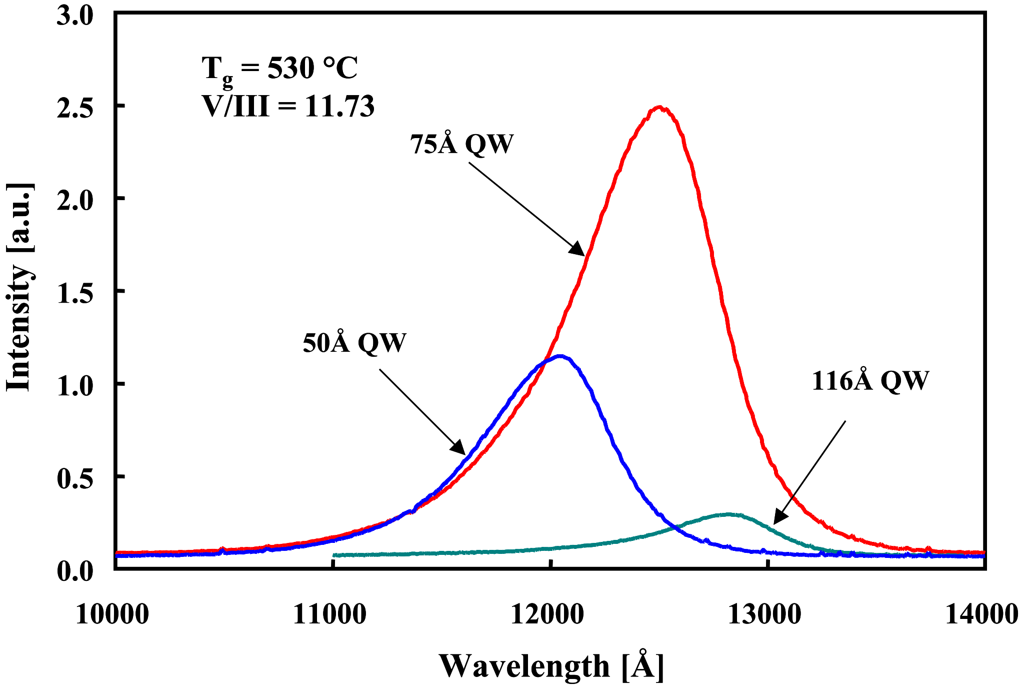

Figure 4.18 The QW thickness effect on PL wavelength and intensity for the GaAs barrier GaAsSb DQW-SCH structures.

Until this point, we investigated only GaAs barriers for GaAsSb QWs. As mentioned in Section 1.4 of Chapter 1, GaAs/GaAsSb heterostructure interface is believed to have a Type-II band lineup [42,43]. This means that photo-excited electrons are not confined in the GaAsSb QW and they recombine with holes through a spatially indirect transition, resulting in poor PL intensity. In comparison with a strained InGaAs QW standard sample emitting at 980nm, the GaAs barrier sample had almost 20 times lower PL intensity. To solve this poor PL intensity problem, we propose to employ larger bandgap barrier materials to make a Type-I band lineup with GaAsSb.

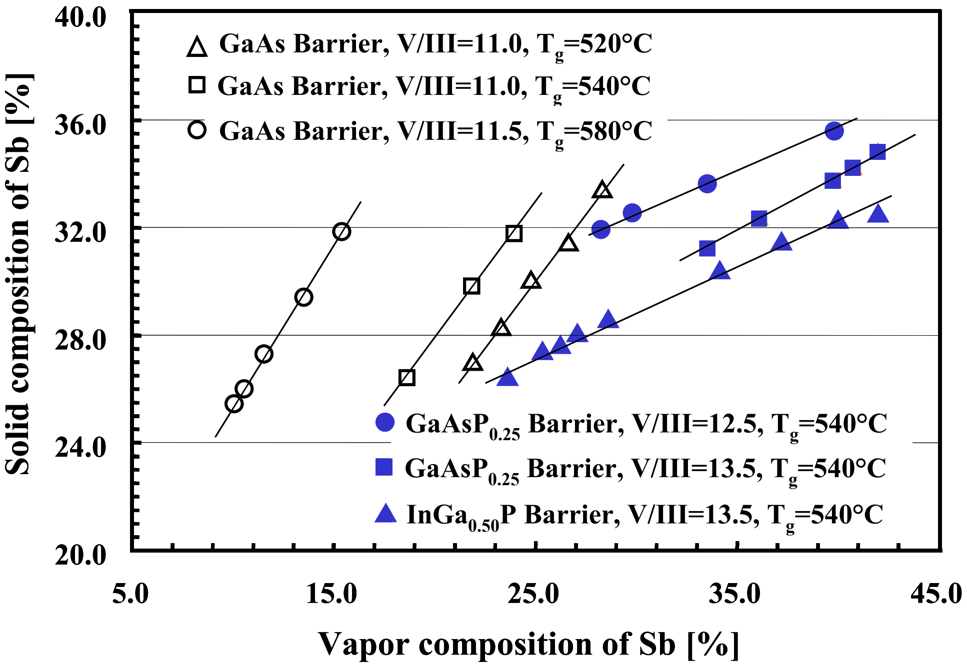

Figure 4.19 Sb vapor composition vs. solid composition with various barrier materials.

In Figure 4.19, the relation between the Sb vapor composition and the Sb solid composition is shown for various barrier materials. It is fairy linear dependence for all barrier cases. However, in P-containing barriers, the Sb incorporation rates are lower than that of the GaAs barrier case. The reason is unknown yet but we believe that some PH_3-related reactions occur during homogeneous or heterogeneous reactions, which inhibit Sb incorporation into solid GaAsSb.

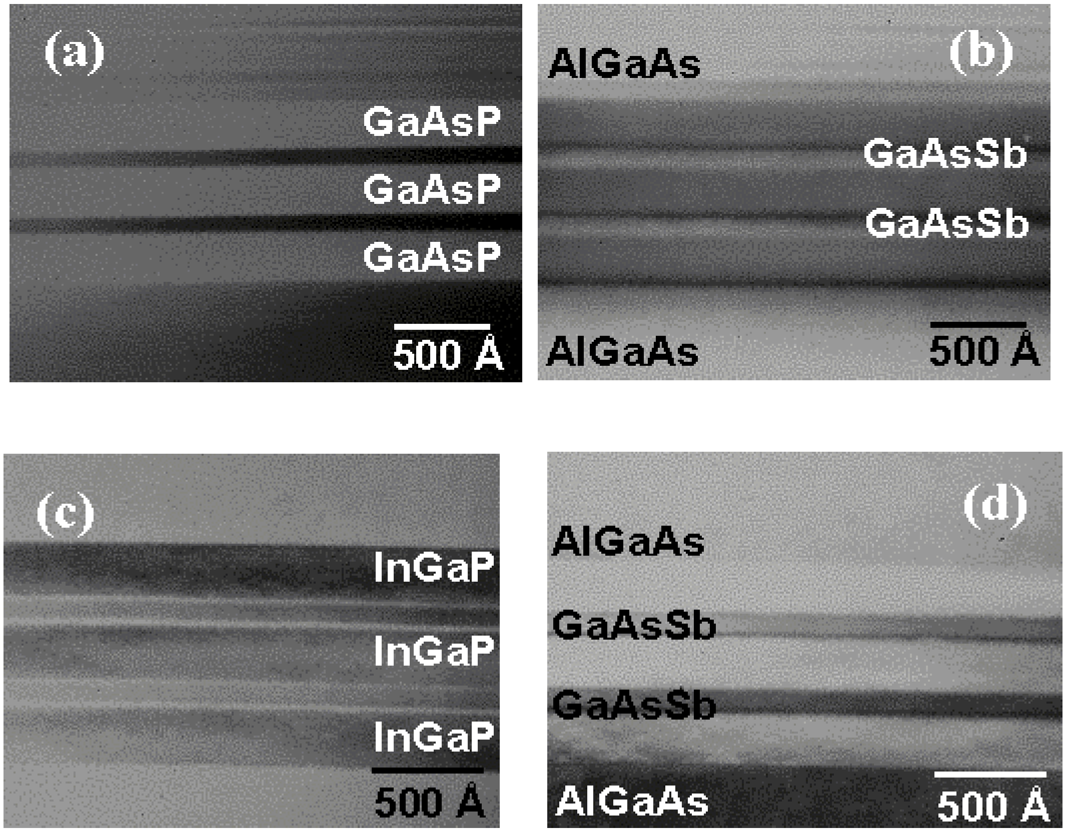

Figure 4.20 TEM images of GaAsP and InGaP barrier GaAsSb DQW structures ((a) and (c) are bright-field images and (b) and (d) are dark-field images).

Based on the optimization results of the GaAsSb QW structures with GaAs barriers, we could successfully grow InGaP- and GaAsP-barrier GaAsSb QW structures even at low T_g. In Figure 4.20, the TEM images of GaAsP-barrier and InGaP-barrier GaAsSb QW structures are shown. The images of (a) and (b) in Figure 4.20 are complementary ones for the $GaAs_{0.70}P_{0.30}$ barrier structure, one is a bright-field and the other is dark-field image. The 80 Å thick DQW appears to be dislocation free. The same high quality is verified in the 100 Å DQW with $In_{0.46}Ga_{0.54}P$ barrier structure. The TEM results show that the GaAsP and InGaP layers that are grown at low temperature (560 ºC) can be good barrier materials. The additional benefit of these larger-bandgap barrier materials is the strain compensation effect. Since Ga-rich InGaP and GaAsP are tensile-strained to GaAs substrate, these can compensate for the compressive strain of the GaAsSb QWs.

The relative PL intensities of the GaAsSb QW structures having various barrier materials are shown in Figure 4.21. The proposed larger bandgap ternary barrier materials dramatically improve the PL intensities, as is shown. The GaAsP barrier structures have the highest intensity even at 1.3 μm. The PL intensity ratio is 1:2:7 for GaAs, InGaP, and GaAsP barriers at the wavelength. This result is attributed to the Type-I band lineup formation of GaAsP and InGaP barrier structures.

The durability of these structures under thermal treatment is of great interest. The long-wavelength-emitting semiconductor laser requires relatively thick lower and upper cladding layers form a high-quality waveguide in order to prevent the radiated light in the active region from being lost to the other layers in the optical cavity, in particular, to the GaAs capping layer and the GaAs substrate. If the active region is not robust to thermal processing, the active region will degrade especially during the growth of upper cladding and capping layers. The minimum required thickness of the upper cladding layer for λ = 1.3 μm is around 1.0 μm (Actually it depends on the index of the cladding layer. If a higher Al-content AlGaAs layer is used as the cladding layer, the thickness can be reduced.). For typical growth rates of AlGaAs and GaAs, it would take 30 to 40 minutes to grow the upper layers. The annealing effect on the PL wavelength shift and intensity drop is shown in Figure 4.22. The annealing was performed at 650 ºC and 700 ºC in N_2 ambient for GaAs, GaAsP, and InGaP barriers. To minimize the experimental ambiguity, all three barrier samples were simultaneously put into the furnace for exposure to the same conditions, such that only difference is the structure of the samples.

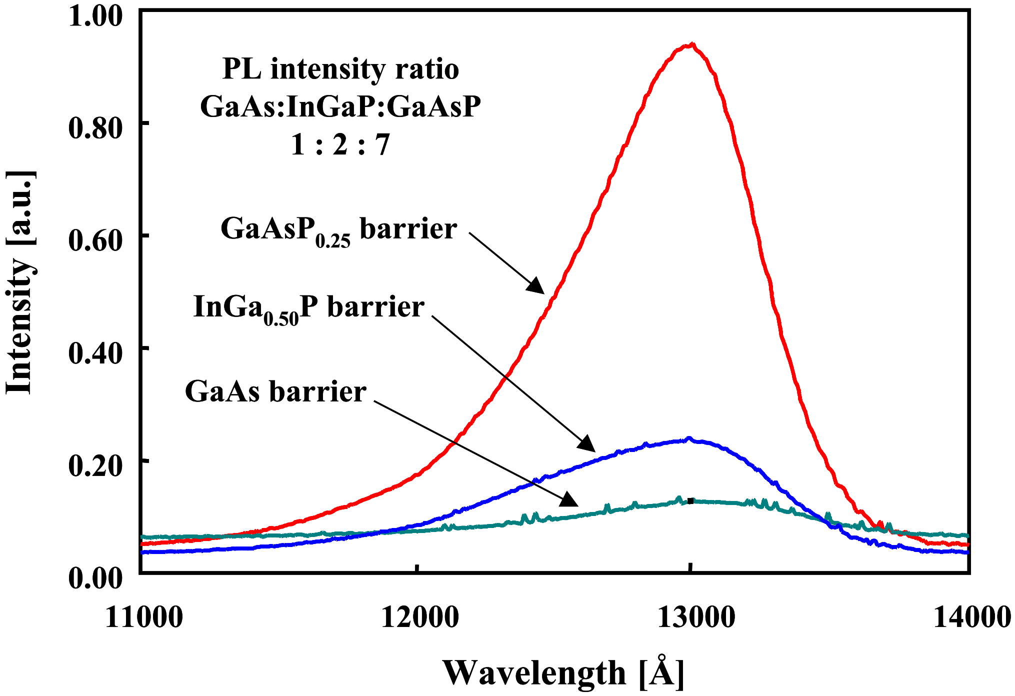

Figure 4.21 PL intensity ratio for GaAsSb DQW samples with various barrier materials.

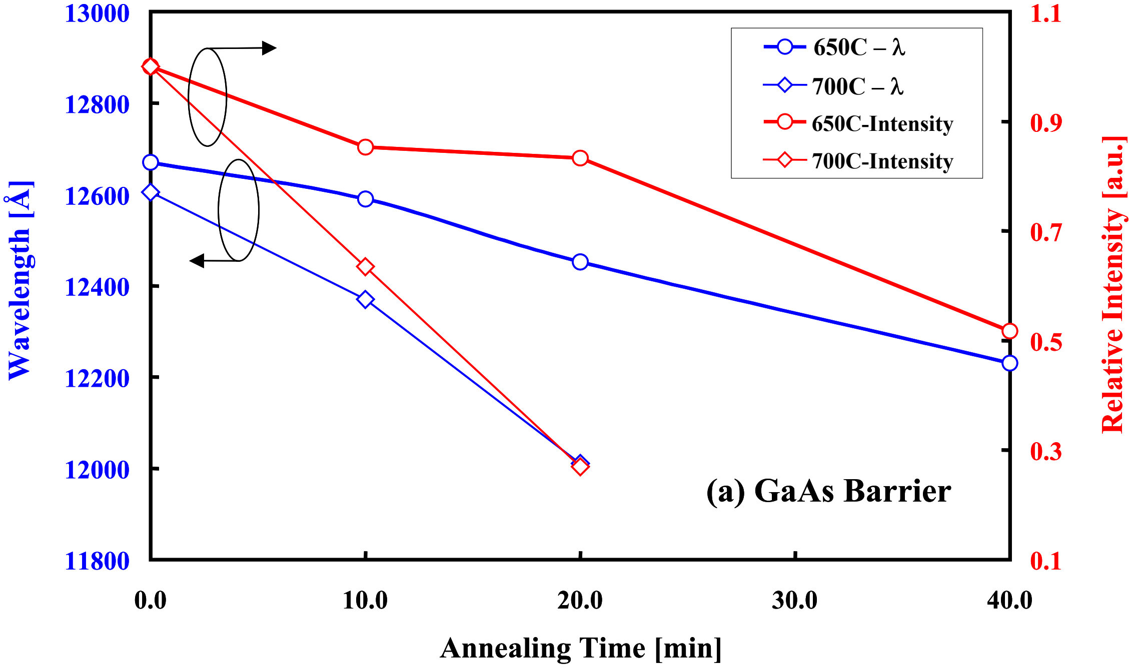

13000
12800
12600
12400
12200
12000
11800
Wavelength [Å]
1.1
0.9
0.7
0.5
0.3
0.1
Relative Intensity [a.u.]
0.0
10.0
20.0
30.0
40.0
Annealing Time [min]
650C – λ
700C – λ
650C-Intensity
700C-Intensity
(a) GaAs Barrier

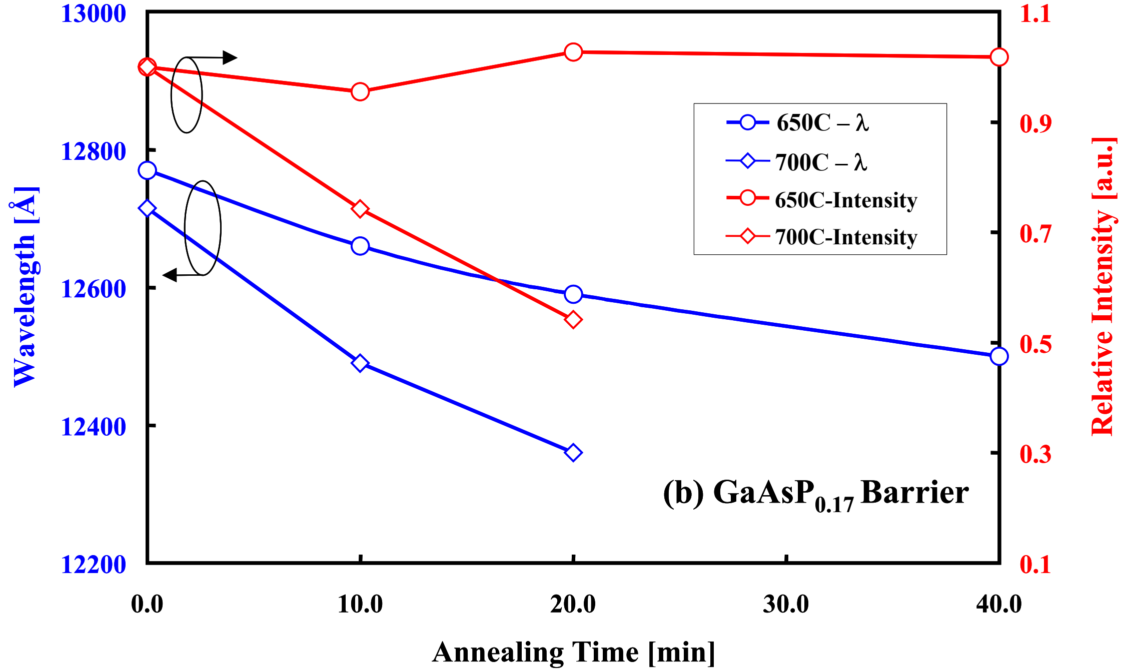

13000
12800
12600
12400
12200
Wavelength [Å]
1.1
0.9
0.7
0.5
0.3
0.1
Relative Intensity [a.u.]
0.0
10.0
20.0
30.0
40.0
Annealing Time [min]
650C – λ
700C – λ
650C-Intensity
700C-Intensity
(b) GaAsP$_{0.17}$ Barrier

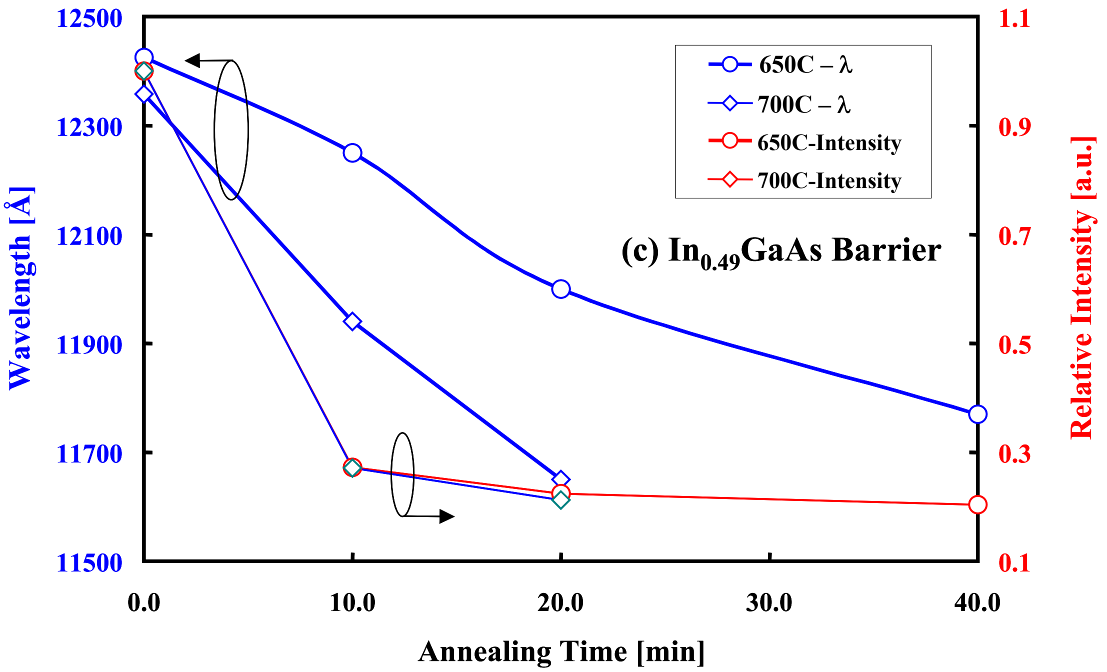

Figure 4.22 Annealing effect on the PL wavelength shift and the PL intensity degradation. The annealing experiments were performed at 650 ºC and 700 ºC in N_2 ambient. (a) GaAs Barrier, (b) GaAsP barrier, and (c) InGaP barrier.

A blue-shift of the PL wavelength has been observed in all three annealed samples. When the annealing temperature is high, the rate of the blue-shift is faster. At an 650 ºC annealing temperature, the time-dependence of the wavelength blue-shift is large on the order of InGaP (-16.56 Å/min) > GaAs (-11.25 Å/min) > GaAsP (-6.15 Å/min). The origin of the blue-shift is not yet clear. It is possibly attributed to the diffusion of P and As into the GaAsSb QWs. A PL intensity degradation was observed in all samples and all annealing conditions except for the GaAsP barrier sample with the 650 ºC annealing condition. The intensity was not changed for 40 minutes annealing under these conditions. Therefore if the upper cladding and capping layers in the laser structure are grorwn at 650 ºC within 40 min (in real applications, the laser structure should be grown shorter than 40 min, because for laser processing, several other thermal treatments such as annealing for Ohmic contacts, AlGaAs oxidation, etc., are required.), the active region containing GaAsP barriers and GaAsSb QWs can be viable. A large sudden intensity drop occurred in the InGaP barrier case with 10 minutes annealing time for both 650 ºC and 700 ºC annealing conditions.

Based on all above optimization results, the GaAsP barrier seems to be the most promising for GaAsSb QW laser structures.

4.4 BAND LINEUP DETERMINATION AND CALCULATION

Before starting this section, it is necessary to define the quantities needed to discuss energy band lineup and the calculations of these energies. Figure 4.23 shows a double heterostructure, which is composed of a compressively strained "active" layer and two identical "cladding" or "barrier" layers (e.g., GaAsSb and GaAs). E_g, ΔE, and δE are symbols used to refer to the energy bandgap of the material, the energy band offset, and the energy shift due to compressive strain, respectively. The subscripts of *c*, *hh*, and l*h* denote the conduction band, valence band heavy hole, and light hole states.

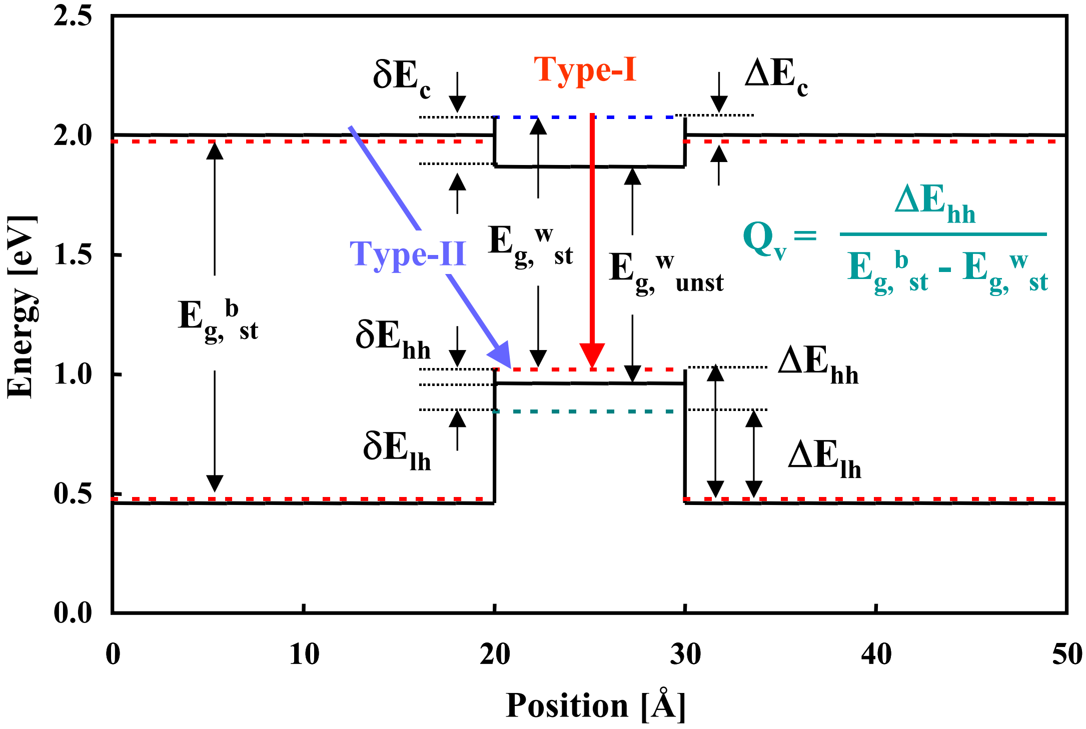

Figure 4.23 Definitions of Type-I, Type-II, Q_v, and relevant energies in heterostructure.

The "st" and "unst" labels are abbreviations referring to the strained and unstrained cases. The superscripts of *w* and *b* indicate the well and barrier, respectively. Type-I and Type-II mean the spatially direct and indirect transitions. The most useful and important parameter in the band lineup is the valence-band discontinuity factor, Q_v. When Q_v is greater than unity, the hetero-interface has Type-II band lineup and when Q_v is smaller than unity, it has Type-I band lineup.

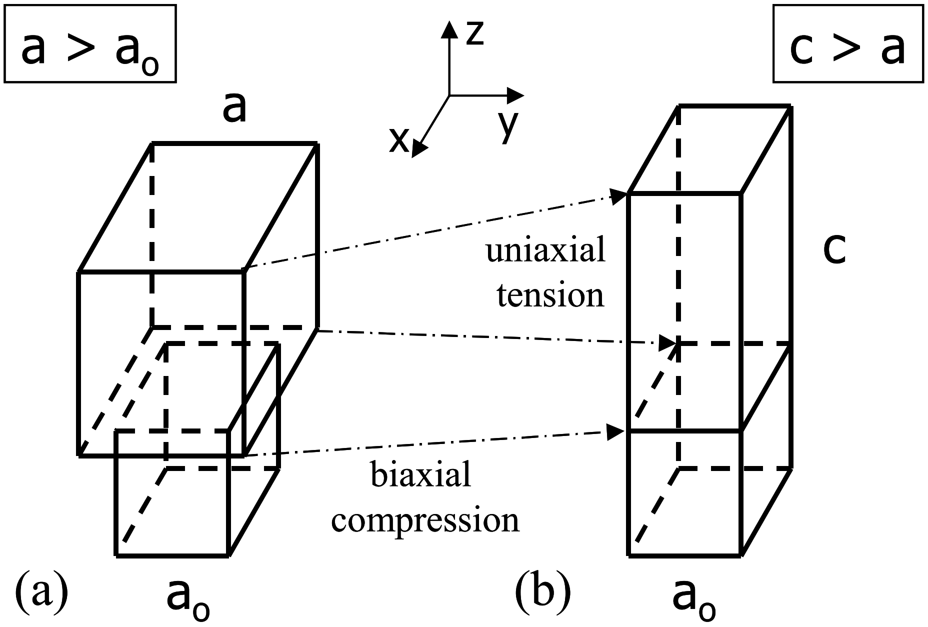

Figure 4.24 A layer with a lager lattice constant, *a* to be grown on a substrate with a lattice constant, a_o. (a) unstrained; (b) strained.

To determine the band lineup of a hetero-interface that has a strained layer, the energy shift due to the strain effect has to be calculated first. Since the electron-hole recombination occurs from the final states that have been changed by strain effect. When larger lattice constant cubic semiconductor is grown on the smaller lattice constant cubic substrate, the lattice in the plane of epitaxial growth shrinks to fit to the lattice constant of the substrate, and the lattice in the growth direction elongates. This causes a compressive strain in the larger lattice material (shown in Figure 4.24).

In this case, the strain in *x-y* plane is [32,114]

$$\varepsilon = \varepsilon_{xx} = \varepsilon_{yy} = \frac{a_0 - a}{a} \qquad \text{Equation 4.1}$$

where a_o and a are the lattice constants of the substrate and the layer, respectively. And the strain in the growth direction (z-direction) is

$$\varepsilon_{zz} = -2\frac{C_{12}}{C_{11}}\varepsilon \qquad \text{Equation 4.2}$$

where C_{12} and C_{11} are the elastic stiffness constants. The bandedge energy shift of heavy-hole (*hh*) band and light-hole (*lh*) band are given by

$$\delta E_{hh} = a_v(\varepsilon_{xx} + \varepsilon_{yy} + \varepsilon_{zz}) + \frac{b}{2}(\varepsilon_{xx} + \varepsilon_{yy} - 2\varepsilon_{zz}) \qquad \text{Equation 4.3a}$$

or $$\delta E_{hh} = [2a_v(1 - \frac{C_{12}}{C_{11}}) + b(1 + 2\frac{C_{12}}{C_{11}})]\varepsilon \qquad \text{Equation 4.3b}$$

$$\delta E_{lh} = a_v(\varepsilon_{xx} + \varepsilon_{yy} + \varepsilon_{zz}) - \frac{b}{2}(\varepsilon_{xx} + \varepsilon_{yy} - 2\varepsilon_{zz}) \qquad \text{Equation 4.4a}$$

or $$\delta E_{lh} = [2a_v(1 - \frac{C_{12}}{C_{11}}) - b(1 + 2\frac{C_{12}}{C_{11}})]\varepsilon \qquad \text{Equation 4.4b}$$

where a_v is the valence band hydrostatic deformation potential, and b is the valence band shear deformation potential. The conduction band energy shift is given by

$$\delta E_c = a_c(\varepsilon_{xx} + \varepsilon_{yy} + \varepsilon_{zz}) = 2a_c(1 - \frac{C_{12}}{C_{11}})\varepsilon \qquad \text{Equation 4.5}$$

For compressive strained layer, the conduction and the valence band edges are

$$E_c = E_{c0} + \delta E_c \qquad \text{Equation 4.6}$$

and

$$E_v = E_{v0} + \delta E_{hh} \qquad \text{Equation 4.7}$$

where the E_{co} and E_{vo} are the conduction band edge and valence band edge of the unstrained layer, respectively. Therefore if E_{vo} is known (because $E_{co} = E_{vo} + E_g$), the strained conduction band edge and valance band edges can be calculated using the above equations. Although there are several possible methods to calculate the valence band edge energy (E_{vo}) such as Anderson' electron affinity rule [115] and the model solid theory [116], unfortunately, it has been reported that these methods are not applicable to calculate E_{vo} (and hence the band lineup) for the GaAsSb/GaAs system [117]. Therefore the empirical method [118] has been used in this study.

The band lineup of the strained GaAsSb and GaAs hetero-interface was investigated experimentally first. To determine the band lineup of the hetero-interface with these materials, the low-temperature (10K) current-dependent cathodoluminescence (CL) has been studied for a 80 Å thick $GaAs_{0.73}Sb_{0.27}$/GaAs DQW sample. Figure 4.25 shows the LT-CL spectra of the structure. For low cathode currents ranging from 500 pA to 15 nA (Figure 4.25 (a)), only one peak (E_I) has been observed at 1050 nm. This is attributed to a spatially direct transition from the conduction band to the valence band of GaAsSb. As the cathode current is increased above 25 nA, the second peak appears and becomes dominant at the lower-energy side (E_{II}). The lower-energy peak is related to a Type-II transition, i.e., due to carrier recombination between electrons in the conduction band of the larger bandgap GaAs barriers and holes in the valence band of the smaller bandgap GaAsSb QWs. Due to the smaller energy bandgap of GaAsSb relative to that of GaAs and the Type-II transition, the peak wavelength of E_{II} is longer than that of E_{I} (inset in Figure 4.25 (b)). For the second peak (E_{II}), a prominent blue shift is observed in contrast to peak E_{I}. Further increase of the cathode current above 250 nA does not change the peak energy position of E_{II}. This can be explained by noting that the spatially separated electrons and holes contribute to bend the energy band in the interface of conduction band side and the electrons in the bent conduction band of the GaAs barriers fill up to a higher energy level. The electrons in the band-bending states overflow and spread out into the GaAs barriers as the cathode current keeps increasing. Once the electron overflow starts, the transition energy cannot increase. Consequently, the blue shift of the recombination peak of E_{II} stops. From the LT-CL spectra, the determined Q_v value of the sample is 1.20 at 10K.

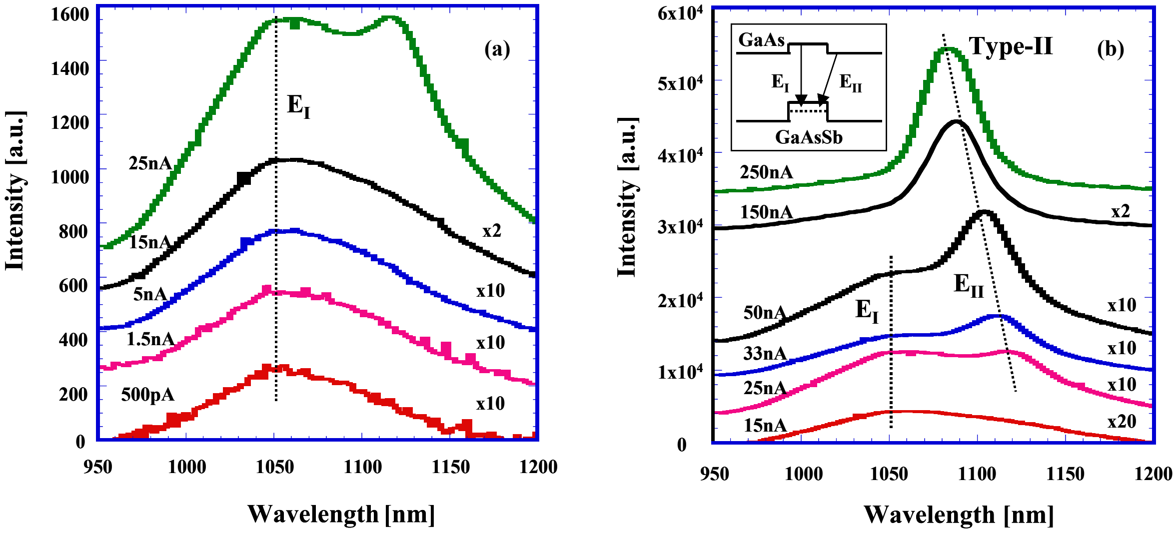

Figure 4.25 Low-temperature current-dependent CL of 80Å DQW $GaAs_{0.73}Sb_{0.27}$ with GaAs barriers at 10K. (a) Spatially direct transition (Type-I) at low cathode current, (b) Type-II transition at high cathode current. The band diagram is shown in inset.

In order to confirm the energy band lineup, Q_v is calculated as a function of x_{sb} by using an empirical method. The parameters that are used in the calculation are listed in Table 4.1 [28].

The values for intermediate compositions of $GaAs_{1-x}Sb_x$ are interpolated linearly from those of GaAs and GaSb binary data except for the bandgap energy. A widely accepted experimentally determined energy bandgap equation was used for the unstrained bulk $GaAs_{1-x}Sb_x$ at room temperature [119].

$$E_g(x) = 1.424 - 1.90x + 1.2x^2 \qquad \text{Equation 4.8}$$

Table 4.1 Material parameters for the calculation of the valence band discontinuity ratio (Q_v).

Parameter	Simbol	GaAs	GaSb	GaP	InP	AlAs
Lattice constant	**a [Å]**	**5.65325**	**6.09593**	**5.45052**	**5.86871**	**5.66000**
Elastic stiffness [10^{11} dyn/cm^2]	**C_{11}**	**11.910**	**8.834**	**14.040**	**10.110**	**12.020**
	C_{12}	**5.381**	**4.023**	**6.203**	**5.610**	**5.700**
Hydrostatic deformation potential [eV]						
Conduction band	**a_c**	**-7.17**	**-6.85**	**-7.14**	**-5.04**	**-5.64**
Valence band	**a_v**	**1.16**	**0.79**	**1.69**	**1.27**	**2.47**
Shear deformation potential	**b [eV]**	**-1.70**	**-1.80**	**-1.50**	**-2.00**	**-1.50**
e effective mass	**m_e/m_o**	**0.067**	**0.045**	**1.860**	**0.075**	**0.790**
h effective mass	**m_h/m_o**	**0.490**	**0.400**	**0.540**	**0.560**	**0.760**
Valence band edge*		**0.48**	**1.16**	**0.29**	**0.20**	**0.00**
Bandgap	**E_g [eV]**	**1.424**	**0.725**	**2.272**	**1.344**	**2.153**

* See ref. [118]

Figure 4.26 shows the calculated energies and the corresponding band lineup of $GaAs_{0.73}Sb_{0.27}$/ GaAs. The band lineup for the unstrained case (solid line) implies a Type-I transition ($Q_v < 1$), but the final transition, which includes the strain effect, comes from a Type-II band lineup ($Q_v > 1$). The calculated strained bandgap of $GaAs_{0.73}Sb_{0.27}$ is 1.115 eV and the valence band offset (ΔE_v) is 0.441 eV. From Equation 1.5, the Q_v is calculated to be ~1.43. This value is larger than that of the LT-CL result. We believe that the discrepancy between these two values is due to the dependence of material parameters (e.g., elastic stiffness) on temperature.

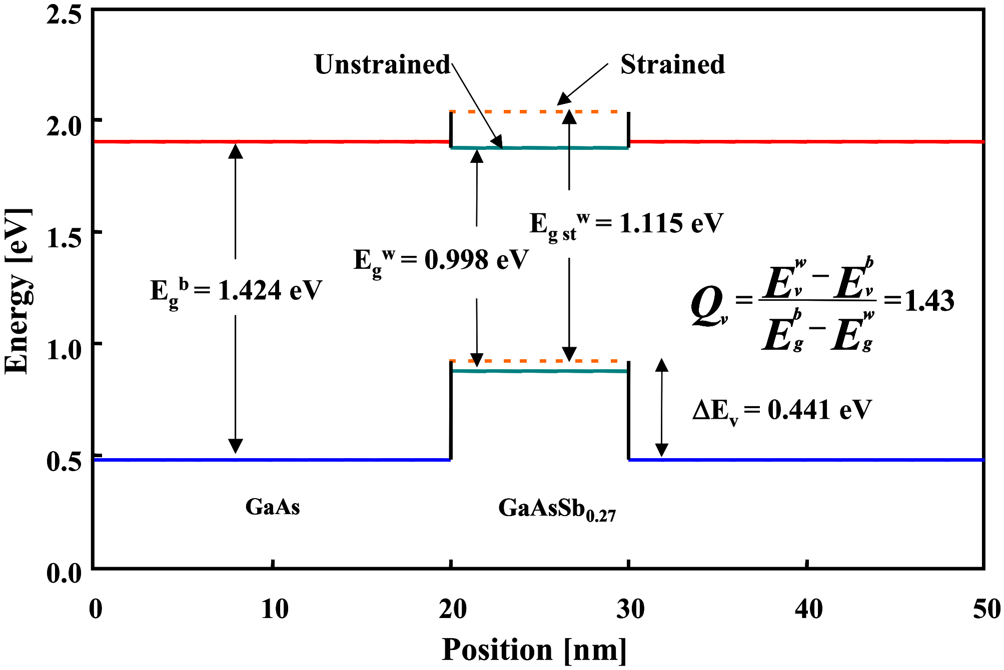

Figure 4.26 Calculated band lineup between a $GaAs_{0.73}Sb_{0.27}$ QW and a GaAs barrier. Solid and dotted lines indicate the unstrained and strained case, respectively.

The calculated energies and Q_v have also been compared to the room-temperature PL spectra from various runs. In Figure 4.27, line (a) is the variation of the bandgap of unstrained bulk GaAsSb. The calculated Type-II and Type-I transitions determined by the empirical method, which include the strain effect, are shown in line (b) and line (c), respectively.

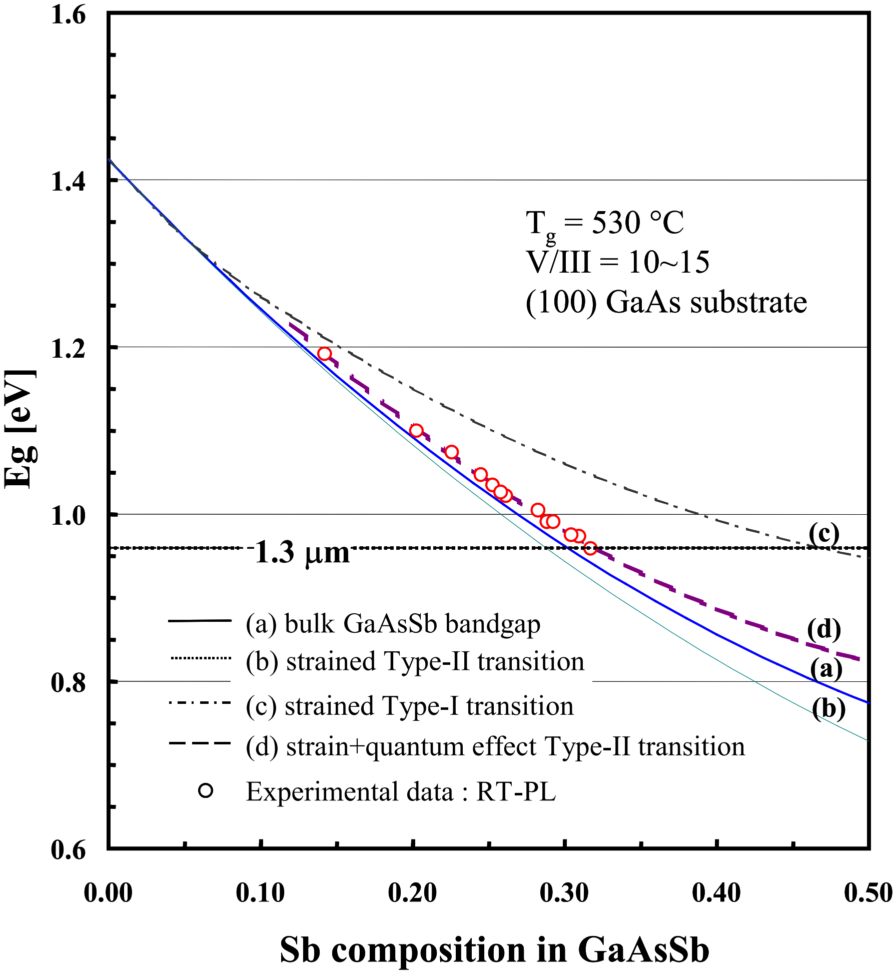

Figure 4.27 Comparison between the calculated energies and experimental RT-PL data.

The relation of the Sb composition and the Type-II transition energy is fitted as $E = 1.424-1.9515x+1.047x^2$. In line (d), we add up the quantum-confinement effect for the 80 Å QW only for the valence band because electrons exist in the thicker GaAs barriers, not in the GaAsSb QW state, such that the quantum effects for the conduction band electrons is very small. The circles in the figure are experimental data that are taken from the RT-PL and as shown in the plot, the experimental data are very well matched with line (d). From this comparison, it is concluded that the GaAsSb/GaAs heterostructure-interface has a Type-II band lineup for all Sb compositions when the GaAsSb QW grown on the GaAs substrate is in a strained condition.

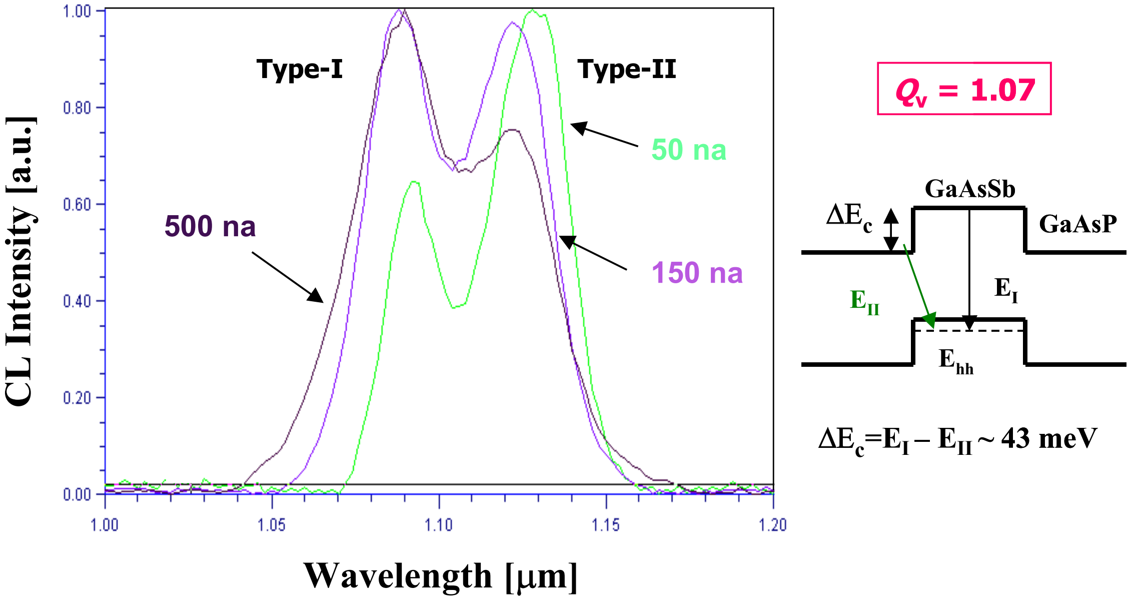

Figure 4.28 Low-temperature current-dependent CL of 80Å DQW $GaAs_{0.70}Sb_{0.30}$ with $GaAsP_{0.14}$ barriers at 10K

In the $GaAsP_{0.14}$ barrier case, a similar result to that of the GaAs barrier has been observed. The active region used in the structure is an 80 Å $GaAs_{0.70}Sb_{0.30}$ DQW. Very weak Type-II band lineup was obtained from LT-CL (in Figure 4.28) and the calculated Q_v is 1.07. Although the band lineup of the sample has a Type-II interface, it can be deduced that if the P compositions in GaAsP barriers are high enough, it is possible to make Type-I band lineup.

For the same reason, DQW-SCH samples having an $In_{0.5}Ga_{0.5}P$ barrier with an 80Å $GaAs_{0.67}Sb_{0.33}$ QW is measured by LT-CL at 10K. Figure 4.29 shows the current-dependent CL spectra for the sample. In contrast to the previous LT-CL results, all peak positions are located at almost the same wavelength. This is the reason why the Q_v value cannot be calculated directly from the CL data. Sometimes it is very complicated to explain the origin of the inverse S shape of the PL (or CL) peak shift in temperature- or power-dependent PL (or CL) (Figure 4.25). Since composition inhomogeneities due to ordering, phase separation, or composition fluctuation [120] and Type-II band lineup [121] cause similar inverse PL spectra, we further discuss the origin of the effect. Figure 4.29 shows good evidence of the homogeneity of the GaAsSb QW. Because both layers were grown using almost the same conditions except for the barrier materials, if the GaAs/GaAsSb structures have phase separation, then so do the InGaP/GaAsSb structures. However, the InGaP-barrier CL data has only a single peak, meaning that the inverse S shape peak shift in the GaAs/GaAsSb CP data originates from the Type-II transitions. In addition, it is possible to conclude that InGaP/GaAsSb has a Type-I hetero-interface. Using the empirical method, Q_v of this sample is determined to be 0.89. We believe that this is the first time that the band lineup between GaAsSb QW and InGaP barriers has been determined.

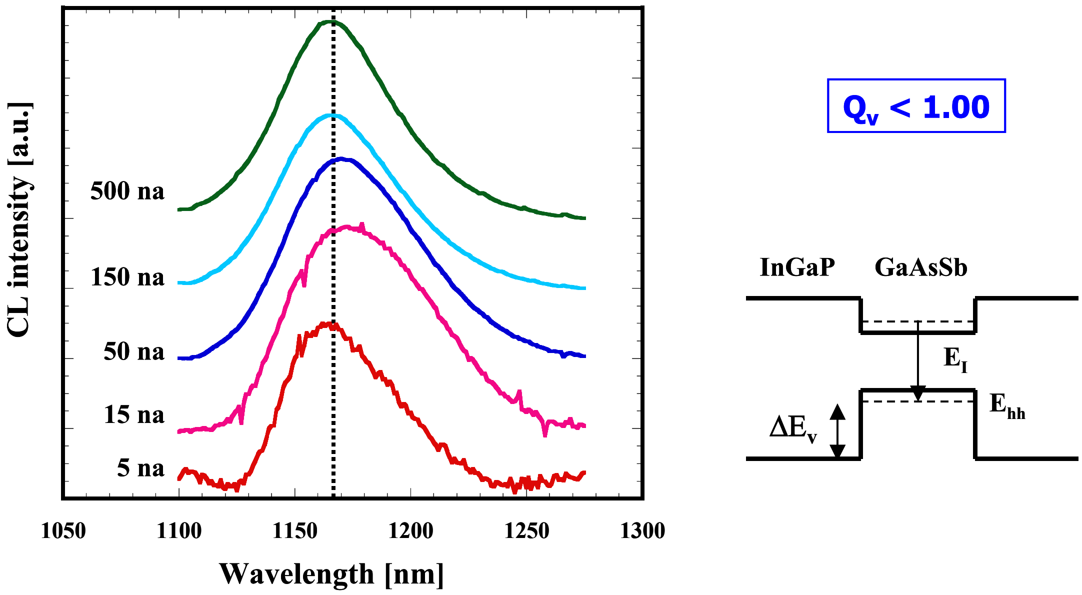

Figure 4.29 Low-temperature current-dependent CL of an 80Å DQW $GaAs_{0.67}Sb_{0.33}$ with $In_{0.5}Ga_{0.5}P$ barriers at 10K.

In addition to single composition simulation, Type-I/Type-II boundaries are calculated as a function of Sb composition for $InGa_yP$ barriers and $GaAsP_z$ barriers. Figure 4.30 shows that there exists a transient y(Ga) and x(P) composition in $InGa_yP$ and in $GaAsP_z$ for each Sb compostion in GaAsSb to form a Type-I band lineup. If we use an appropriate barrier composition to make a Type-I transition, it is possible to increase the PL intensity considerably and fabricate high-performance devices. The effort to form a Type-I band lineup is in the same direction as that of strain-compensation. Therefore, we can take additional advantage from this approach.

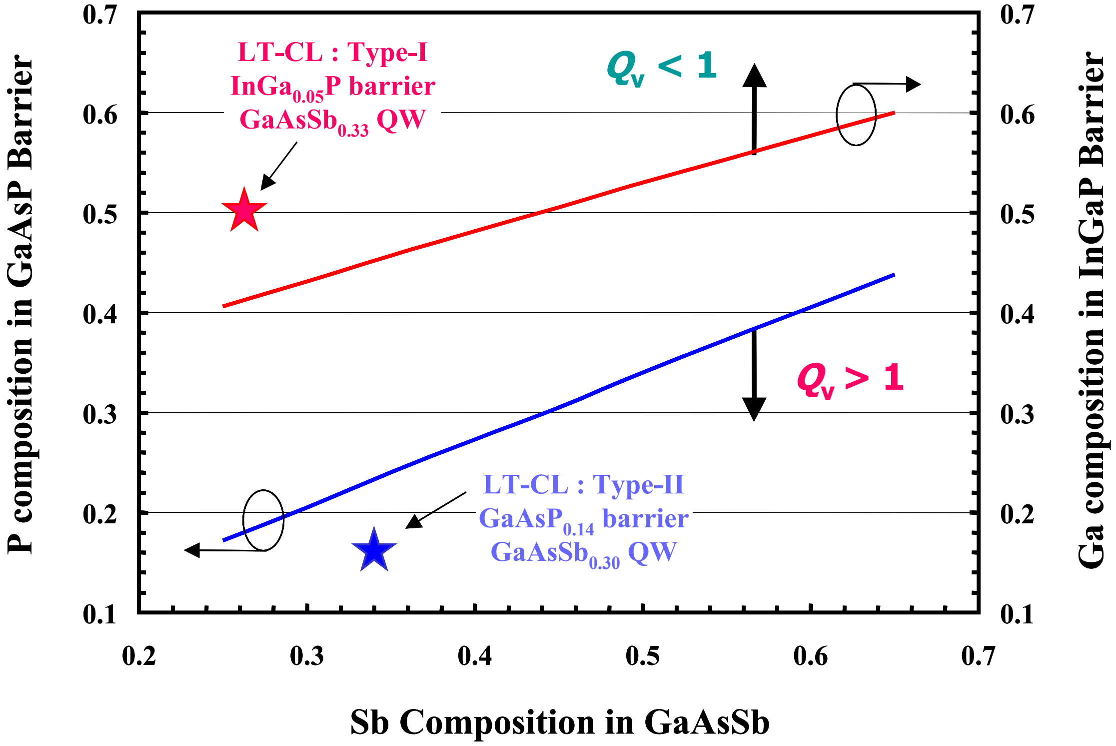

Figure 4.30 Type-I/Type-II boundary as a function of Sb compostion for barrier materials.

Chapter 5: GaAsSb Lasers

In this chapter, the laser diodes that have GaAsSb active QW layers are discussed. Based on the optimization of the growth conditions and barrier materials, we have grown GaAsSb active-region laser structures and fabricated broad-area metal contact lasers or oxidation confined lasers for CW operation. As for the barrier layers, GaAs and GaAsP materials were employed. The laser structures with InGaP barriers have also been tried, however those samples did not lase at 300 K. For the purpose of comparison to GaAsSb lasers, shorter-wavelength InGaAs active QW lasers were grown and fabricated. The other purposes of making an InGaAs/GaAs strained QW laser are to check the performance of the MOVCD growth system and to confirm the performance of the stack of all the other device layers (such as n-type cladding, active region, and p-type cladding layers).

5.1 INGAAS QW LASER

In the early stage of this study, we have grown GaAsSb/GaAs laser structures and fabricated laser diodes several times, but unfortunately, the performance of those devices was very poor (almost all devices did not lase). Because of this, we grew and fabricated a more conventional InGaAs/GaAs strained DQW-SCH laser using the same growth and doping conditions for the AlGaAs and GaAs layers as is used for the GaAsSb laser structure discussed in Chapter 4 in order to help determine where the problems related to the GaAsSb DQW injection lasers came from, i.e., whether this is due to the GaAsSb/GaAs material itself or due to other growth conditions including the quality of the cladding and cap layer materials that were grown by MOCVD. Since an InGaAs/GaAs laser structure that emits wavelengths at around 0.9 ~ 1.0 μm has a much better material quality (hence a brighter PL intensity) than that of the GaAsSb active-region lasers, it is relatively easy to make good InGaAs/GaAs laser devices. If this material structure does not lase, it means that the failure-to-lase problem of the GaAsSb/GaAs laser structures results from one or all of the reasons of quite low doping in the n- and p- type layers, the formation of the junction at an improper position, and the poor quality of the GaAsSb active region.

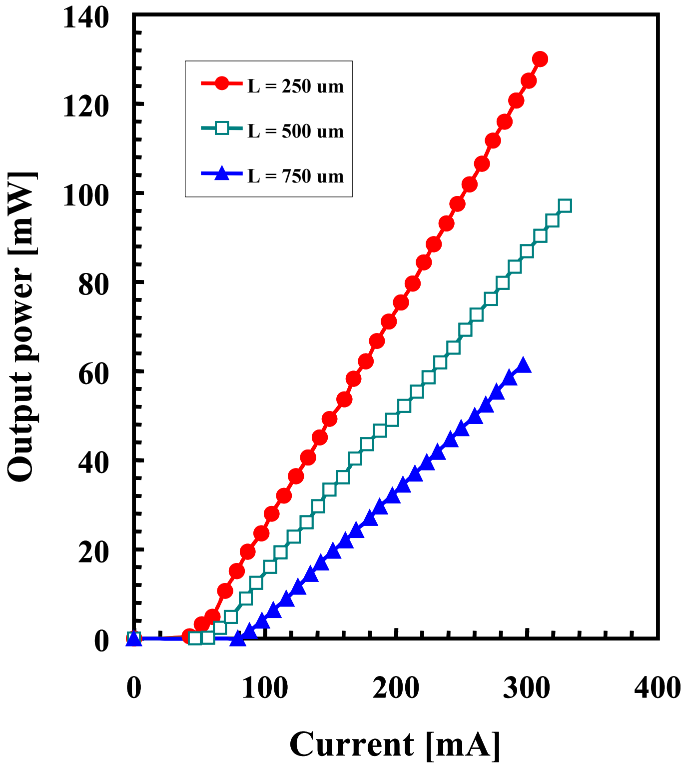

Figure 5.1 Light-current curves from broad-area InGaAs/GaAs DQW-SCH lasers under pulsed operation at RT.

The light output versus current (*L-I*) curves of the devices are shown in Figure 5.1. The structure consists of an 2 x 10^{18} cm^{-3} Si-doped n-type GaAs buffer, 2 x 10^{18} cm^{-3}, and 5 x 10^{17} cm^{-3} Si-doped n-type $Al_{0.45}GaAs$ lower cladding layers (total thickness is 1.0 μm), undoped 100 Å $In_{0.13}GaAs$ DQW, 5 x 10^{17} cm^{-3}, and 2 x 10^{18} cm^{-3} C-doped p-type $Al_{0.45}GaAs$ upper cladding layers (total thickness is 1.0 μm), and 3 x 10^{18} cm^{-3} C-doped p-type 0.1 μm-thick GaAs capping layer.

The threshold current (I_{th}) and threshold current density (J_{th}) of the device with a cavity length of 250 μm and a 50 μm-wide metal stripe were only 47.6 mA and 381 A/cm^2 under pulsed operation, respectively. The maximum output power of 130 mW was achieved from uncoated laser from one facet without any kinks observed in the *L-I* curve. The slope efficiency was 0.49 mW/mA. The *L-I* curves from diodes with different device dimensions are shown together in Figure 5.1. From these results, we can conclude that the MOCVD system and other layers are fairly good for the InGaAs strained QW laser application and the problem of the GaAsSb/GaAs QW lasers come from the quality of the active material. Figure 5.2 shows the threshold current density dependence upon the inverse cavity length. An infinite cavity length threshold current density (J_∞) of 129.24 A/cm^2 is extrapolated from the J_{th} vs. inverse cavity length data.

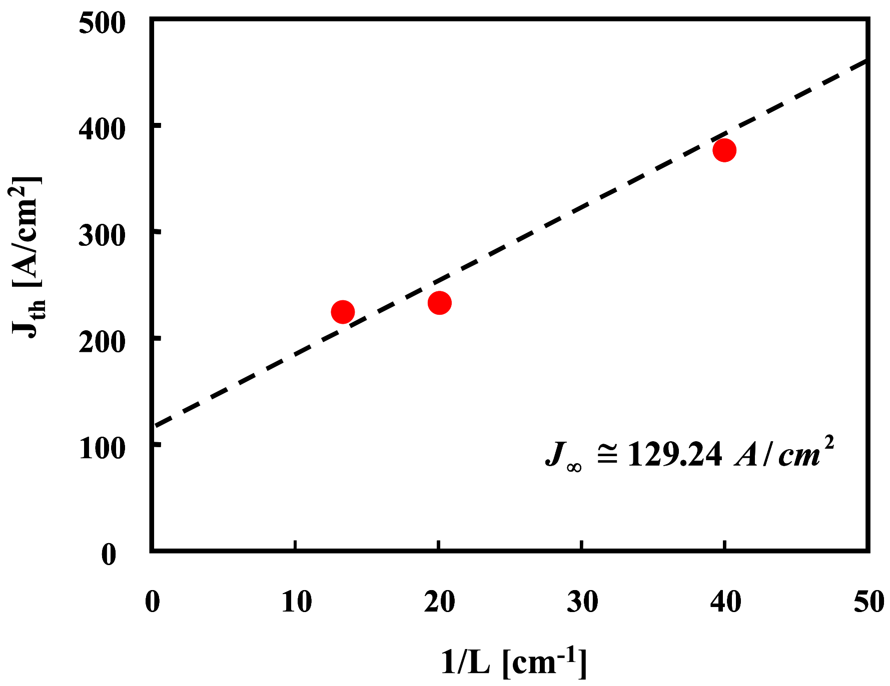

Figure 5.2 Threshold current density vs. inverse cavity length.

5.2 GAASSB QW LASER

Based on the InGaAs QW active laser and further optimization of the GaAsSb growth conditions, GaAsSb QW laser structures with GaAs barriers and GaAsP barriers are grown monolithically by MOCVD. The structures and characteristics of the laser devices are discussed in this section. For the GaAs barrier laser, 1.228 μm CW emitting wavelength was achieved, and for the GaAsP barrier, CW operation was achieved at λ =

1.274 μm. To our best knowledge, these two emitting wavelengths are the longest CW operated ones from GaAsSb QW lasers that are grown monolithically by MOCVD.

5.2.1 GaAsSb laser with GaAs barriers

Figure 5.3 shows the schematic diagram of the GaAsSb SQW-SCH laser structure with GaAs barriers. The structure is similar to that of the InGaAs QW laser except for the active region and the Al composition of cladding layers. Since a higher Al composition in the AlGaAs cladding layers gives a better optical confinement and also has a faster growth rate, the total growth time for the upper cladding layers can be reduced, resulting in the thermal degradation of active region being minimized.

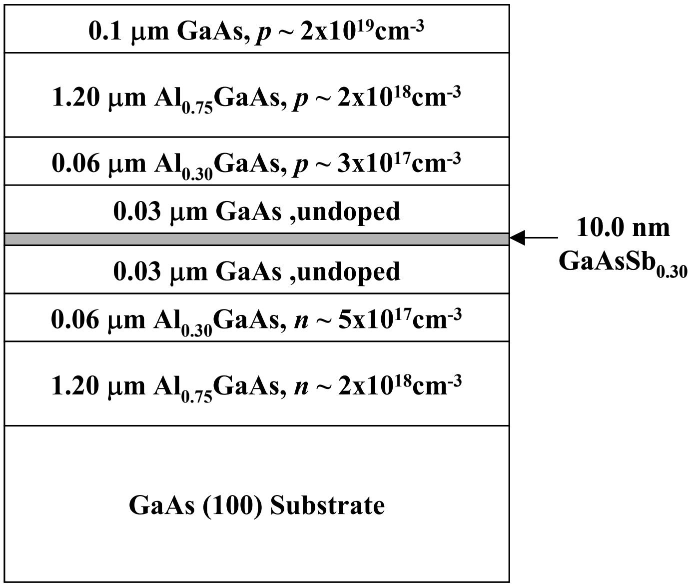

Figure 5.3 Schematic diagram of the GaAsSb SQW laser structure with GaAs barriers.

The GaAsSb QW region was grown at 570 ºC with a V/III ratio of 14.13. The T_g is slightly higher than that of the optimized conditions because after several maintenance procedures such as reactor cleaning, and platter cleaning, the optimized T_g condition has been changed. However we believe that the new growth temperature is within the optimized old growth temperature range from the results of repeated runs with the same recipes before and after those reactor maintenance events. The processed laser devices were lased under CW operation at 300 K with an I_{th} of 265 mA. The device had a cavity dimension of 1000 μm-long and employed a 20 μm-wide metal stripe. The maximum output power per facet was 10 mW.

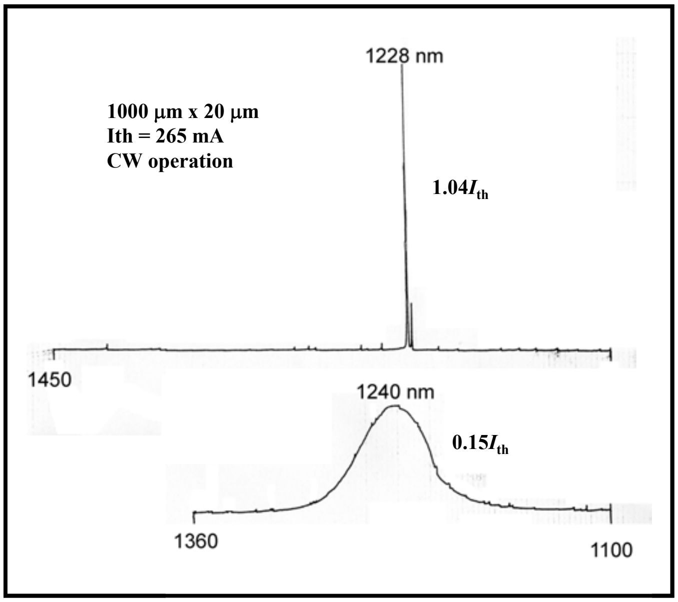

Figure 5.4 The CW lasing spectra of GaAs barrier GaAsSb laser below and above I_{th}.

The slope efficiency was 0.12 mW/mA and we note that this is very small compared to the InGaAs QW lasers described above (0.49 mW/mA). This low efficiency can be attributed to spatially indirect carrier transition characteristic of the GaAsSb/GaAs Type-II band lineup. The spectra of below and above I_{th} are shown in Figure 5.4. The CW lasing wavelength of 1.228 μm was achieved at $1.04I_{th}$.

5.2.2 Strain-compensated GaAsSb laser with GaAsP barriers

To improve the laser performance, GaAsP has been used as barrier materials to compensate for compressive strain in GaAsSb QWs and to achieve Type-I band lineup for better carrier confinement.

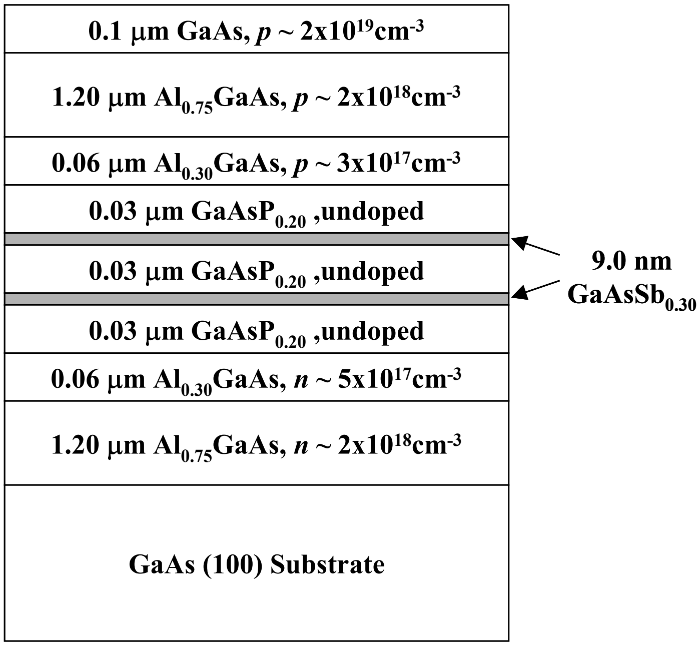

Figure 5.5 Schematic diagram of the GaAsSb DQW laser structure with GaAsP barriers.

Figure 5.5 shows the schematic diagram of the GaAsP-barrier GaAsSb DQW-separate-confinement-heterostructure (SCH) [122]. The structure is similar to the GaAs-barrier GaAsSb QW laser (Figure 5.3) except for the barrier materials. The active region was grown at 550 ºC with a V/III ratio of 14.82. The solid Sb and P compositions in GaAsSb QW and GaAsP barrier were 30%, and 20%, respectively. Those compositions were determined by using high-resolution XRD and dynamic X-ray diffraction simulations. The conventional 60 μm-wide stripe-geometry broad-area lasers were fabricated with various cavity lengths.

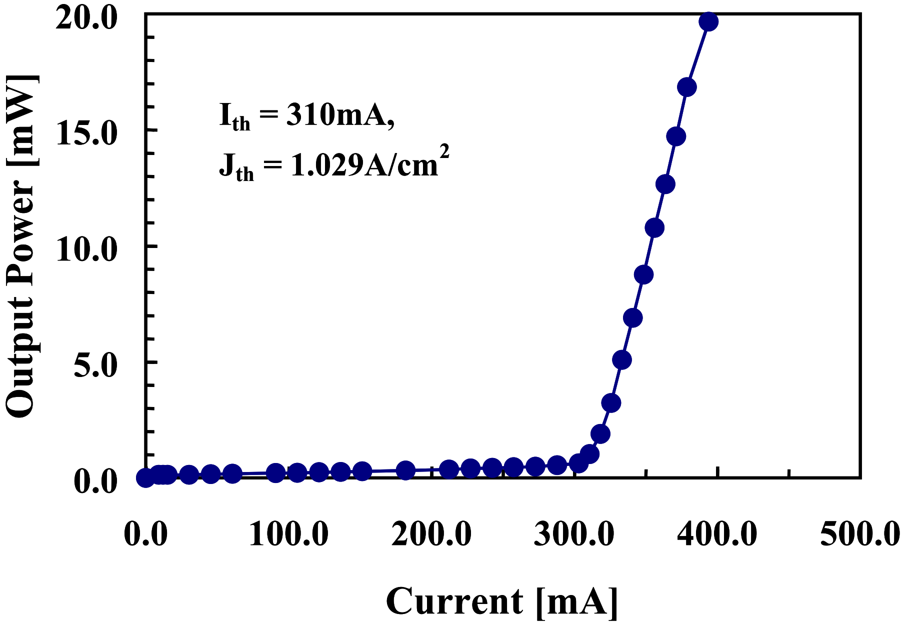

Figure 5.6 Light output-vs.-current characteristics for a 60 μm-stripe x 500 μm-long laser at 300K under pulse mode conditions (0.4 μs pulse, 0.1 % duty cycle).

The light-output versus current (*L-I*) curve of a 500 μm-long cavity laser operated in pulsed mode at 300 K is shown in Figure 5.6. A pulse width of 0.4 μs and a duty cycle of 0.1 % were used for all measurements. I_{th} and J_{th} are 310 mA and 1.029 kA/cm^2, respectively. A differential quantum efficiency of 28 % is calculated from the *L-I* curve. The smallest value of J_{th} = 608 A/cm^2 was obtained for a 1370 μm-long laser. The infinite cavity length threshold current density J_∞ = 265.0 A/cm^2 is extrapolated from the J_{th} vs. inverse cavity length data. The J_∞ value of the GaAsSb QW laser is greater than that of InGaAs QW laser meaning that the material or interface quality of GaAsSb QW is poorer than that of InGaAs laser. However this value is comparably small (see Figure 1.4).

Figure 5.7 shows spontaneous and lasing spectra of a 500 μm-long laser in pulse mode condition at 300 K. The lasing peak at 1.15I_{th} occurs at λ~1.200 μm while at 0.05I_{th} current injection, the electroluminescence peak occurs at 1.215 μm. The blue shift between the sub-threshold and lasing wavelength of this device is only 12.4 meV. In GaAsSb QW lasers having GaAs barriers [51], the reported blue shift was ~26 meV, due to the Type-II band lineup of the GaAs/GaAsSb heterostructure-interface. The small blue shift in this sample is attributed to the Type-I band lineup of the GaAsP/GaAsSb heterostructure-interface.

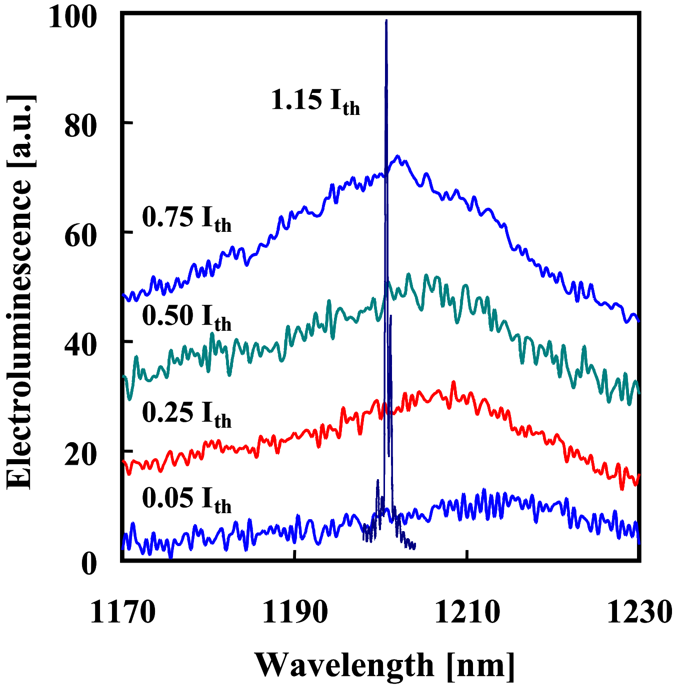

Figure 5.7 Spontaneous and lasing spectra for a 60 μm-stripe and 500 μm-long laser at room temperature under pulsed operation (I_{th} = 305 mA).

We have also evaluated the internal quantum efficiency (η_i) and the internal loss (α_i) from the inverse external differential quantum efficiency (η_d) vs. cavity length (L) plot (Figure 5.8). The solid line and broken line are obtained from the data of the GaAsSb lasers and InGaAs lasers, respectively. The η_d is defined as

$$\frac{1}{\eta_d} = \frac{1}{\eta_i}\left(\frac{\alpha_m + \alpha_i}{\alpha_m}\right) \qquad \text{Equation 5.1}$$

where the mirror loss (α_m) is described as

$$\alpha_m = \frac{1}{\boldsymbol{L}} \ln(\frac{1}{\boldsymbol{R}}) \qquad \text{Equation 5.2}$$

where R is the power reflectivity of the mirror, and $R = 0.32$ is used for an uncoated mirror in the calculation. The calculated η_i values are 33.8% for the GaAsSb QW lasers and 51.5% for the InGaAs QW lasers. The lower η_i of the GaAsSb samples is not due to the large compressive strain effect of the GaAsSb QWs, because the tensile-strained GaAsP barriers compensate for the compressive strain of the QWs. We attribute this reduced η_i to the smaller conduction-band offset of the GaAsP/GaAsSb hetero-interface. From the slopes in the figure, α_i is estimated to be 8.4 cm^{-1} for the GaAsSb QW lasers and 7.5 cm^{-1} for InGaAs QW lasers. The high internal loss of the GaAsSb LD's implies that the crystalline or the interfaces of the GaAsSb QWs are slightly inferior to that of the InGaAs QWs.

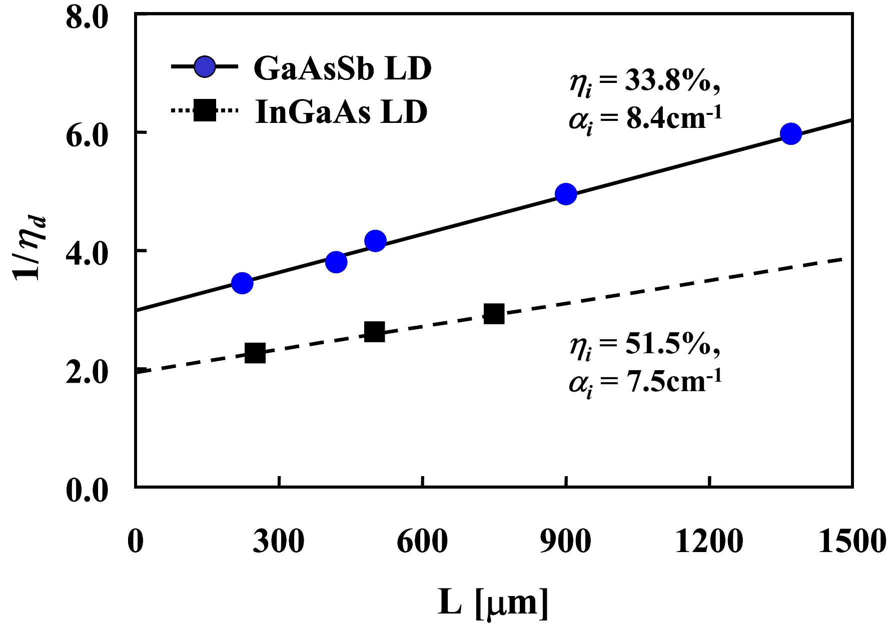

Figure 5.8 Inverse external differential quantum efficiency vs. cavity length.

In Figure 5.9, the threshold current density (J_{th}) as a function of total loss (α), where $\alpha = \alpha_i + \alpha_m$, is shown. The solid and broken lines denote the GaAsSb QW lasers and InGaAs QW lasers, respectively. Following the method described in Ref. 15, we have calculated the transparency current density (J_{tr}) and gain constant (G_0). For the G_0 calculations, confinement factors (Γ) of 0.02081 and 0.02873 were used for GaAsSb and InGaAs laser structures, respectively. The J_{tr} and G_0 are found to be 135 A/cm^2 and 1728 cm^{-1} for GaAsSb QW LDs and 73 A/cm^2 and 1940 cm^{-1} for InGaAs QW LDs. These values are comparable to the reported values of MBE-grown GaAsSb lasers [51].

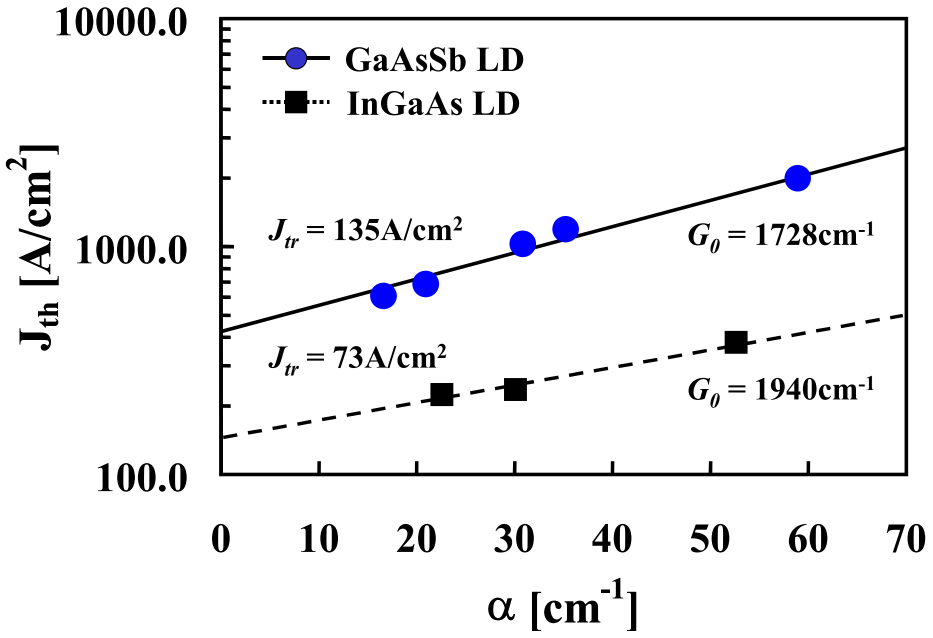

Figure 5.9 Threshold current density vs. total loss

Until now, we have discussed the a feasibility of GaAsSb QW laser with GaAsP barriers for long-wavelength application by comparing with the performance of InGaAs QW lasers. Although the over-all performance of the GaAsSb laser is inferior to that of the InGaAs laser, it seems viable from the wavelength point of view and can be grown monolithically by MOCVD. However, the lasing wavelength that discussed above (λ = 1.2 μm) is still short for optical communication and it was achieved in pulsed mode operation. To increase the lasing wavelength and to achieve CW operation, we have attempted to control the growth conditions more precisely.

With the improved growth conditions, 1.274 μm CW lasing has been achieved in $GaAs_{0.67}Sb_{0.33}$ SQW-SCH with $GaAs_{0.80}P_{0.20}$ barriers. The device cavity was 1050 μm-long and used a 4 μm-wide metal stripe (Figure 5.10). The 110 Å-thick GaAsSb QW active region was grown at 570 ºC and the V/III ratio was 14.23. The I_{th} of the device was 354 mA. The use of additional strain compensation coupled with a higher Sb alloy QW composition, and a thicker QW could result in CW operation at a longer wavelength.

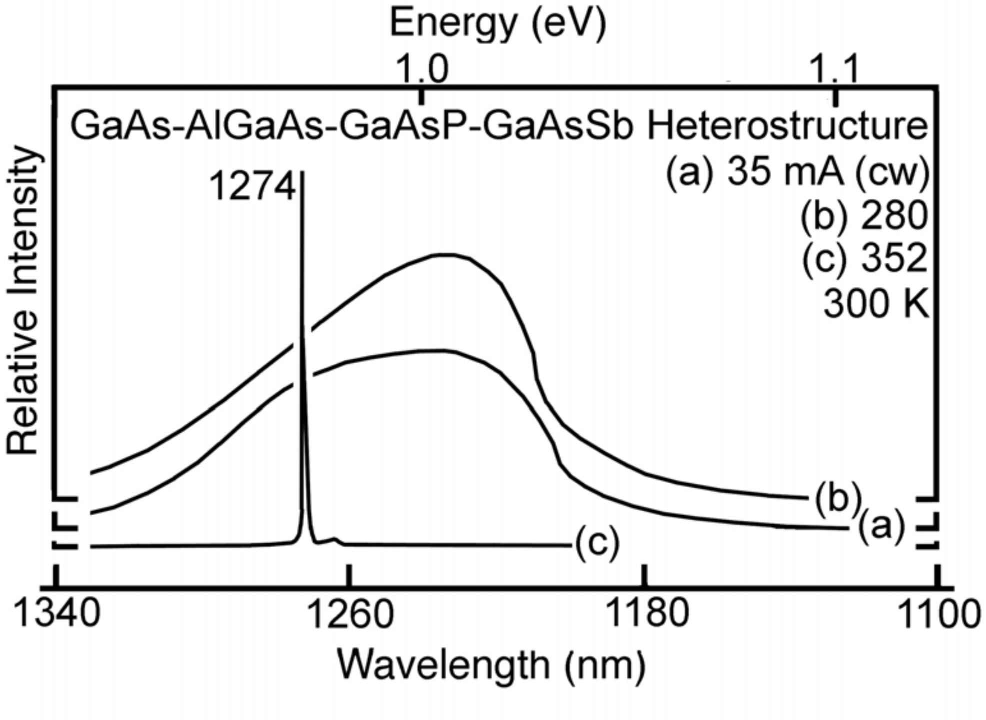

Figure 5.10 Spontaneous and lasing spectra for a 1050 μm-long and 4 μm-strip laser at room temperature under CW operation (I_{th} = 310 mA).

Although we have a long lasing wavelength with the 4 μm-wide metal stripe device, the calculated J_{th} (7.0 kA/cm^2) is significantly large due to current spreading. To obtain more accurate J_{th} with minimized current spreading, 20 μm-wide stripe lasers were fabricated with various cavity lengths. The J_∞ of 325 A/cm^2 is extrapolated from the J_{th} vs. inverse cavity length plot (Figure 5.11).

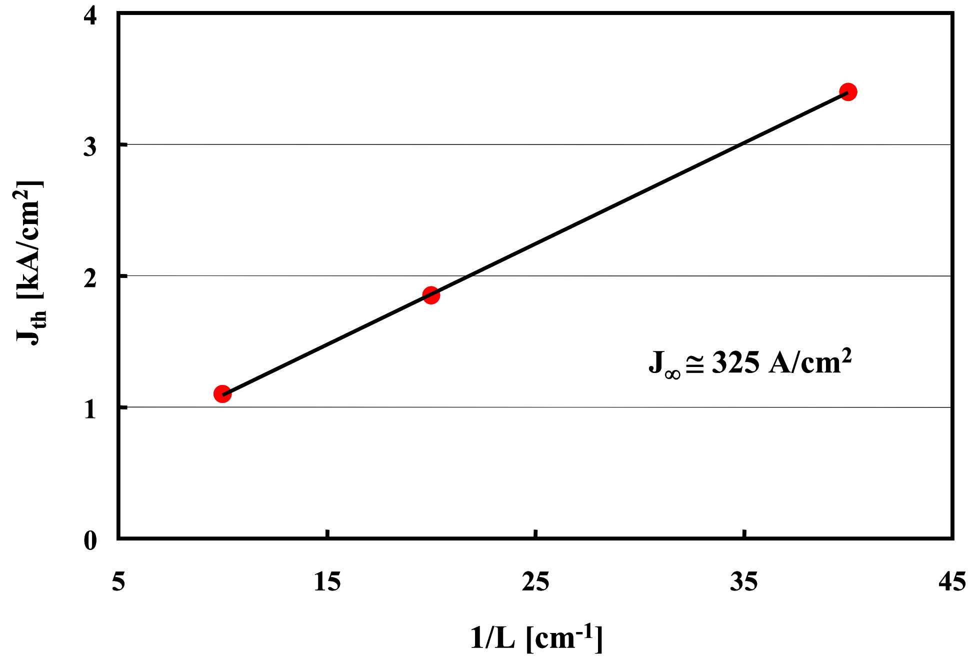

Figure 5.11 Threshold current density (J_{th}) vs. inverse cavity length.

This J_∞ value is bigger than that of 1.2 μm lasing wavelength GaAsSb QW laser due to the higher strain. For 975 μm-long cavity and 20 μm-wide strip device, I_{th} of 385 mA, and λ of 1.270 μm were achieved in CW operation at room temperature. The calculated J_{th} was 1.97 kA/cm^2. In Figure 5.12, the lasing spectra of the laser are shown.

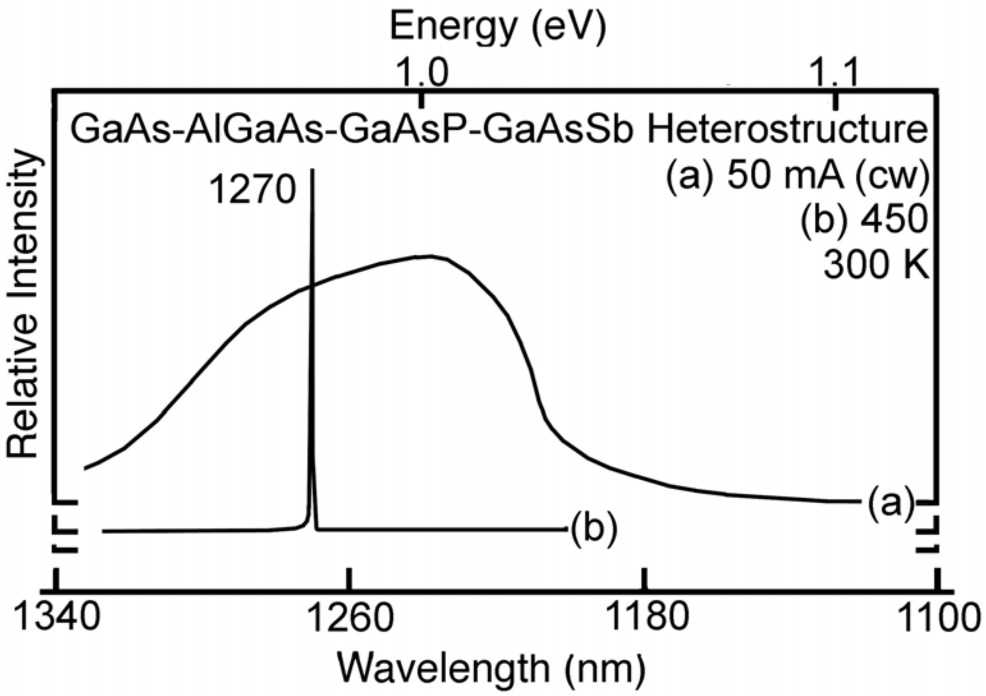

Figure 5.12 Spontaneous and lasing spectra for a 975 μm-long and 20 μm-strip laser at room temperature under CW operation (I_{th} = 385 mA).

From the discussed results, the GaAsSb QW laser that has strain compensation using GaAsP barriers is believed to be a good candidate for long-wavelength optical communication system applications. The 1.274 μm lasing wavelength under CW operation is the longest one yet reported at 300 K for a monolithically MOCVD-grown GaAsSb QW active-region laser.

Chapter 6: Summary and Future Work

GaAsSb compound semiconductor alloys are promising candidates for long-wavelength light-emitting active material, because this ternary system has a direct bandgap spanning the spectral range from the near infrared to far infrared. Recently, there has emerged a new demand for long wavelength VCSELs operating near $\lambda = 1.33$ μm, because such device would have several benefits over the conventional edge-emitting semiconductor lasers such as one-step growth, and ease of device testing as well as the compatibility with 2D or 3D data processing. Although InGaAsP/InP based edge emitting semiconductor lasers have been well developed for optical communication purposes, it is very hard to realize VCSELs with the InGaAsP/InP material system due to the lack of high-refractive-index-contrast DBR pairs grown lattice-matched on InP substrates. The GaAsSb material system has been studied intensively for application in the active region of long-wavelength semiconductor lasers, especially in order to realize a long-wavelength VCSEL, because this material system can be grown strained on GaAs substrates and hence high-refractive-index-contrast AlGaAs/GaAs DBR mirror pairs can be employed.

In this work, we have developed GaAsSb QW lasers grown on GaAs substrates by MOCVD to meet the requirements for 1.3 μm-range optical communications. Until now, most reported GaAsSb QW laser devices were grown by MBE or by a complicated MBE-MOVCD-MBE three-step growth process. Since MOCVD is superior to MBE from the economical point of view, monolithic GaAsSb lasers grown by MOCVD are preferred to growth by MBE. Although several GaAsSb QW lasers grown by MOCVD were reported, the lasing wavelength is limited at a short wavelength of around 1.2 μm.

The development of fully-MOCVD grown long-wavelength GaAsSb QW lasers is the main goal of this work.

To grow better semiconductor materials by MOCVD and to optimize the growth conditions, it is essential to have profound knowledge of the growth system and the characterization techniques. The growth concept and experimental apparatus of MOCVD and the fundamental characterization techniques, such as XRD, AFM, PL, CL, ECV, and TEM, were discussed.

Typical laser structures consist of AlGaAs cladding and waveguide layers, barrier layers composed of various materials, and a GaAsSb QW active region. Studies of the effect of changing the MOCVD growth parameters, such as the growth temperature, V/III ratio, and the growth rate, allowed us to optimize the growth conditions for each layer. The material quality of the grown layers was determined by using the characterization techniques described above. For n-type and p-type dopants for the lower and upper cladding layer, Si and C were employed, respectively. Uniform and high enough doping concentrations were achieved in both type of doped layers. Especially for the GaAsSb QW active layer, a large number of test structures were grown to optimize and improve the material and optical quality by changing basic growth parameters as well as the barrier materials.

Based on the optimized growth conditions, we first grew an InGaAs QW laser for the purposes of comparison and checking the performance of the MOCVD system and the performance of the stacked layers with the thickness needed in real devices. The fabricated laser devices had very good electrical and optical characteristics, revealing that the growth system and device structures were of high quality.

In the next step to develop this long-wavelength lase device, GaAsSb QWs with GaAs barriers were imbedded into the laser structure as an active region replacing the InGaAs QW. We have obtained CW lasing from the GaAsSb/GaAs SQW-SCH laser with a lasing wavelength at λ = 1.228 μm. However to fulfill the requirement of better optical confinement and longer wavelength laser operation, we have employed novel barrier materials, such as InGaP and GaAsP to achieve a Type-I band lineup and to incorporate strain-compensation because the GaAs-barrier GaAsSb QW structure has reported to have Type-II band lineup and huge compressive strain.

We have grown strain-compensated GaAsSb DQW laser structures with GaAsP barrier on GaAs substrates. The broad-area edge-emitting lasers have operated at a wavelength of $\lambda \sim 1.200$ μm at 300 K in a pulsed-mode operation condition. The emission energy blue-shift (before and after lasing threshold) was only 12.4 meV, indicating that GaAsP/GaAsSb has a Type-I band alignment. A minimum threshold current density of 608 A/cm^2 was measured for a 1370 μm-long cavity laser. The infinite-cavity-length threshold current density, J_∞, was 265 A/cm^2. We found values of $\eta_i = 33.8$ % and $\alpha_i = 8.4$ cm^{-1}. We calculated a transparency current density of $J_{tr} = 135$ A/cm^2 and a gain constant of $G_0 = 1728$ cm^{-1}. From these results, we conclude that MOCVD-grown strain-compensated GaAsSb/GaAsP QWs are promising active-region material for long-wavelength laser applications. To increase the lasing wavelength, further experiments were done to control the growth parameters precisely. With improved conditions ters, we could grow thicker QWs and we also increased the Sb composition in the GaAsSb QW layers without a significant degradation of material quality. The fabricated laser devices were operated in CW mode at 300 K and exhibited a lasing wavelength at 1.274 μm. The maximum output power reached at over 14 mW per uncoated facet. To our best knowledge, this CW lasing wavelength is the longest one in the GaAssb system that is grown monolithically by MOCVD.

For future work, several experimental approaches are suggested. First the thermal cycling effect should be examined in detail for the various barrier materials. In VCSEL applications, usually current confinement is achieved by a thermal oxidation process at medium to high temperatures (400 ~ 500 ºC). Therefore it is essential to minimize thermal degradation during thermal processing by growing a more robust GaAsSb material. Second, to increase the lasing wavelength to 1.3 μm, the Sb incorporation into GaAsSb QW should be increased. This can be accomplished by the much more precise control of the growth parameters and by a deeper understanding of the thermodynamics and kinetics during the MOCVD growth. Finally, although we discussed the feasibility of InGaP as a strain-compensation barrier, this material has not been studied thoroughly because the faster thermal degradation of GaAsSb/InGaP QWs and the much different growth conditions required for InGaP relative to GaAs and GaAsP barriers. However we believe that this material can be an attractive alternative candidate for the barrier material due to the higher bandgap for the Type-I band lineup and the availability of strain-compensation with this system With more studies the optimized growth conditions are undertaken, it could be a promising barrier material for a good performance long-wavelength GaAsSb-based laser.

Bibliography

[1] Y. Sakata, T. Hosoda, Y. Sasaki, S. Kitamura, M. Yamamoto, Y. Inomoto, and K. Komatsu, IEEE J. Quantum Electron. 35, 368 (1999).

[2] A. F. Phillips, S. J. Sweeney, A. R. Adams, and P. J. A. Thijs, IEEE J. Sel. Top. Quantum Electron. 5, 401 (1999).

[3] K Iga, IEEE J. Quantum Electron. 24, 1845 (1988).

[4] C. W. Wilsen, J. Temkin, and L. Coldren, "Vertical-Cavity Surface-Emitting Lasers: Design, Fabrication, Chacterization, and Application," Cambridge University Press, Cambridge, UK (1999).

[5] M. Ogura, W. Hsin, M.-C. Wu, S. Wang, J. R. Whinnery, S. C. Wang, and J. J. Yang, Appl. Phys. Lett. 51, 1655 (1987).

[6] J. J. Wierer, D.A. Kellogg, and N. Holonyak, Jr., Appl. Phys. Lett. 74, 926 (1999).

[7] M. Peter, R. Kiefer, F. Fuchs, N. Herres, K. Winkler, K. -H. Bachem, and J. Wagner, Appl. Phys. Lett. 74, 1951 (1999).

[8] D. L. Smith, and C. Mailhiot, J. Appl. Phys. 62, 2545 (1987).

[9] X. Sun, S. Wang, J. S. Hsu, R. Sidhu, X. G. Zheng, X. Li, J. C. Campbell, A. L. Holmes, IEEE J. Sel. Top. Quantum Electron. 8, 817 (2002).

[10] Y. -H Zhang, Appl. Phys. Lett. 66, 118 (1995).

[11] S. P. Watkins, O. J. Pitts, C. Dale, X. G. Xu, M. W. Dvorak, N. Matine, and C. R. Bolognesi, J. Cryst. Growth 221, 59 (2000).

[12] S. Neumann, W. Prost, and F. –J. tegude, 15th IEEE Inter. Conf. Indium Phosphide and Related Materials (IPRM 2003), pp.575-578, IEEE, Santa Barbara, California (2003).

[13] M. W. Dvorak, and C. R. Bolognesi, IEEE Trans. Microw. Theory Tech. 51, 1640 (2003).

[14] R. Bhat, W. –P. Hong, C. Caneau, M. A. Koza, C. –K. Nguyen, S. Goswami, Appl. Phys. Lett. 68, 7 (1996)

[15] M. Kondow, T. Kitani, S. Nakatsuka, M. C. Larson, K. Nakahara, Y. Yazawa, and M. Okai, IEEE J. Sel. Top. Quantum Electron. 3, 719 (1997).

[16] J. S. Harris, IEEE J. Sel. Top. Quantum Electron. 6, 1145 (2000).

[17] M. Yamada, M. Shimizu, T. Takeshita, M. Okayasu, M. Horiguchi, S. Uehara, and E. Sugita, IEEE Photonics. Technol. Lett. 1, 422 (1989).

[18] L. Yang, A. S. Sudbo, W. Tsang, P. A. Garbinski, and R. M. Camarda, IEEE Photonics Technol. Lett. 2, 59 (1990).

[19] D. Schlenker, Z. Pan, T. Miyamoto, F. Koyama, and K. Iga, Jpn. J. Appl. Phys. 38, 5023 (1999).

[20] D. L. Huffaker, G. Park, Z. Zou, O. B. Shchekin, and D. G. Deppe, Appl. Phys. Lett. 73, 2564 (1998).

[21] A. E. Zhukov, A. R. Kovsh, V. M. Ustinov, Y. M. Shernyakov, S. S. Mikhrin, N. A. Maleev, E. Y. Kondrat'eva, D. A. Livshits, M. V. Maximov, B. V. Volovik, D. A. Bedarev, Y. G. Musikhin, N. N. Ledentsov, P. S. Kop'ev, Z. I. Alferov, and D. Bimberg, IEEE Photonics Technol. Lett. 11, 1345 (1999)

[22] D. L. Huffaker, G. Park, Z. Zou, O. B. Shchekin, and D. G. Deppe, IEEE J. Sel. Top. Quantum Electron. 6, 452 (2000).

[23] J. J. Dudley, D. I. Babic, R. Mirin, L. Yang, B. I. Miller, R. J. Ram, T. Reynolds, E. L. Hu, and J. E. Bowers, Appl. Phys. Lett. 64, 1463 (1994).

[24] Y. Qian, Z. H. Zhu, Y. H. Lo, H. Q. Hou, M.C. Wang, and W. Lin, IEEE Photonics Technol. Lett. 9, 8 (1997).

[25] V. Jayaraman, T. J. Goodnough, T. L. Beam, F. M. Ahedo, and R. A. Maurice, IEEE Photonics Technol. Lett. 12, 1595 (2000).

[26] R. M. Biefeld, Mater. Sci. Eng. R36, 105 (2002).

[27] S. R. Johnson, C. Z. Guo, S. Chaparro, Y. G. Sadofyev, J. Wang, Y. Cao, N. Samal, J. Xu, S. Q. Yu, D. Ding, and Y.-H. Zhang, J. Cryst. Growth 251, 521 (2003).

[28] Landolt-Bernstein, Numerical Data and Functional Relationships in Science and Technology, New Series, Group III, Volume 22, edited by O. Medelung (Springer-Velag, Berlin, 1982).

[29] J. W. Matthews, and A. E. Blakeslee, J. Cryst. Growth 27, 118 (1974).

[30] J. W. Matthews, A. E. Blakeslee, and J. S. Harris, Thin Solid Films 33, 253 (1976).

[31] K. Ikossi-Anastasiou, IEEE Trans. Electron. Devices 40, 878 (1993).

[32] S. L. Chuang, Phys. Rev. B 43, 9649 (1991).

[33] I. Lefebvre, C. Oriester, M. Lannoo, and G. Hollinger, J. Vac. Sci. Technol. B 12, 2527 (1994).

[34] K. Nishi, T. Anan, and S. Sugou, Digest of the LEOS summer Topical Meeting, ThA1.4, pp. III39-III40, San Diego, California (1999).

[35] C. B. Cooper, R. R. Saxena, and M. J. Ludowise, J. Electron. Mater. 11, 1001 (1982).

[36] G. B. Stringfellow, J. Cryst. Growth 64, 413 (1983).

[37] G. B. Stringfellow, J. Cryst. Growth 68, 111 (1983).

[38] G. B. Stringfellow, “Organometallic Vapor-Phase Epitaxy: Theory and Practice,” 2nd Ed., pp. 20-34, Academic Press, San Diego, California (1999).

[39] G. B. Stringfellow, J. Cryst. Growth 27, 21 (1974).

[40] H. Sakaki, L. L. Chang, R. Ludeke, C.-A. Chang, G. A. Sai-Halasz, and L. Esaki, Appl. Phys. Lett. 31, 211 (1977).

[41] A. D. Prins, D. J. Dunstan, J. D. Lambkin, E. P. O’reilly, and A. R. Adams, Phys. Rev. B 47, 2191 (1993).

[42] G. Ji, S. Agarwala, D. Huang, and H. Morkoc, Phy. Rev. B 38, 10571 (1988).

[43] M. Peter, J. Forker, K. Winkler, K. H. Bachem, and J. Wagner, J. Electron. Mater. 24, 1551 (1995).

[44] R. Teissier, D. Sicault, J. C. Harmand, G. Ungaro, G. Le Roux, and L. Largeau, J. Appl. Phys. 89, 5473 (2001).

[45] M. S. Noh, J. H. Ryou, R. D. Dupuis Y. –L Chang, and R. H. Weissman, submitted to J. Appl. Phys. (2003).

[46] T. Anan, K. Nishi, S. Sugou, M. Yamada, K. Tokutome, and A. Gomyo, Electron. Lett. 34, 2127 (1998).

[47] T. Anan, M. Yamada, K. Tokutome, S. Sugou, K. Nishi, and K. Kamai, Electron. Lett. 35, 903 (1999).

[48] T. Anan, M. Yamada, K. Nishi, K. Kurihara, K. Tokutome, A. Kamei, and S. Sugou, Electron. Lett. 37, 566 (2001).

[49] M. Yamada, T. Anan, K. Kurihara, K. Nishi, K. Tokutome, A. Kamei, and S. Sugou, Electron. Lett. 36, 637 (2000).

[50] M. Yamada, T. Anan, K. Tokutome, A. Kamei, K. Nishi, and S. Sugou, IEEE Photonics Technol. Lett. 12, 774 (2000).

[51] O. Blum and J. F. Klem, IEEE Photonics Technol. Lett. 12, 771 (2000).

[52] S. W. Ryu and P. D. Dapcus, Electron. Lett. 36, 1387 (2000).

[53] F. Quochi, J. E. Cunningham, M. Dinu, and J. Shah, Electron. Lett. 36, 2075 (2000).

[54] H. M. Manasevit and W. I. Simpson, J. Electrochem. Soc. 116, 1725 (1969).

[55] Y. Seki, K. Tanno, K.Iida, and E, Ichiki, J. Electrochem. Soc. 122, 1108 (1975).

[56] R. D. Dupuis and P. D. Dapkus, Appl. Phys. Lett. 32, 406 (1978).

[57] A. Y. Cho, J. Vac. Sci. Technol. 16, 275 (1979).

[58] G. A. Antypas and L. W. James, J. Appl. Phys. 41, 2165 (1970).

[59] K. Sugiyama and H. Saito, Jpn. J. Appl. Phys. 11, 1057 (1972).

[60] T. Waho, S, Ogawa, and S, Maruyama, Jpn. J. Appl. Phys. 16, 1875 (1979).

[61] A. Bosacchi, S. Franchi, P. Allegri, V. Avanzini, A. Baraldi, R. Magnanini, M. Berti, D. De Salvador, and S. K. Sinha, J. Cryst. Growth 201/202, 858 (1999).

[62] F. Quochi, D. C. Kilper, J. E. Cunningham, M. Dinu, and J. Shah, IEEE Photonics Technol. Lett. 13, 921 (2001).

[63] M. Razeghi, "The MOCVD Challenge Volume 2: A survey of GaInAsP-GaAs for photonic and electronic device applications," Institute of Physics Publishing, pp. 42-47, Philadelphia, Pennsylvania (1995).

[64] D. J. H. Lambert, “Growth and Characterization of Group III-Nitride Power Transistors, Power Rectifiers, and Solar Blind Detectors by Metalorganic Chemical Vapor Deposition,” Ph.D. Dissertation, The University of Texas at Austin (2000).

[65] “Chemical properties,” Epichem, Allentown, Pennsylvania (2003).

[66] C. A. Larson, N. I. Buchan, S. H. Li, and G. B. Strinfellow, J. Cryst. Growth 94 663 (1989).

[67] S. H. Li, C. A. Larson, N. I. Buchan, and G. B. Stringfellow, J. Electron. Mater. 18, 457 (1989).

[68] M. J. Cherng, H. R. Jen, C. A. Larsen, and G. B. Stringfellow, J. Cryst. Growth 77, 408 (1986).

[69] G. B. Stringfellow, “Organometallic Vapor-Phase Epitaxy: Theory and Practice,” 2nd Ed., ch. 2-6, Academic Press, San Diego, California (1999).

[70] M. Razeghi, “The MOCVD Challenge Volume 2: A survey of GaInAsP-GaAs for photonic and electronic device applications,” Institute of Physics Publishing, pp. 29-42, Philadelphia, Pennsylvania (1995).

[71] G. B. Stringfellow, “Organometallic Vapor-Phase Epitaxy: Theory and Practice,” 2nd Ed., pp. 211-225, Academic Press, San Diego, California (1999).

[72] H. Heinecke, E. Veuhoff, N. Putz, M. Heyen, and P. Balk, J. Electron. Mater. 13, 815 (1984).

[73] T. F. Kuech and E. Veuhoff, J. Cryst. Growth 68, 148 (1984).

[74] V. Swaminathan and A. T. Macrander, pp. 181-232, Prentice Hall, Englewood Cliffs, New Jersey (1991).

[75] B. D. Cullity and S. R. Stock, “Elements of X-Ray Diffraction,” 3rd Ed., pp. 524-538, Prentice Hall, Upper Saddle River, New Jersey (2001).

[76] B. D. Cullity and S. R. Stock, “Elements of X-Ray Diffraction,” 3rd Ed., pp. 520-521, Prentice Hall, Upper Saddle River, New Jersey (2001).

[77] C. Kittel, “Introduction to Solid State Physics,” 6th Ed., John Wiley & Sons, New York (1991).

[78] V. Swaminathan and A. T. Macrander, "Materials Aspects of GaAs and InP Based Structures," pp. 281-321, Prentice Hall, Englewood Cliffs, New Jersey (1991).

[79] M. Dinu, J. E. Cunningham, F. Quochi, and J. Shah, Appl. Phys. Lett. 94, 1506 (2003).

[80] G. Binnig, C.F. Quate, Ch. Geber, Atomic Force Microscope, Phys. Rev. Letters, 56, 930 (1986).

[81] G. Binnig, H. Rohrer, Ch. Gerber, E. Weibel, Phys. Rev. Letters, 49, 57 (1982).

[82] "Dimension 3000 Scanning Probe Microscope Instruction Manual," Digital Instrument, Santa Barbara, California (1994).

[83] P. Blood, Semicond. Sci. and Tech. 1, 7 (1986)

[84] D. K. Schroder, "Semiconductor material and device charcterization," pp. 41-58, John Wiley & Sons, Inc, New York, (1990).

[85] M. T. Furtado, M. S. S. Loural, and A. C. Sachs, J. Appl. Phys. 62, 4926 (1987).

[86] D. B. Williams and C. B. Carter, "Transmission Electron Microscopy" Plenum, New York (1996).

[87] H. Terao and H. Sunakawa, J. Cryst. Growth 68, 157 (1984).

[88] T. F. Kuech, R. Potemski, R. Cardona, and G. Scilla, J. Electron. Mate. 21, 341 (1992).

[89] P.M. Enquist, J. A. Hutchby, And T. H. de Lyon, J. Appl. Phys. 63, 4485 (1988).

[90] A. Kozen, S. Nojima, J. Tenmyo, and J. Ashahi, J. Appl. Phys. 59, 1156 (1986).

[91] N. Nordell, P. Ojala, W. H. van Berlo, and M. K. Linnarsson, J. Appl. Phys. 67, 778 (1990).

[92] W. S. Hobson, S. J. Pearton, E. F. Schubert, and G. Cabaniss, Appl. Phys. Lett. 55, 1546 (1989).

[93] L. J. Guido, G. S. Jackson, D. C. Hall, W. E. Plano, N. Holonyak, Jr., Appl. Phys. Lett. 52, 522 (1987).

[94] N. Pan, R. R. Welser, C. R. Lutz, P. M. DeLeka, B. Ham, K. Hong, J Cryst. Growth 225, 397 (2001).

[95] R. D. Rajavel, T. Hussain, M. C. Montes, M. W. Sawins, S. Thomas III, C. H. Chow, J. Cryst. Growth 251, 848 (2003).

[96] K. Tateno, Y. Kohama, and C. Amano, J. Cryst. Growth 172, 5 (1997).

[97] M. Konagai, T. Yamada, T. Akatsuka, S. Nozaki, R. Miyake, K. Saito, T. Fukamachi, E. Tokumitsu, and K .Takahashi, J. Cryst. Growth 105, 359 (1990).

[98] T. F. Kuech, M. A. Tischler, P. –J. Wang, G. Scilia, R. Potemski, and R. Cardone, Appl. Phys. Lett. 53, 1317 (1998).

[99] N. Watanabe, H. Ito, and T. Ishibashi, J. Cryst. Growth 147, 256 (1995).

[100] B. T. Cunningham, G. E. Stillman, and G. S. Jackson, Appl. Phys. Lett. 56, 361 (1990).

[101] W. K. Liu, K. Bacher, F. J. Towner, T. R. Stewart, C. Reed, P. Specht, R. C. Lutz, R. Zhao, and E. R. Weber, 201/202, 217 (1999).

[102] S. Bhunia, K. uchida, S. Nozaki. N. Sugiyama, M Furiya, and H. Morisaki, J. Appl. Phys. 93, 1613 (2003).

[103] J. S. Lee, I. Kim, B. D. Choe, and W. D. Jeong, J. Appl. Phys. **76**, 5079 (1994).

[104] G. B. Stringfellow, J. Cryst. Growth 75, 91 (1986).

[105] Z. M. Fang, K. Y. Ma, D. H. Jaw, R. M. Cohen, and G. B. Stringfellow, 67, 7034 (1990).

[106] J. R. Pessetto and G. B. Stringfellow, J. Cryst. Growth 62, 1 (1983).

[107] M. F. Gratton, R. G. Goodchild, L. Y. Juravel, and J. C. Wiklley, J. Electron. Mater. 8, 25 (1979).

[108] N. Takenaka, M. Inoue, J. Shirafuji, and Y. Inuishi, J. Phys. D 11, L91 (1978).

[109] H. Mani, A. Joullie, F. Karouta, and C. Schiller, J. Appl. Phys. 59, 2728 (1986).

[110] M. J. Cherng, G. B. Stringfellow, and Y. R. M. Cohen, Appl. Phys. Lett. 44, 677 (1984).

[111] C. B. Cooper, R. R. Saxena, and M. J. Ludowise, J. Electron. Mater. 11, 1001 (1982).

[112] Q. Xie, J. E. van Nostrand, J. L. Brown, and C. E. Stutz, J. Appl. Phys. 86, 329 (1999).

[113] E. Selvig, B. O. Fimland, T. Skauli, and R. Haakenaasen, J. Cryst. Growth 227/228, 562 (2001).

[114] S. L. Chuang, “Physics of Optoelectronic Device,” pp. 147-154, Wiley, New York, (1995).

[115] R. L. Anderson, Solid-State Electron. 5, 341 (1962).

[116] C. G. van de Walle and R. M. Matin, Phys. Rew. B 34, 5621 (1986).

[117] G. Liu, S. -L. Chuang, and S. -H. Park, J. Appl. Phy. 88, 5554 (2000).

[118] A. Ichii, Y. Tsou, and E. Garmire, J. Appl. Phys. 74, 2112 (1993).

[119] R. E. Nahory, M. A. Pollack, J. C. DeWinter, and K. M. Williams, J. Appl. Phys. 48, 1607 (1977).

[120] M. C. DeLong, P. C, Taylor, and J. M. Olson, Appl. Phys. Lett. 57, 620 (1990).

[121] D. Vignaud, X. Wallart, and F. Mollot, Appl. Phys. Lett. 72, 1075 (1998).

[122] M. S. Noh, R. D. Dupuis, D. P. Bour, G. Walter, and N. Holonyak, Jr., Appl. Phys. Lett. 94, 2530 (2003).

Vita

Min-Soo Noh was born in Seoul, Korea, on April 4, 1965, the son of Dr. Kyung-Pok Noh and Kyung-Ja Shin. After graduating from Joongkyung High School, in 1984, he enrolled at Yonsei University in Seoul, Korea to study Physics. He received a Bachelor of Science in Physics degree in February 1988. He enrolled in the Graduate School at Yonsei University in March 1988. He joined the Solid State Physics Laboratory supervised by Dr. Choong Hyun Chung and received his Mater of Science in Physics degree in February 1990 after completing his thesis entitled “Fabrication of Atomic Layer Epitaxy Growth System”. He worked at GoldStar Central Research Laboratory from January 1990 to July 1999. He married Sora Jeong on February 25, 1995. He enrolled in the Graduate School at The University of Texas at Austin to study electrical engineering in solid-state electronics area toward his Ph.D. degree in the fall of 1999. At the same time, he joined the MOCVD group supervised by Dr. Russell D. Dupuis as a Graduate Research Assistant in the Microelectronics Research Center. After receiving his Ph.D. degree in December 2003, he will be working for the Optoelectronics Group at LG Electronics Institute of Technology in Seoul, Korea.

Permanent address: 136-36, 10/6
Itaewon-Dong, Yongsan-Gu
Seoul, 140-858, Korea

This dissertation was typed by the author.